An Engine Air-Brake Integration Study

by

Hiten Mulchandani

Bachelor of Engineering, Mechanical (2008)
The University of Auckland

Submitted to the Department of Aeronautics and Astronautics
in partial fulfillment of the requirements for the degree of

Master of Science in Aeronautics and Astronautics

at the

MASSACHUSETTS INSTITUTE OF TECHNOLOGY

February 2011

Author .....
Department of Aeronautics and Astronautics
October 22, 2010

Certified by .....
Zoltan S. Spakovszky
Associate Professor of Aeronautics and Astronautics
Thesis Supervisor

Accepted by .....
Eytan H. Modiano
Associate Professor of Aeronautics and Astronautics
Chair, Committee on Graduate Students

An Engine Air-Brake Integration Study

by

Hiten Mulchandani

Submitted to the Department of Aeronautics and Astronautics on
October 22, 2010 in partial fulfillment of the requirements for the degree of
Master of Science in Aeronautics and Astronautics

Abstract

The feasibility of operating an engine air-brake (EAB) integrated with a pylon duct bifurcation in a realistic aircraft engine environment has been analyzed. The EAB uses variable exit guide vanes downstream of a high bypass ratio (BPR) fan rotor to produce drag quietly by swirling flow out of the fan nozzle. The swirling motion yields low pressure in the vortex core from simple radial equilibrium, thereby generating pressure drag. The 4-BB internal plug and 5-BB external plug nozzles of BPR 8 are chosen to provide a realistic environment for model-scale tests at the NASA Aero-Acoustic Propulsion Lab (AAPL). The objectives of this study are to quantify the impact of a pylon on the drag and noise of an EAB, and explore means to mitigate the potential loss of swirling flow and associated drag.

Analysis is conducted at approach conditions on the 4-BB nozzle, with fan and core nozzle pressure and temperature ratios obtained from an engine cycle analysis. A pylon is designed to represent engine installations typically encountered in short-range jet aircraft. The pylon is a prismatic NACA 0012 airfoil geometry with swept leading, trailing edges and an extended internal fairing to facilitate compatibility with both nozzles in the AAPL facility. The EAB cases analyzed include three types of pylon/vane configurations: (1) the baseline pylon with un-deflected swirl vanes is used in the calculation of the equivalent drag coefficient (C_D); (2) the pylon with the trailing edge (TE) flap deflected full-span by 35 degrees is used to set structural load limits for detailed design of the baseline pylon; and (3) configurations with the pylon TE flap deflected partial-span by 20 degrees and asymmetric swirl vanes are used to generate swirling outflow from the fan nozzle exhaust. The partial-span deflection cases are further categorized by the location of the asymmetric vanes: at the nozzle exhaust (aft) and further upstream.

Computational results demonstrate the aft vanes generate C_D in the range 0.35-0.61 and the upstream vane cases produce C_D between 0.09-0.18. The difference in drag is because the flow avoids the majority of the duct bifurcation in the aft vanes cases to produce stronger swirling outflow. A C_D value between 0.7-1.0 is required to achieve a 3-4 degree glidescope change and therefore an overall noise benefit of 2.5 dB for a conventional tube-and-wing aircraft on approach. The aft vane configurations show promise in reaching this target while the upstream vane installation concepts require further investigation.

Thesis Supervisor: Zoltan S. Spakovszky
Title: Associate Professor of Aeronautics and Astronautics

Acknowledgements

As I near the end of my Master's program in Aeronautics at MIT, I am reminded of a phrase I heard (and later took to heart) from one of the directors at the Fulbright Gateway Seminar held in Miami just over two year ago, when I first arrived in the US:

"Find reasons to succeed, not excuses to fail."

This powerful expression has greatly empowered me during my time at graduate school. In addition, however, there are a number of people who have helped, guided, supported, and encouraged me to undertake and successfully complete this program. While I cannot do justice to them all, I would like to highlight the actions of a select few.

First, I would like to thank Professor Zoltan Spakovszky from MIT and Dr. Parthiv Shah from ATA Engineering Inc., for bringing me onboard this project. Professor Spakovszky's energy and passion for fluid mechanics research are contagious and I thank him for pushing me well beyond my comfort zone to accomplish the results that are presented in this thesis. In the same light, Parthiv has been instrumental to my understanding of this project through many involved technical discussions of fluid mechanics concepts associated with swirling flow. Together, they have helped guide my approach to performing original research by encouraging me to think in terms of first principles. You inspire me to give my best every day.

Second, I would like to acknowledge my loving parents and wonderful triplet siblings for their encouragement, counsel, and support throughout my study. My parents Viju and Chandra Kant Mulchandani have always shown unwavering support in my pursuits, often helping me financially, and constantly reminding me that I can overcome any obstacle through hard work, perseverance, and ruthless determination. With my siblings, Hiren and Heena Mulchandani, I have shared many deep conversations about life, love, and happiness. Collectively, my family has encouraged me to expand my horizons outside of graduate school and given me invaluable advice about beginning the next chapter of my life. You are my rock and words cannot adequately capture the love and affection I share for each of you.

Third, I would like to show my gratitude towards my close friends; Jon Allison, Hemant Chaurasia, Sydney Do, Pritesh Mody, and Russ Stratton, (a.k.a. the “Mates”), extended friends; Mehdi Ben Abda, Aditya Bhakta, Indira Deonandan, Nikhil Galagali, Yu-Chung Hsiao, Rezy Pradipta, and Vivek Sharma, and lab friends; Tanya Garza, Ben Glass, Leo Ng, and Shinji Tanaka. I have enjoyed getting to know each of you, and I recall with fondness the fun times we have shared talking about life, research, and where our careers may take us in the future. You have helped make my experience at MIT a memorable one.

Fourth, I would like to recognize my cousin and aunt, Rajesh and Hema Daryani, for providing delicious home-cooked food and a comfortable environment whenever I visited. You made me feel like going home was just a short drive away.

Finally, I am greatly indebted to the folks who have helped fund my study. Thanks to the New Zealand Ministry of Research in Science and Technology, Fulbright New Zealand, and the Fulbright Program for providing a generous seed fund to begin my graduate study. Special thanks also go to ATA for providing partial funding in support of this research.

I am eternally grateful to anyone who has helped me in this endeavor in any way and to each I say sincerely from the bottom of my heart, thank you.

Table of Contents

List of Figures

List of Tables

Nomenclature

Roman

A	area
B	flow blockage
c	chord
C	enclosed contour
C_D	equivalent drag coefficient
C_d	nozzle flow coefficient
C_p	static pressure coefficient
C_S	side load coefficient
D	diameter; corrected flow per unit area (non-dimensional)
F	force
l	length
L	domain axial range
$\dot{m}$	mass flow rate
M	Mach number
n	normal coordinate
$\mathbf{n}$	unit normal vector

p	static pressure
p_t	stagnation pressure
q	dynamic pressure
r	radius
R	ideal gas constant (per unit mass)
S	swirl parameter
T	static temperature
T_t	stagnation temperature
V	velocity
x	axial coordinate

Greek

γ	ratio of specific heats
Γ	circulation
δ^*	boundary layer displacement thickness
η	adiabatic efficiency
θ	glidescope angle
κ	flow turning angle
π	pressure ratio
ρ	density
τ	temperature ratio

$\boldsymbol{\omega}$	vorticity vector

Subscripts

0	EAB with baseline pylon; empty nozzle
atm	atmosphere
c	viscous core
centerbody	surface of the internal plug
cold	cold core
core nozzle	surface of the core nozzle
e	exit
EAB	Engine Air-Brake
fan	fan stream
fan, ideal	ideal engine fan stream
fan nozzle	fan nozzle surface
hot	hot core
inlet	engine inlet
ref	reference value
S	side
system net	net system quantity
thrust	thrust force
u,spill	spillage in the upstream domain
x	axial direction

y	vertical direction
θ	circumferential direction

Superscripts

$\bar{}$	averaged quantity
$\rightarrow$	vector quantity

Acronyms

AP1	Alternative Pylon Configuration 1
AP2	Alternative Pylon Configuration 2
AAPL	NASA's Aero-Acoustic Propulsion Laboratory
BPR	Bypass Ratio
CDA	Continuous Decent Approach
CFD	Computational Fluid Dynamics
CMI	Cambridge/MIT Institute
CNPR	Core Nozzle Pressure Ratio
CNTR	Core Nozzle Temperature Ratio
CV	Control Volume
EAB	Engine Air-Brake
ERA	Environmentally Responsible Aviation
FEGVs	Fan Exit Guide Vanes
FNPR	Fan Nozzle Pressure Ratio

FNTR	Fan Nozzle Temperature Ratio
GE	General Electric
HBPR	High Bypass Ratio
ID	Inner Diameter
ILS	Instrument Landing System
NACA	National Advisory Council on Aeronautics
NPSS	Numerical Propulsion System Simulation
OASPL	Overall Sound Pressure Level
OD	Outer Diameter
OGV	Outlet Guide Vane
RANS	Reynolds Averaged Navier-Stokes
S-A	Spalart-Allmaras
SAI	Silent Aircraft Initiative
SAX-40	Silent Aircraft eXperimental
SDT	Source Diagnostic Test
SLA	Stereolithographic
TE	Trailing Edge
VEGVs	Variable Exit Guide Vanes

Symbols

∞	Freestream value

Chapter 1

Introduction

1.1 Background and Motivation

Since the inception of commercial jet transportation in the 1960s, complaints about airport noise levels have resulted in stricter international noise certifications for airframe manufacturers and airline operators [1]. Through the years, aircraft manufacturers have relied on technological improvements to meet increasingly stringent noise restrictions while regulators have introduced operational changes to address local noise issues. Aircraft noise at take-off and approach are the largest sources of annoyance near airports. Take-off is a high power operation during which noise is dominated by jet noise and turbomachinery sources, primarily from the high bypass ratio fan. Approach is a low power operation during which noise from engine sources is of comparable strength to the airframe noise. Airframe sources include acoustic scattering of turbulent boundary layers past trailing edges of the clean airframe and conventional drag inducing devices such as flaps, slats, and thrust reversers [2].

Operational changes to the aircraft flight trajectory can reduce the perceived noise level at the ground by keeping noise sources farther from the communities surrounding airports. One such idea is the continuous decent approach (CDA), used for decades in numerous successful airport trials in the U.S. and currently in trial around London in the U.K. CDAs work by maintaining a constant three-degree decent angle (glidescope) until meeting the ground-based Instrument Landing System (ILS). This allows the aircraft to approach the airport smoothly from a higher altitude, instead of approaching it in a stair-step fashion, throttling down and requesting permission to fly at each new (lower) altitude [2]. As a result, the noise at a ground level location directly below the flight path is significantly reduced. CDAs in use today emphasize a fixed conventional glidescope; however, emerging innovative technologies may enable even further reduction of noise transmitted to the ground by increasing the glidescope. For an airframe noise-

dominated aircraft on approach with all other sources unchanged, noise reduction to the ground in Equation 1.1 roughly scales as the fifth power of the approach speed and as the square of the distance between the source and observer (or small glidescope angle θ) due to the spherical spreading of the acoustic wave fronts. Therefore, from a noise reduction perspective, an increase in glidescope is desirable because of the increased distance between the source and observer [3].

$$\text{Noise reduction} \approx 10\log_{10}\left(\frac{V}{V_{ref}}\right)^5\left(\frac{\theta_{ref}}{\theta}\right)^2 \tag{1.1}$$

The modern-day noise challenge however is a system-level problem, requiring reductions in both airframe and engine sources, as well as operational changes to further attenuate noise before it reaches the ground. An example of the system-level approach to noise reduction is the Cambridge/MIT Institute (CMI) Silent Aircraft Initiative (SAI). The SAI set goals to develop an aircraft that was no louder than the background noise in a typical urban environment. The outcome is the Silent Aircraft eXperimental (SAX-40) highly integrated airframe/propulsion system. The SAX-40 is an all-lifting, aerodynamically clean body with embedded, acoustically shielded, ultra-high bypass ratio, boundary layer ingesting engines that enable conventional flight trajectories on approach without the use of auxiliary flaps, slats, and thrust reversers [4].

The most recent work on the NASA "N+2" aviation program suggests future aircraft concepts that could be introduced 20 years from now will have a seamless hybrid shape, with an integrated airframe and propulsion system similar to the SAX-40 [5]. This will allow the aircraft to simultaneously reduce noise, emissions and fuel burn. Furthermore, work towards the "N+3" effort is intended to identify key technology development needs, such as advanced airframes and propulsion systems, as well as breakthroughs that will enable such vehicles to enter service in the 2030-2035 time frame [6].

In addition to source noise reduction through cleaner aerodynamics, the foremost means to achieve the aggressive SAI noise goals was to design the airframe for lower speed and a steeper approach profile [3]. The engine air-brake (EAB) device was born out of this requirement for additional quiet drag. The simplest demonstration of quiet drag is the swirl tube concept, conceived and developed at the MIT Gas Turbine Lab (GTL) in 2006 by Shah et al. [3]. The swirl tube is a duct with embedded stationary swirl vanes in which swirling outflow is achieved by ram air passing through the vanes. The EAB technology concept is a propulsion system integrated device that uses variable exit guide vanes (VEGVs) to quietly generate drag via swirling outflow

emanating from the turbofan engine exhaust, thereby reducing an aircraft's measured noise at a ground level location. A key feature of all swirling flows is radial pressure gradients. Simple radial equilibrium for an axisymmetric swirling flow can be written as,

$$\frac{\partial p}{\partial n} = \frac{\rho V_\theta^2}{r} \quad . \tag{1.2}$$

The above equation illustrates the concept behind the generation of pressure drag. Pressure forces balance the centripetal acceleration of fluid particles on curved paths. Thus swirling motion yields low pressure in the vortex core, thereby generating pressure drag. If this swirling motion is stable, it will be quiet, as demonstrated by Shah et al. [7]. The term "quiet" in this context means the noise from the EAB is quieter than the loudest sources on the aircraft, which is usually the airframe noise on approach. This quiet drag could:

1. Enable a steeper and/or slower approach flight path, reducing the community noise footprint.
2. Compensate for the loss of drag from the absence of conventional high-lift devices and faired landing gear associated with a cleaner airframe.

An obvious application of the EAB is onboard an airframe noise-dominated aircraft. While many next-generation airframe/propulsion integrated aircraft will likely be airframe noise-dominated, there are several conventional tube-and-wing type aircraft that may also benefit from additional quiet drag. For example, according to Shah et al. [3], a quiet equivalent drag coefficient (C_D) of approximately 1.0, based on total fan area for the 737-700A class aircraft, is estimated to increase the glidescope at approach from 3 to 4 degrees at constant flight speed. This suggests an overall noise reduction of 2.5 dB.

The MIT GTL has been collaborating with ATA Engineering Inc., (ATA) on the development of the EAB concept. ATA has completed an initial aerodynamic assessment of the EAB concept in which the idea of using VEGVs downstream of a fan rotor in a high bypass ratio (HBPR) cycle was explored as a means to generate swirling outflow. The specific objective of this assessment was to quantify the quiet drag potential of an EAB in a HBPR cycle using a ducted propulsor with VEGVs on an aircraft of the size of a Boeing 787-8. It focused on NASA's Source Diagnostic Test (SDT) ducted propulsor geometry that is based on a General Electric (GE) 90 fan. The Boeing 787-8 class of twin engine aircraft was selected for two reasons. First, the 787-8 GEnx engine cycle's bypass ratio (BPR) of 8.85 is comparable to the GE90's BPR of 9 [8]. Second, in terms of fleet scenario, the 787-8 is in the same category as the "N+1" next generation of

conventional tube-and-wing aircraft needed to realize the stringent noise goals set by NASA's Environmentally Responsible Aviation (ERA) program [6], [9]. The EAB is not specific to the GE90 engine cycle, but the use of an existing powerplant, for which relevant cycle information is widely available, allowed meaningful analysis to be carried out. Results suggest that for a vane exit angle between 30-35 degrees, the equivalent drag coefficient is about 1.2 based on total aircraft propulsion system fan area. According to ATA, for a 787-8 class aircraft, this has the potential to increase the approach glidescope angle from the conventional 3 degrees to 4.5 degrees at constant flight speed, with a corresponding overall noise benefit of 3 to 4 dB.

The EAB appears to hold promise in meeting NASA's ERA quiet aircraft goals, although there are a number of technical challenges that must be first overcome to realize the full potential of quiet drag in a realistic engine environment. As such, ATA is currently engaged in a more detailed analysis of the EAB's potential and is working with MIT in the development effort.

The primary challenge of the integrated EAB is the behavior of swirling outflow in the presence of a pylon duct bifurcation. MIT is tasked with the concept development effort for the assessment of pylon effects on swirling exhaust flows in a realistic operating environment. A second challenge involves the design of VEGVs to operate in conventional (un-deflected) and air-brake mode. Previous work on variable fan stage OGVs for a different application by Dunbar [10] suggests this challenge should be surmountable. Finally, it is important to quantify the effects of the swirling outflow on fan noise and operation due to re-matching of the core engine [3]. This challenge is currently being explored by ATA using engine cycle analysis software coupled with a simple noise code.

The objective of the advanced study is to analytically quantify the swirl-drag-mass flow relationship of an integrated EAB for model scale aero-acoustic testing in the 4-BB and 5-BB nozzles at the NASA Aero-Acoustic Propulsion Laboratory (AAPL). The 4-BB and 5-BB are dual-stream nozzles of BPR 8 and fan diameter 24.5 cm [11]. Both nozzles share the same fan flow geometry but the 4-BB nozzle has an internal plug in the core stream whereas the 5-BB nozzle has an external plug. Furthermore, the AAPL facility provides anechoic testing services in aircraft noise reduction, with an emphasis on engine nozzle and fan components [12]. Two types of EAB test articles will be evaluated in AAPL using model scale tests:

- Swirling exhaust flows generated by a row of periodically spaced, full-span turning vanes to create data sets that address EAB potential for future novel propulsion systems.

- Integrated EAB with conventional (baseline) and alternative pylon configurations to address practical challenges associated with engine installation.

The objective of the model scale tests is to experimentally verify the swirl-drag-mass flow relationship and obtain noise measurements for typical HBPR nozzles with flows representative of current and future EAB configurations. Measurements will include the far-field noise, nozzle gross thrust force, and fan and core stream mass flows. The experiments will also be run at a wider range of operating conditions to map out a larger design space.

1.2 Review of Previous Work

1.2.1 Overview

A selected literature review is presented in this section to introduce the concept development and associated challenges of quiet drag generation from swirling outflow in (1) the "swirl tube" concept, and (2) the EAB integrated with a pylon duct bifurcation.

1.2.2 The Swirl Tube

For conventional high-drag devices such as flaps and slats, there is a strong correlation between drag and noise, as suggested by Smith [13]. Upon cleaning up the noise sources by suppressing the flow features around these devices, drag is also reduced. The swirl tube shown in Figure 1–1, then, is a departure from this noise-drag correlation because the noise does not increase with drag, until the flow becomes unstable, as shown in Figure 1–2.

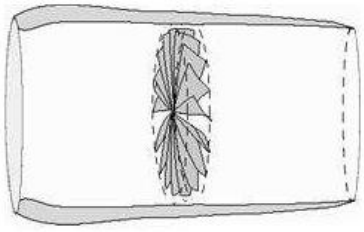

Figure 1–1: Ram pressure-driven swirl tube concept, adapted from [2].

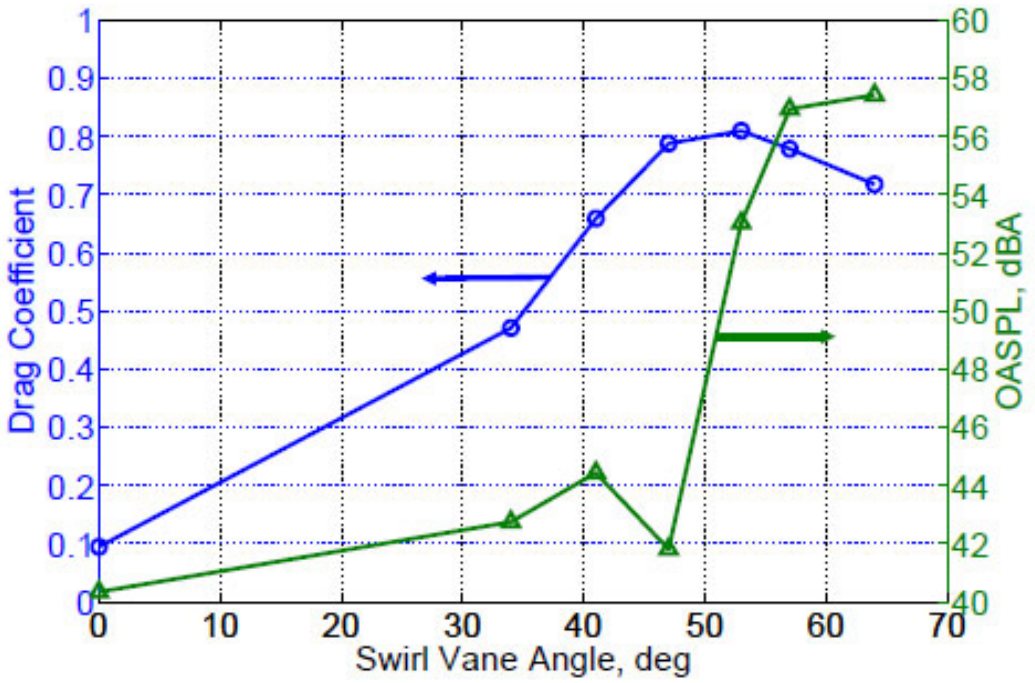

Figure 1–2: The relationship between C_D, swirl vane angle, and overall sound pressure level (OASPL) suggests that a high-drag, low noise configuration exists at a swirl vane angle of 47 degrees. Beyond this vane setting, unsteady vortex breakdown causes an increase in noise, adapted from [14].

The swirl tube device has a demonstrated maximum drag coefficient of 0.8, based on through flow area, and a far-field noise signature of 44 dBA when extrapolated to full-scale. The full-scale size corresponds to the CMI SAX-40 conceptual design fan diameter of 2.16 m, and an estimated observer distance of 120 m at a point directly below the aircraft on a conventional 3 degree glidescope. This is below the noise levels of other aircraft noise sources and quieter than the background noise in a well-populated urban area. Beyond a critical swirl vane angle of approximately 50 degrees, the stable swirling flow transitions into vortex breakdown close to the exit of the duct. In this setting, the device is around 15 dB louder due to scattering noise from the unsteady flow structures in the burst vortex close to the solid duct surfaces as shown in Figure 1–2. Thus the vortex breakdown instability sets the limit of swirl tube capability in terms of the noise-drag relationship near a swirl vane angle of 50 degrees [7], [14].

1.2.3 Engine Air-Brake

The engine air-brake uses variable exit guide vanes downstream of a high bypass ratio fan rotor to produce a drag-generating, quiet swirling exhaust flow as shown in Figure 1–3. Traditionally, the fan exit guide vanes (FEGVs) are used to turn the swirling flow from the fan rotor in the axial direction to maximize thrust production. When operating as an EAB however, the FEGVs are turned using an actuation mechanism to exhaust a swirling outflow.

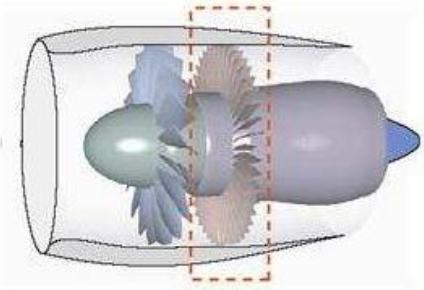

Figure 1–3: High bypass ratio fan rotor with variable VEGVs to create swirling outflow, adapted from [3].

During this time, the swirling outflow emanating from the turbofan engine exhaust generates so-called "equivalent drag" in the form of a thrust reduction. Equivalent drag is defined as a reduction in system net thrust of the swirling case with deflected FEGVs from the baseline, non-swirling configuration. The non-dimensional equivalent drag coefficient developed by ATA is given by Equation 1.3,

$$C_D = \frac{F_0 - F_{EAB}}{qA_{ref}} \tag{1.3}$$

where A_{ref} is the fan inlet area and the dynamic pressure q is defined as,

$$q = \frac{1}{2}\rho_\infty V_\infty^2 . \tag{1.4}$$

The resulting equivalent drag, if quiet, will enable the aircraft to fly a steeper flight trajectory. Table 1.1 presents the estimated overall benefit in terms of noise for several conventional tube-and-wing aircraft on approach.

Table 1.1: Estimated equivalent drag required for glidescope changes on several conventional tube-and-wing aircraft, provided by ATA.

Commercial Aircraft					3 to 4 degrees		3 to 6 degrees	
					2.5 dB overall noise reduction (under flight path)		6 dB overall noise reduction (under flight path)	
Model	Approach Speed (m/s)	Landing Mass (kg)	Wing Ref. Area (m^2)	Total Fan Area (m^2)	Wing Area C_D	Fan Area C_D	Wing Area C_D	Fan Area C_D
737-700A	66.4	58,000	125	3.77	0.03	1.01	0.09	3.04
767-300	74.7	145,000	283	7.57	0.03	0.86	0.08	2.59
777-200ER	71.1	213,000	428	15.33	0.03	0.80	0.09	2.40
787-8	72.0	166,000	387	12.49	0.02	0.72	0.07	2.17

Another concept that can be used to exhaust swirling outflow is the idea of deployable swirl vanes in a long mixer duct as shown in Figure 1–4. Swirl vanes are stowed during take-off and cruise and deployed when required on approach.

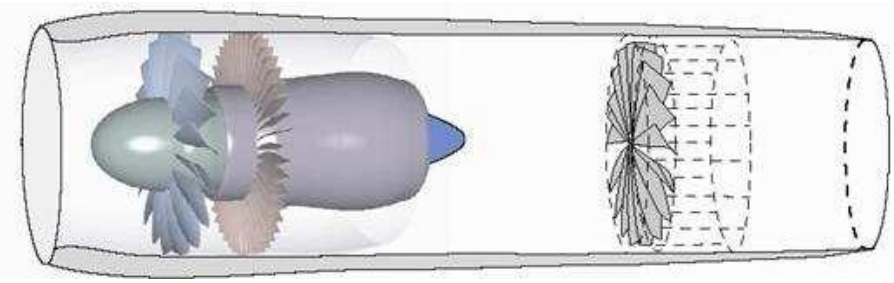

Figure 1–4: Deployable swirl vanes in a turbofan mixer duct, adapted from [3].

There are a number of technical challenges that must be overcome to realize the full potential of swirling exhaust flows for quiet drag in real engine environments. These include:

- Potential loss of swirling flow due to the presence of a pylon and duct bifurcation in the fan stream.
- Design of VEGVs to operate in conventional (un-deflected TE) and air-brake mode (deflected TE).
- Effect of swirling outflow on the fan rotor and core engine performance in terms of operational re-matching and noise.

In addition to these primary challenges, a number of secondary issues including cost, complexity, and maintenance must be assessed in order to justify the use of quiet drag EAB devices in future low-noise aircraft configurations. Each technical challenge is discussed in the following sections.

1.2.4 Pylons

The key challenge associated with quiet drag generation on an integrated EAB is the potential loss of swirling exhaust flow due to the presence of a pylon in the fan stream. Engines are supported to the aircraft wing by pylon duct bifurcations. The pylon serves two purposes; to carry the structural load of the engine, and to route services such as fluid lines, electrical harnesses for power generation, and the pneumatic duct for bleed air to the aircraft cabin [15].

The engine is attached to the pylon via front and aft engine mount adaptors that fit to their counterparts on the pylon. On the engine side, these mounts are usually installed on the intermediate case above the high pressure compressor and the turbine frame. On the pylon side, mounts are attached to an aerodynamically faired framework that leads to the forward and aft wing spar. The mounts transfer engine side loads, vertical loads, and torque to the pylon. For some engines, such as the CFM56-5A, the front mount also transfers the thrust force but on others, such as the GE90, thrust is transmitted via the aft engine mount into the engine pylon. This requires the use of two thrust links to transfer force from the intermediate compressor case to the aft mount [15], [16]. Figure 1–5 shows the arrangement of the engine mounts and location of the thrust links on the CFM56-5A and GE90 engines. Depending on the proximity of the fan duct bifurcation to the fan stage, locally asymmetric outlet guide vanes (OGVs) are employed to accommodate the pylon’s upstream influence.

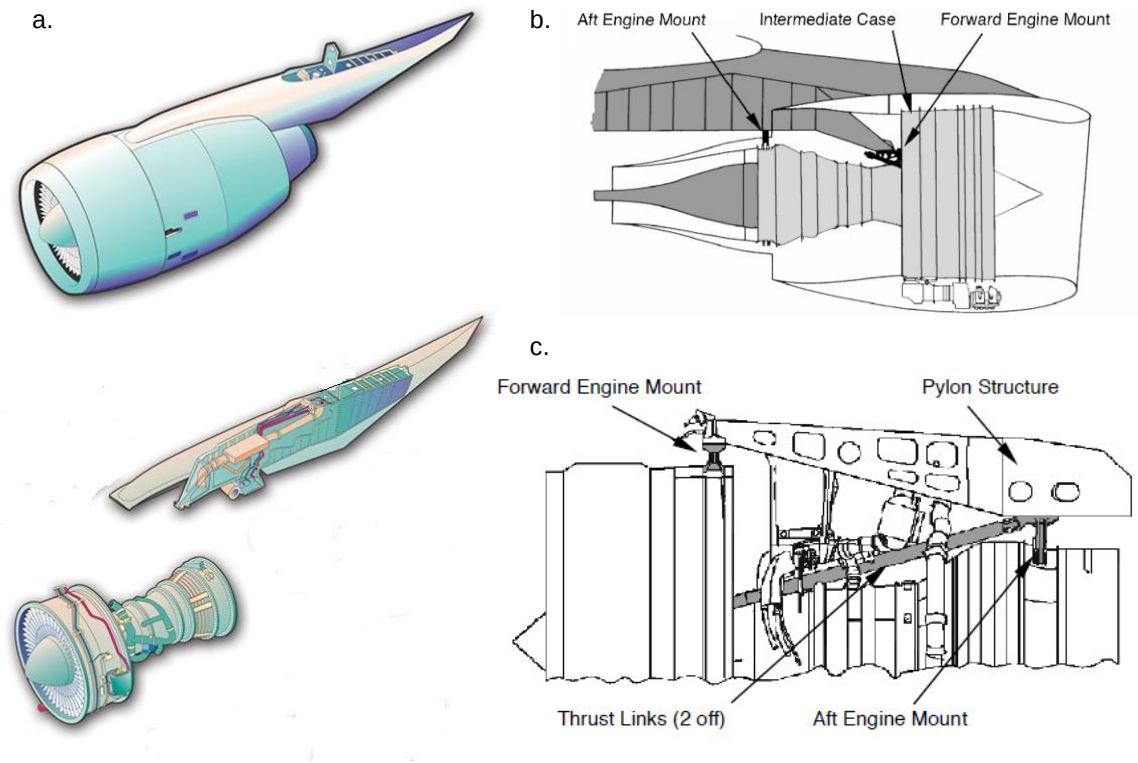

Figure 1–5: a. Exploded view of a pylon installed on the CFM56-5A [17], b. Location of the forward and aft mounts in the fan stream of the CFM56-5A, c. Location of the thrust links connecting the compressor case to the aft mount on the GE90 [15].

1.2.5 Design of VEGVs

The use of variable stator technology in axial compressors of conventional turbofans is in wide use today so solutions to the second challenge can follow a similar path, although the additional loading requirement and complexity for guide vanes to support swirling flows needs yet to be assessed. Past industry patents in the area of variable fan OGVs for different applications suggest this type of technology could be effectively incorporated into a conventional turbofan engine [10].

1.2.6 Fan Rotor and Core Engine Performance

The effect of turbofan re-matching is considered important because the loss of fan stream mass flow from swirling motion will affect the fan's operating point and stability margin. In addition to the fan rotor performance, suction on the core flow will affect the core engine performance

because of an increase in core mass flow. Thus re-matching of the core engine also needs to be addressed. In the initial aerodynamic assessment, ATA found a strong correlation between the fan stage operating point and drag generation capability at approach rotor speed for various VEGV swirl angle distributions. For the maximum achievable drag coefficient of 1.2, the corrected fan mass flow reduced by approximately 5%, corresponding to a similar reduction in the operability margin according to ATA. This reduction is acceptable to maintain an adequate stall margin for the NASA SDT fan rotor considered here [18].

The change in fan mass flow will also affect fan noise because of the different flow interaction with the rotor and subsequent effect on the rotor wake. An investigation of the NASA SDT fan with flight nozzles of different exit areas by Woodward et al. [19] indicates a 5% reduction in fan mass flow at approach rotor speed will increase the fan overall sound pressure level (OASPL) by 1 dB. This is likely due to the combination of a higher rotor incidence angle and corresponding increased rotor wake turbulence levels.

1.3 Problem Statement and Research Objectives

The present investigation examines the feasibility of operating the EAB device integrated with a pylon in a realistic engine environment.

The specific objectives of this investigation are to:

- Quantify the impact of a pylon on the drag and noise of an EAB.
- Explore means to mitigate the potential loss of swirling flow and associated drag.

Specific research questions to be addressed are:

- What type of installation is feasible for the application of the integrated EAB device?
- What is the effect of the pylon and duct bifurcation on swirling exhaust flow in terms of mass flow changes and equivalent drag?
- What is the maximum equivalent drag that can be achieved for stable swirling flows?

The hypothesis is that swirling flow in the presence of a pylon duct bifurcation in an EAB can generate an equivalent drag coefficient between 0.7-1.0 to realize an overall noise benefit of 2.5 dB for several conventional tube-and-wing aircraft on approach.

1.4 Thesis Contributions

The primary contributions of this thesis are:

- Conceptual design of a baseline pylon based on the NACA 0012 airfoil profile for analysis of the integrated EAB.
- Quantification and analysis of equivalent drag, side load, and mass flow results for a family of integrated EAB designs. Results demonstrate swirling outflow can be maintained in the presence of a pylon for all designs but only the aft vane concepts show potential in reaching the target C_D range of values for an overall noise benefit of 2.5 dB on approach.
- Investigation of vortex flow structures in non-uniform swirling flow. Results suggest that asymmetry of the swirling flowfield due to a pylon duct bifurcation leads to the roll-up and spatial dissipation of the emanating vortex sheet into three distinct vortices. Local backflow is not observed suggesting a different vortex breakdown if indeed instability is reached.

1.5 Synopsis of Chapters

Chapter 2 provides details for the preliminary two-dimensional computational fluid dynamics (CFD) analysis of the pylon-cascade geometry used to explore the extent of the expected separation with turning vanes, quantify the downstream residual flow turning, and characteristic grid density requirements and sensitivity of the choice of turbulence model. Chapter 3 presents the conceptual design of the baseline (straight) pylon including design constraints, selection of a realistic turbofan engine environment, details of a roadmap used to design the pylon, the conceptual design and a brief overview of its detailed design and construction. Chapter 4 presents a detailed account of the three-dimensional CFD investigation including results and analysis of the baseline and alternative pylon configuration calculations, and a discussion of the major outcomes. Chapter 5 discusses the analysis of ATA's three-dimensional CFD simulations, presenting insights into reasons behind the equivalent drag and side load results. Finally, Chapter 6 presents conclusions, implications of the study, and recommendations for future work.

Chapter 2

Preliminary Two-Dimensional Analysis of Pylon-Vane Interaction

2.1 Motivation for Two-Dimensional Analysis

There were two key reasons for starting with a two-dimensional analysis. First, from a simplified perspective of flow over a two-dimensional pylon-cascade geometry, it could be used to investigate the extent of the expected separation and to quantify any residual flow turning downstream of the pylon. Second, from a computational modeling perspective, it was important to characterize the grid density and sensitivity of the choice of turbulence model for the more extensive three-dimensional computations.

2.2 Technical Approach

The technical approach involved conducting a preliminary CFD investigation of pylon effects on two-dimensional pylon-cascade geometry with:

1. 0 degree TE angle (un-deflected) OGVs and,
2. 35 degree TE angle (deflected) turning vanes,

to investigate the pylon's upstream influence, impact of the pylon on the downstream flow field, and quantify the deterioration in flow turning angle. The specific turning vane angle of 35 degrees was selected to correspond to the FEGV deflection that yielded the maximum equivalent drag in the initial study on the SDT geometry performed by ATA.

2.3 Computational Setup

2.3.1 Operating Conditions

The CFD operating conditions were selected to correspond to an inlet Mach number of 0.40 and a fan total pressure ratio and fan total temperature ratio of 1.51 and 1.13 respectively, to simulate take-off conditions. The airfoil profile was taken at mid-span of the SDT low-count OGVs, as described in Hughes [20]. Ambient conditions were taken as 288 K and 1 atm so the total temperature and pressure at the domain inlet was 325 K and 1.51 atm. In addition, a flow turning angle of 32 degrees was specified at the inlet for the turning case to correspond to the mass-averaged angle at mid-span of the rotor-stator mixing plane in the initial CFD analyses conducted by ATA. The outer boundaries were specified as periodic to simulate flow through the full annulus.

The standard k-ω turbulence model was employed because of its robustness and accuracy in dealing with separated flows. More details on the choice of this model are presented in Section 2.3.3. All simulations solved the steady state Reynolds averaged Navier-Stokes (RANS) equations to convergence in ANSYS Fluent.

2.3.2 Pylon-Cascade Cases

The preliminary CFD studies were conducted on flow exiting a row of un-deflected OGVs. The chord and solidity of each OGV at mid-span is 83 mm and 1.51 respectively, allowing 26 blades to be modeled in the full annulus as in the SDT low-count arrangement. The cascade was approximately 1c upstream of a single pylon of chord c (228 mm), represented by a NACA 0012 airfoil profile. The CFD domain outlet was 5.75c downstream of the vanes' trailing edges.

The final grid scheme eliminated the interpolation of cells at the interface joining the upstream cascade grid to the downstream pylon grid to reduce any possible effects of numerical diffusion and thereby more effectively capture the vane TE wakes. The mesh constructed in Gambit consisted of approximately 850,000 cells with wall y+ values over the airfoil surface below 2. Figure 2–1 shows a close-up view of the un-deflected OGV grid in Gambit.

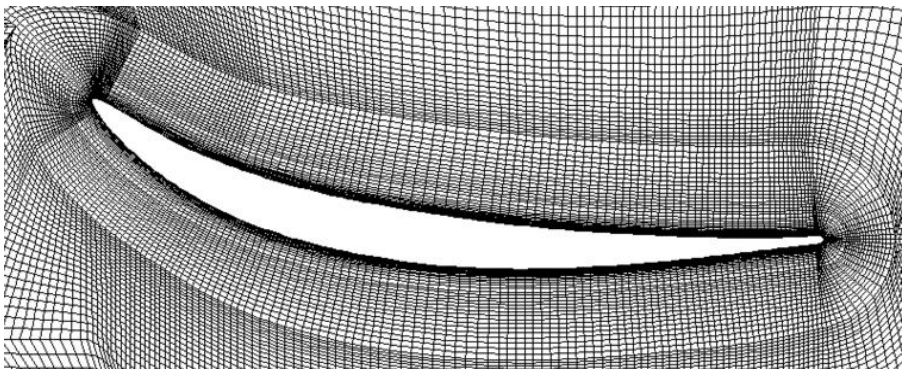

Figure 2–1: Close-up view of the un-deflected OGV grid.

The flowfield results for absolute Mach number in Figure 2–2 show that the vane wakes are captured downstream of the cascade exit. Only the portion of the full annulus cascade close to the pylon is presented; the geometry extends a further 5*c* downstream of the cascade exit. C_p contours in Figure 2–2 show the upstream influence due to the pylon in terms of static pressure field non-uniformity. From Figure 2–3, the non-dimensional change in blade loading between a blade close to the pylon and a blade away from the pylon is 0.04.

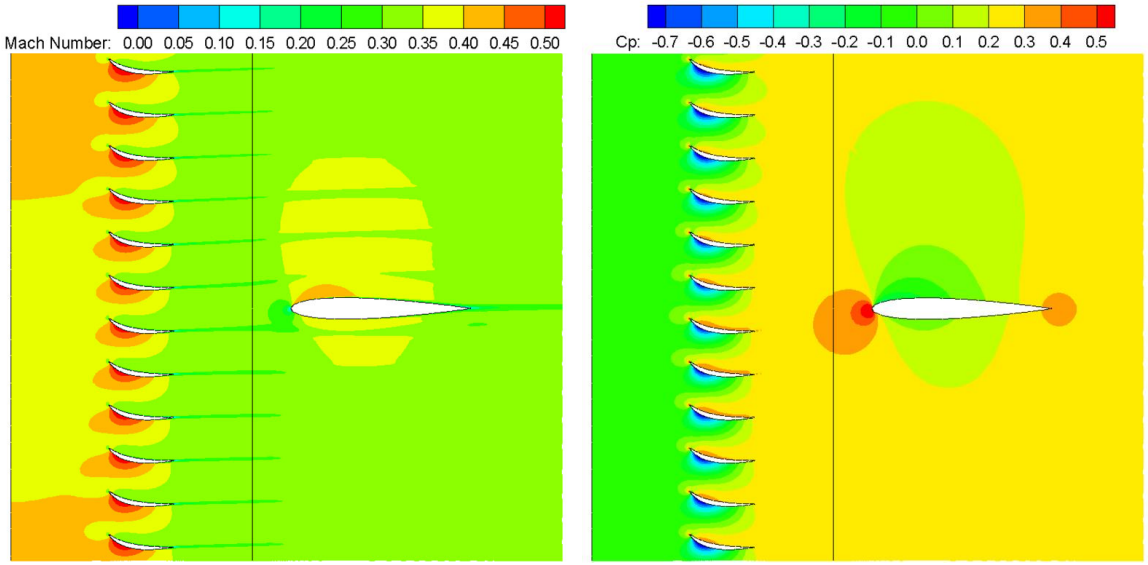

Figure 2–2: Absolute Mach number contours indicate vane wakes are captured downstream of the cascade exit and C_p contours show the upstream static pressure field non-uniformity due to the pylon for the un-deflected OGV pylon-cascade geometry.

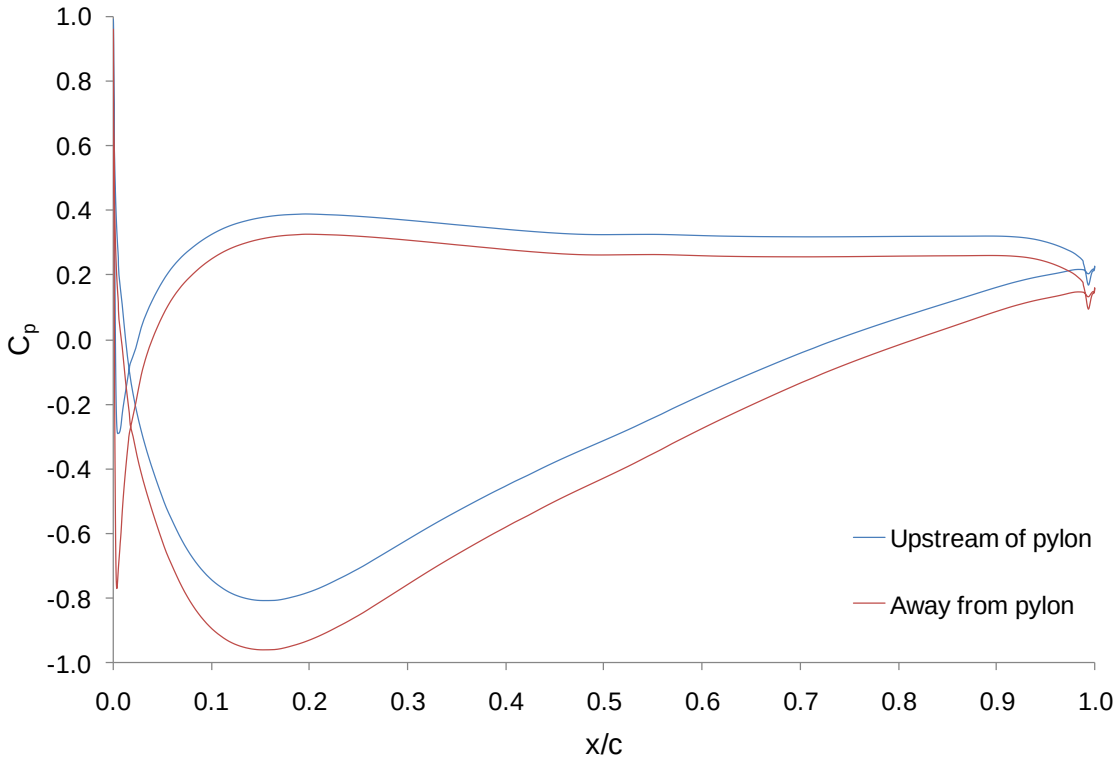

Figure 2–3: Non-dimensional change in blade loading is 0.04 between a blade close to the pylon and a blade further away due to upstream influence of the pylon for the un-deflected OGV pylon-cascade geometry.

As with the baseline cascade, the tuning case involved taking the profile of the SDT 35 degree TE angle OGV at mid-span. The same flowfield dimensions and grid scheme was employed, although the downstream domain was tilted to avoid skewed cells by aligning the domain with the vane TE wakes. The mesh constructed in Gambit consisted of approximately 638,000 cells with wall y+ values over the airfoil surface below 2. Figure 2–4 shows a close-up view of the deflected OGV grid in Gambit.

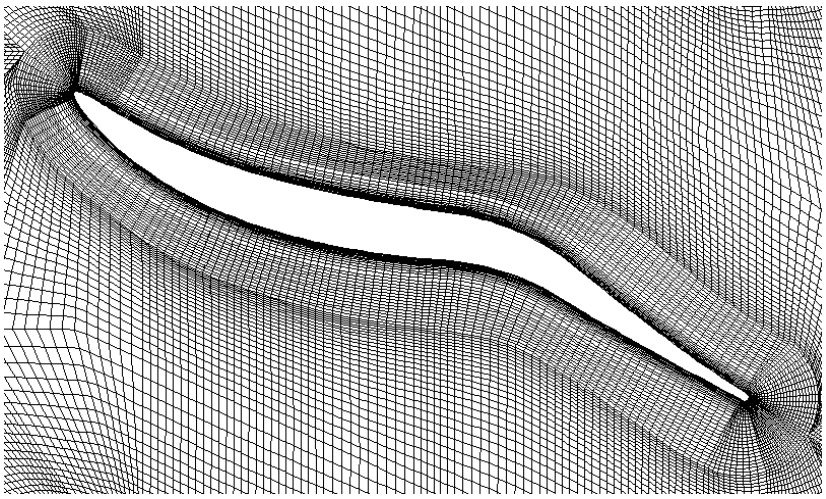

Figure 2–4: Close-up view of the deflected OGV grid.

Quantitative flowfield results for absolute Mach number in Figure 2–5 and axial Mach number in Figure 2–6 show that the deflected OGVs produce a large separation and recirculation behind the pylon. Given the relatively large incidence angle onto the pylon, this was expected although the bulk turning of flow is retained downstream of the pylon. As before, only a portion of the full annulus cascade is presented. C_p contours in Figure 2–5 show the upstream influence due to the pylon is large compared to the un-deflected OGVs, as expected. From Figure 2–7, the non-dimensional change in blade loading between a blade close to the pylon and a blade away from the pylon is 0.80. This is greater than the change in blade loading for the un-deflected OGVs, suggesting locally asymmetric OGVs may be needed to correct for the pylon's upstream influence.

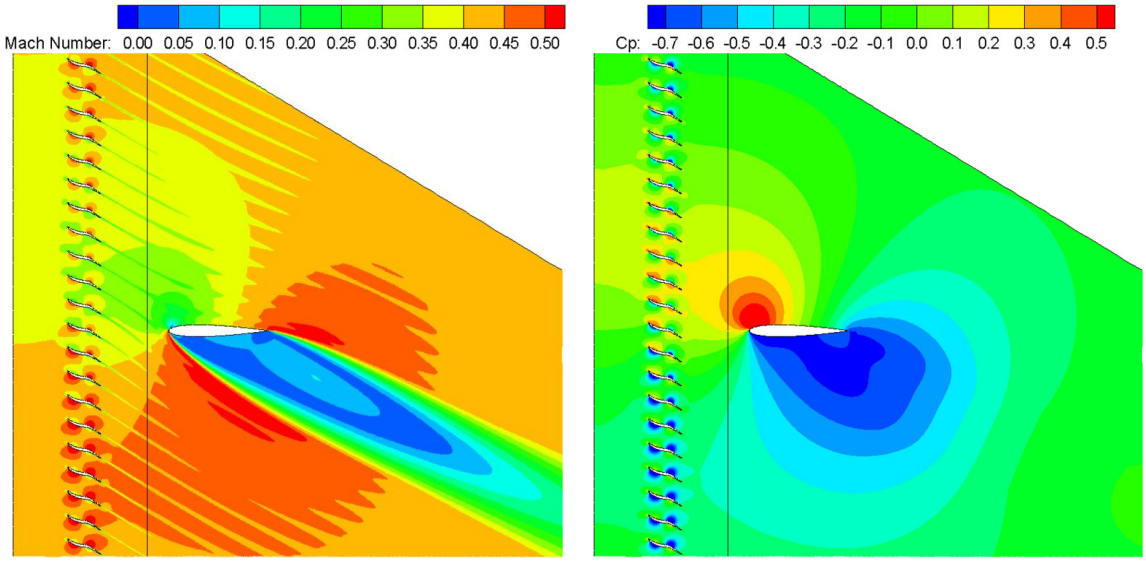

Figure 2–5: Absolute Mach number contours show a large region of separation behind the pylon and C_p contours show the extent of the upstream static pressure field non-uniformity due to the pylon is large for the deflected OGV pylon-cascade geometry.

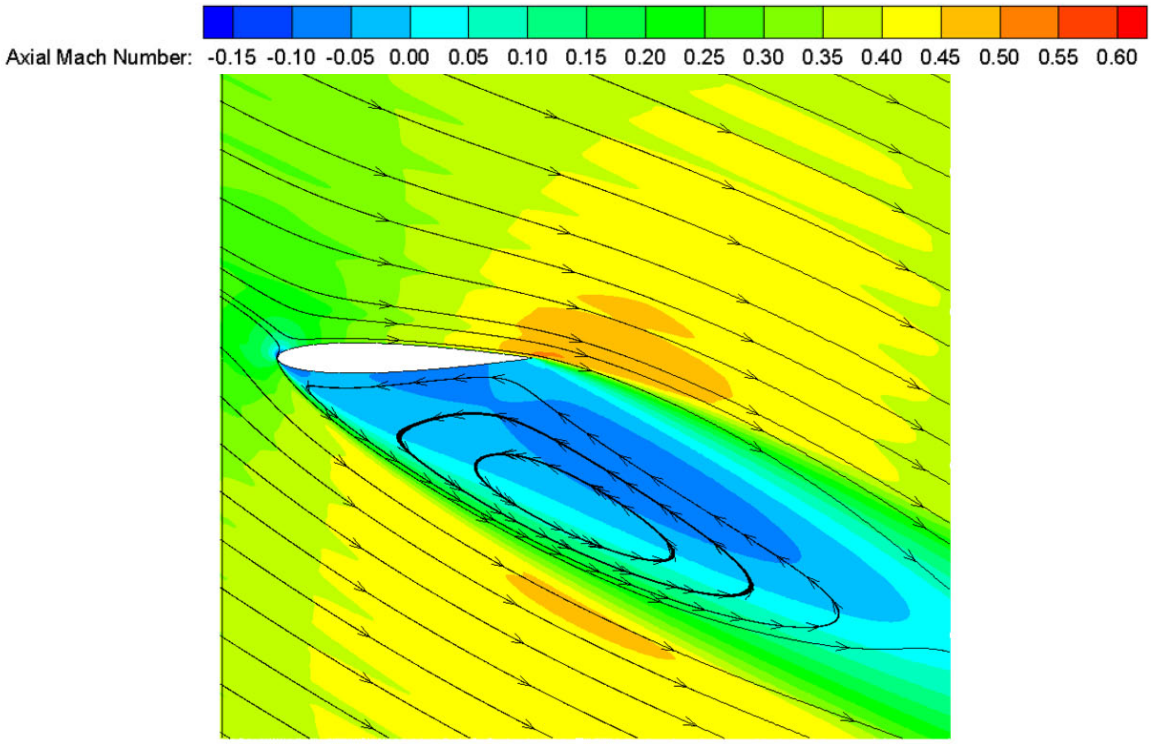

Figure 2–6: Axial Mach number contours show the recirculating flow in the separated region behind the pylon is due to the large flow incidence angle onto the pylon.

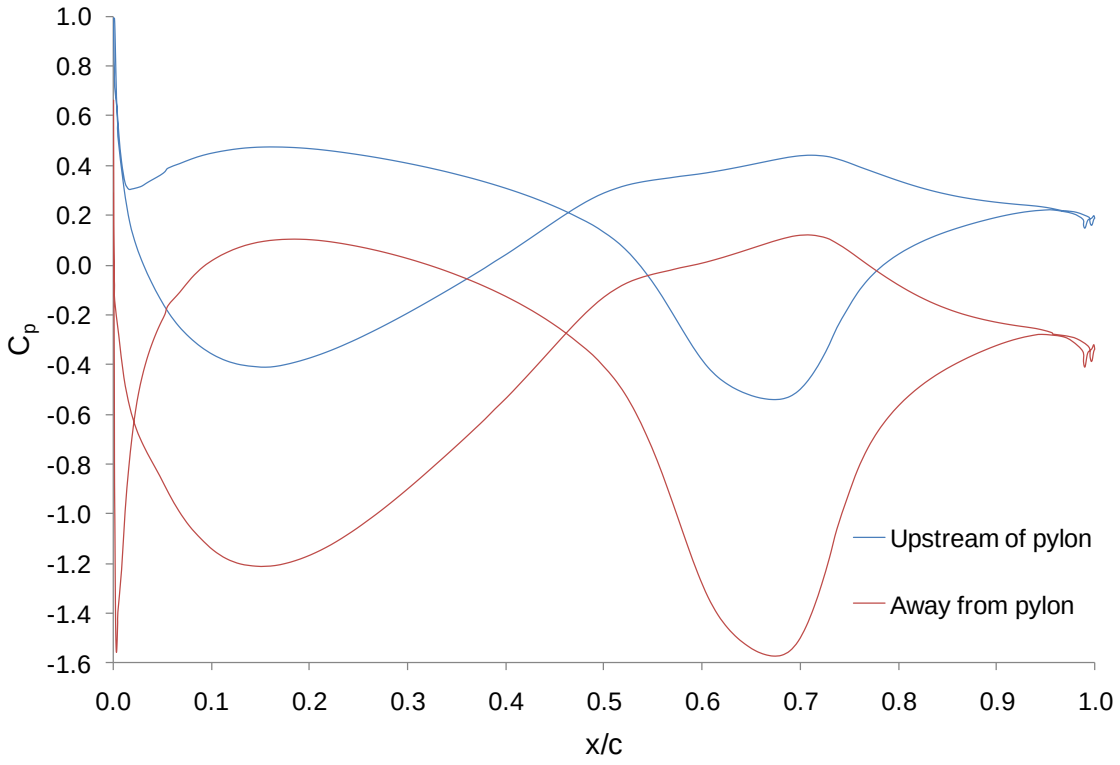

Figure 2–7: Non-dimensional change in blade loading is 0.80 between a blade close to the pylon and a blade further away due to upstream influence of the pylon for the deflected OGV pylon-cascade geometry.

The variation in axial Mach number and flow turning angle κ, defined in Equation 2.1, at the CFD domain outlet are shown in Figure 2–8 and Figure 2–9 respectively for the two cases already introduced and the turning case without the pylon.

$$\kappa = \tan^{-1}\left(\frac{V_y}{V_x}\right) \tag{2.1}$$

The large reduction in axial velocity for the turning case in Figure 2–8 occurs as a result of flow separation around the pylon. The reduced depth of vane wakes in the two 35 degree TE cases compared with the 0 degree TE case is due to lower levels of separation off the vanes. From Figure 2–9, for the 0 degree TE case, the residual flow angle is the vane deviation angle whereas the bulk turning angle is between 25-28 degrees at the domain outlet for the 35 degree case. The last case shows the inlet turning angle of -32 degrees is retained in the absence of the pylon, as expected.

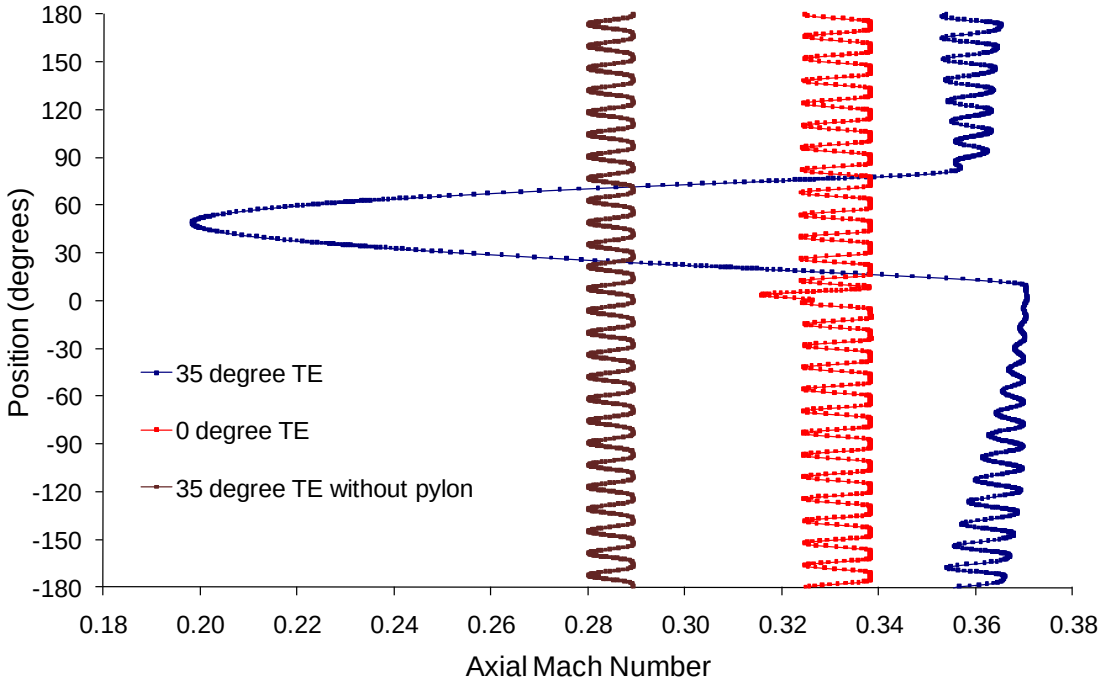

Figure 2–8: The reduction in axial Mach number occurs as a result of flow separation around the pylon.

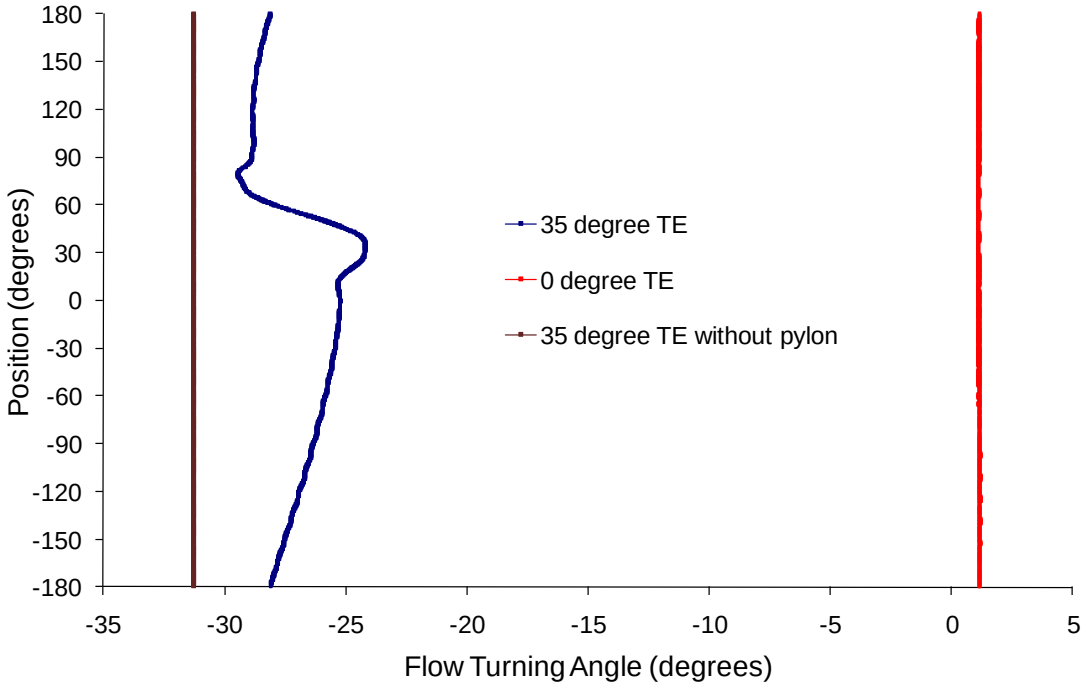

Figure 2–9: The residual flow turning angle is between 25-28 degrees for the 35 TE cascade at the domain outlet.

2.3.3 Turbulence Model Sensitivity Study

To assess the effect of turbulence model choice on capturing details of the separated flow, a turbulence model sensitivity study was carried out on the 35 degree TE OGV pylon-cascade geometry. The one-equation Spalart-Allmaras (S-A) turbulence model was compared to the standard *k*-ω model. The former was employed for its relative simplicity and related reduced computational cost. The latter can accurately model a wider class of flows including flows with large regions of separation [21].

Results for axial Mach number in Figure 2–10 show the standard *k*-ω model better captures details of the recirculating flow by predicting a larger region of low axial velocity in the separated region around the pylon. From Figure 2–11, the standard *k*-ω model predicts a different extent of flow separation immediately behind the pylon compared to the S-A model. Figure 2–12 shows the increased separation off the vanes and pylon in the standard *k*-ω model causes large velocity deficits which result in approximately 2 degrees higher deviation angle on average at the domain outlet. As a consequence, the standard *k*-ω model predicts lower axial Mach numbers at the domain outlet, shown in Figure 2–13.

Based on these findings, it was decided to use the standard *k*-ω model for all two- and three-dimensional analyses.

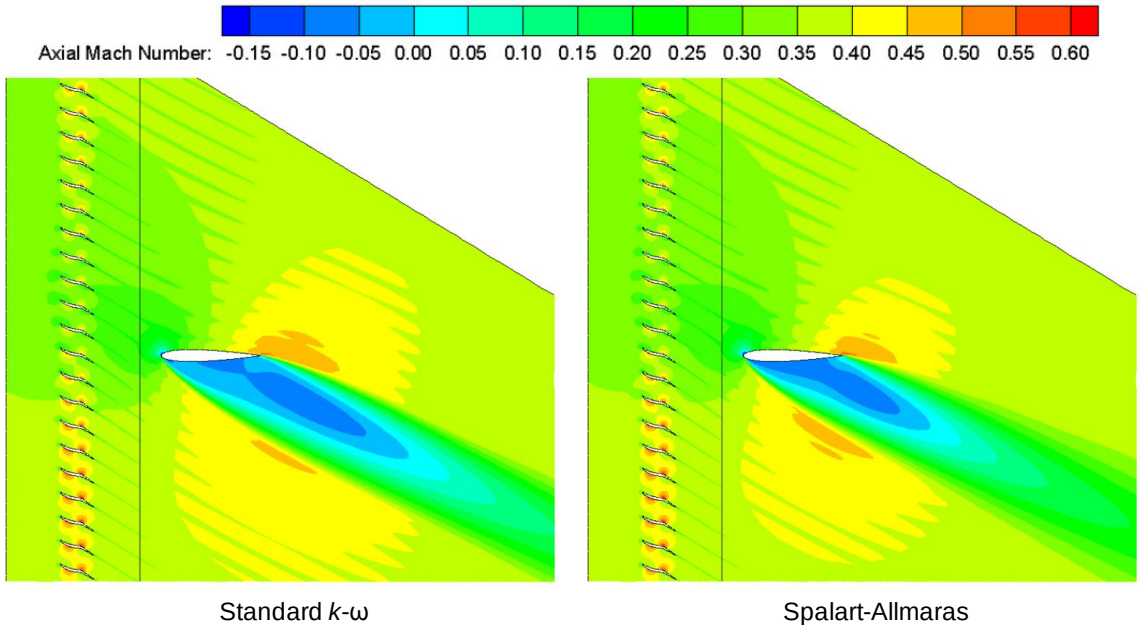

Figure 2–10: Axial Mach number contours show the standard *k*-ω turbulence model predicts a larger region of lower velocity in the separation region compared to the S-A model.

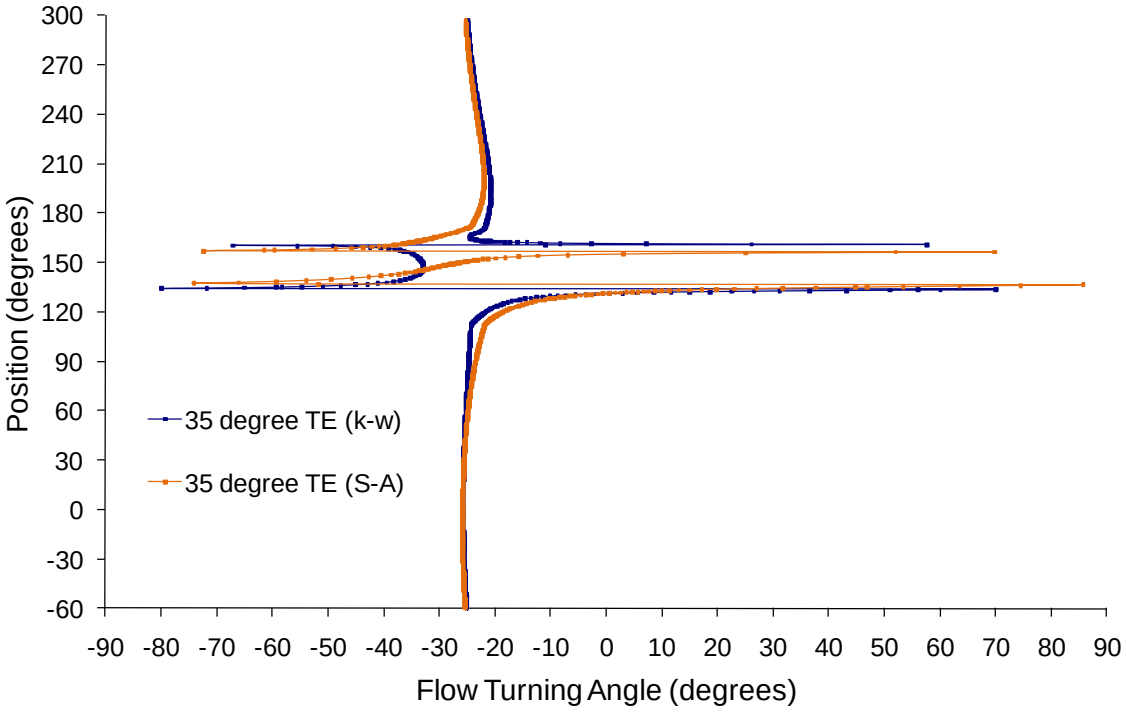

Figure 2–11: The standard *k*-ω model predicts a different extent of flow separation in the recirculating region immediately behind the pylon compared to the S-A model.

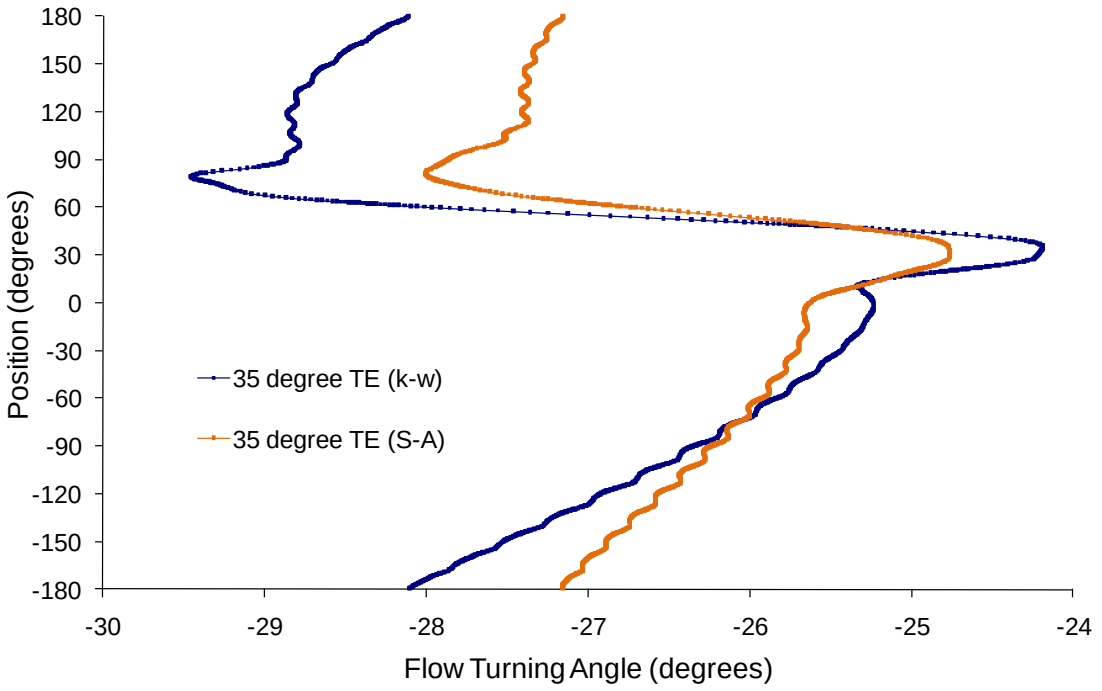

Figure 2–12: Increased separation off the vanes and pylon in the standard *k*-ω model causes larger velocity deficits, resulting in approximately 2 degrees higher turning at the domain outlet.

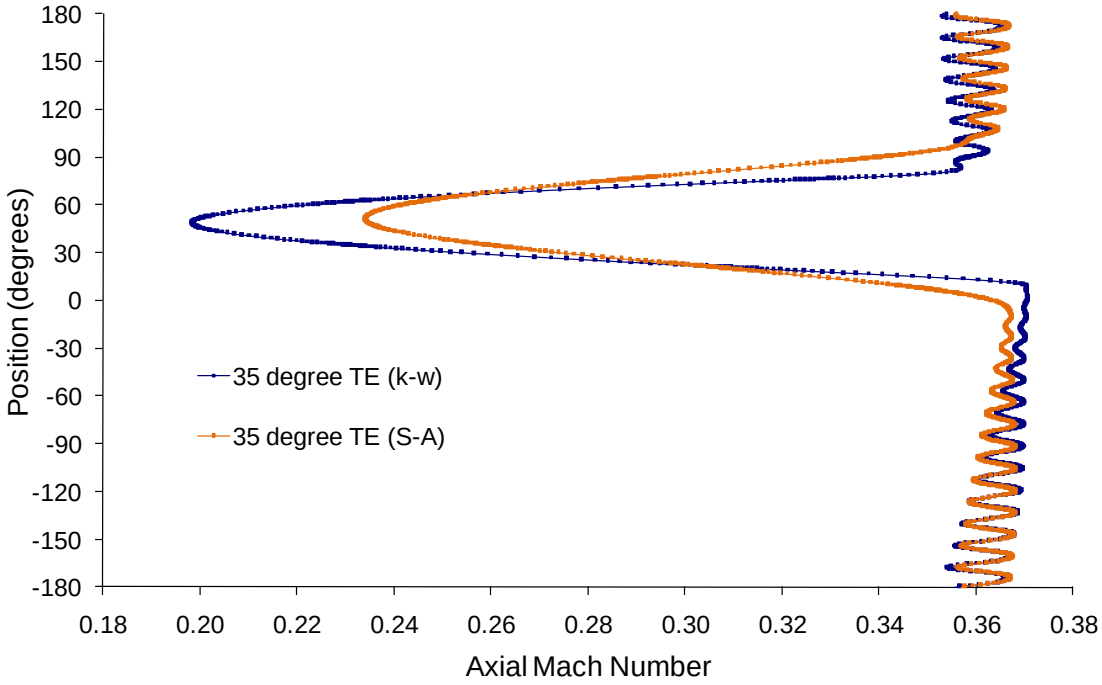

Figure 2–13: The standard *k*-ω model predicts a larger reduction in axial Mach number around the pylon because of increased separation around the pylon.

Chapter 3

Conceptual Design of Baseline Pylon

3.1 Motivation and Design Constraints

In order to assess the feasibility of operating the EAB in a realistic engine environment, the definition of a representative pylon had to be developed. A literature review of pylons in existing turbofan engines yielded information that could be used to design the pylon. With the EAB application in mind, the pylon design must be:

- Representative of current engine installations to yield a realistic engine environment for air-brake feasibility assessment.
- Compatible with both the 4-BB internal plug and 5-BB external plug nozzle at the NASA AAPL facility.
- Designed in a modular fashion to enable parametric vane study and ability to test alternative pylon configurations.

3.2 Engine Selection

The first step in the pylon design was to select the turbofan engine. After performing a broad literature review of several HBPR turbofan engines such as the GE90, CFM56, and the GE CF34, it was decided to select the GE CF34 engine of the Bombardier CRJ Regional Jet aircraft. This is primarily because the -3 series is compatible with the 4-BB internal plug nozzle and the -8/-10 series is compatible with the 5-BB external plug nozzle. Furthermore, sufficient information was found in literature on the CF34's installation configuration [22] including the internal flow path, which together with common aerodynamic installation effects from Naik et al. [23], could be used to fully define the pylon geometry. The CF34 engine series with tail-mounted pylons are shown in Figure 3–1 and Figure 3–2.

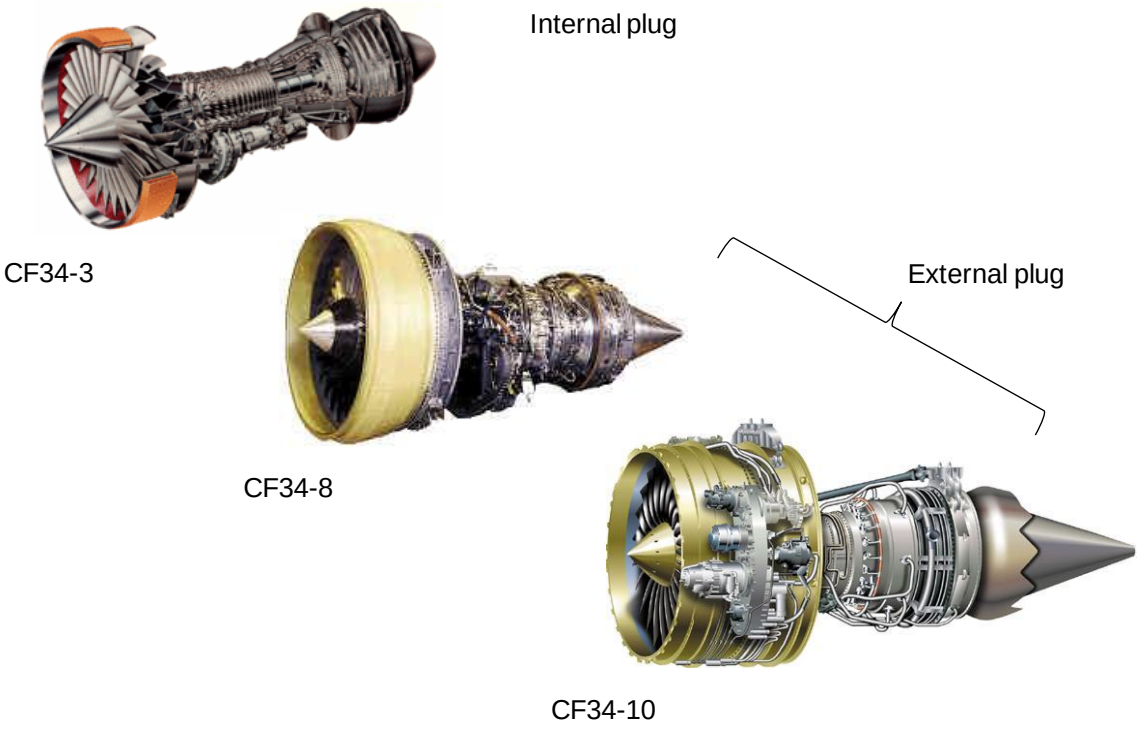

Figure 3–1: The CF34 engine series, showing the -3 internal plug, and the -8/-10 external plug types [24].

Figure 3–2: The CRJ-200 CF34-3 internal plug engine is shown at left and CRJ-900 CF34-10 external plug engine is shown at right with their respective tail-mounted pylons [24], [25].

3.3 Design Roadmap

The conceptual design began by fitting a scaled version of the CF34-3 engine configuration obtained from literature [22] in the 4-BB nozzle geometry. The position of the pylon leading and trailing edges on the engine's internal flow path was estimated by using the location of the forward and aft engine mounts as reference points. Once this was decided, the location of the pylon on the engine was known, as shown in Figure 3–3. Examination of pylon images gathered from literature suggests the symmetric NACA 0012 profile, a variation of which is used in common installations [23], is suitable as the root airfoil because its bulky mid-section can accommodate essential services. This airfoil is used in a prismatic pylon installation that extends from the engine into the freestream. Since a common hardware is the objective, the installation was compared with the 4-BB and 5-BB nozzle geometry to scale the pylon if necessary and when the desired fit was achieved, the full definition was established. Finally, detailed technical drawings for manufacturing the pylon were developed in Solid Works by ATA.

The conceptual design is a prismatic pylon with a NACA 0012 airfoil profile, 14 degree swept leading and trailing edges to simplify the geometry and an extended internal fairing to facilitate compatibility with both the 4-BB and 5-BB nozzles as shown in Figure 3–3 and Figure 3–4.

Detailed design suggests construction in three modular sections: fan flow pylon constructed of aluminum, an aft pylon constructed of stereolithographic (SLA) material and a freestream section also constructed of SLA material. The three sections are held together via aluminum tendons, as shown in Figure 3–5. The outer section protrudes into the freestream and will be hand smoothed to avoid any spurious noise generation associated with sharp edges.

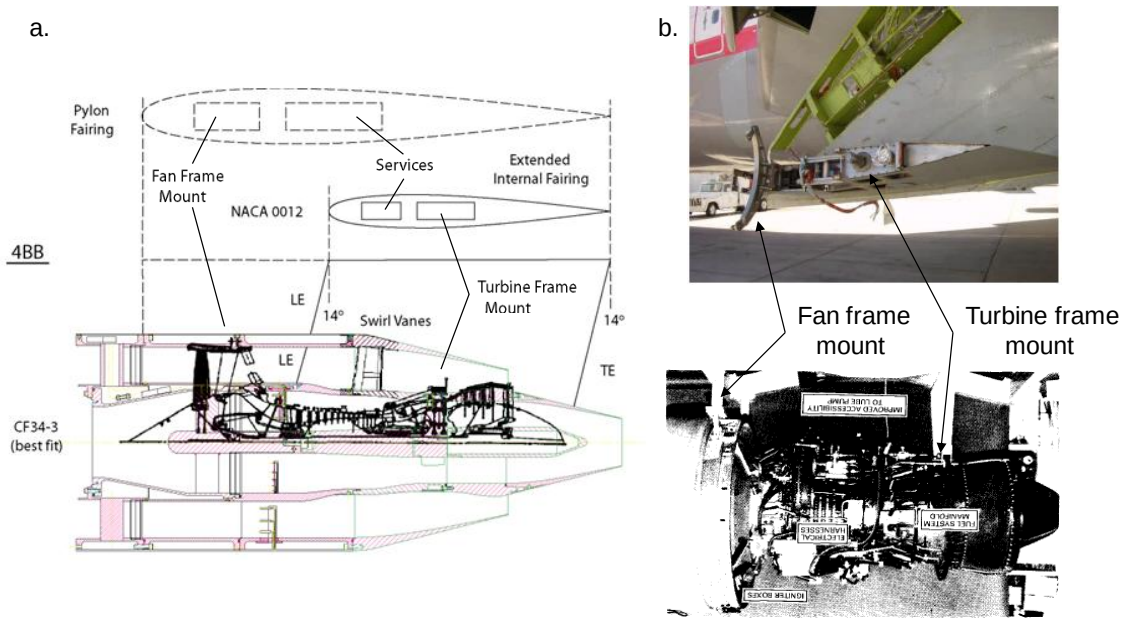

Figure 3–3: Pylon definition for the 4-BB nozzle based on the CF34-3 engine [22], [26].

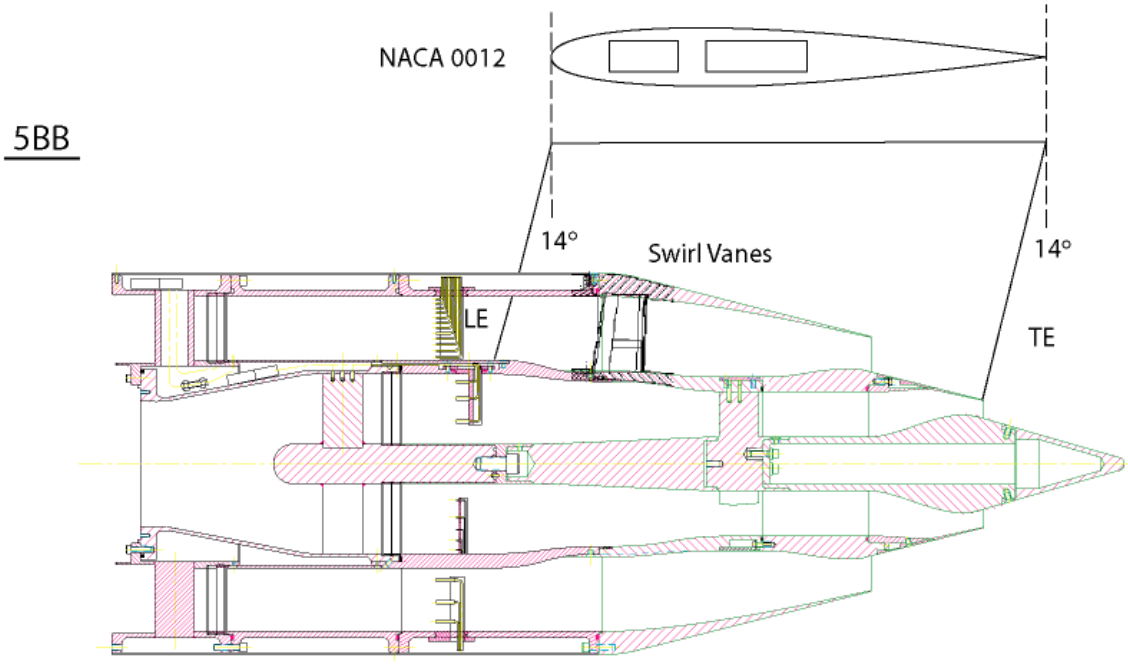

Figure 3–4: The extended internal fairing hardware is the same for both the 4-BB and 5-BB nozzles.

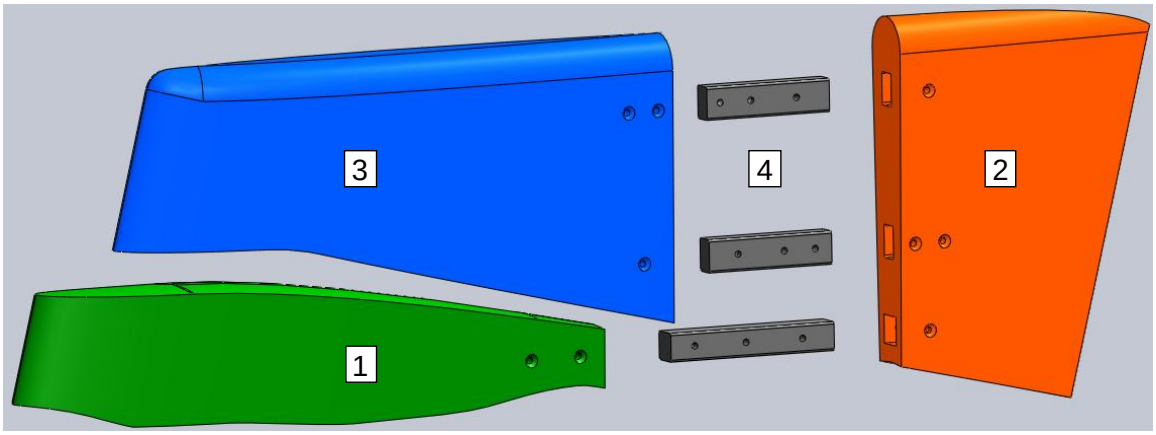

Figure 3–5: The baseline pylon is composed of (1) fan flow, (2) aft pylon, and (3) freestream sections and fastened together by (4) three aluminum tendons. Provided by ATA.

Figure 3–6 shows the pylon installed in the 5-BB nozzle test bed. Loading of the entire pylon assembly is transmitted to the core through the fan flow section via fastners that connect to the core nozzle adapter. Moreover, the pylon aft section will have an un-deflected TE version, shown here, and a deflected TE version for an alternative pylon configuration, discussed in more detail in the next section.

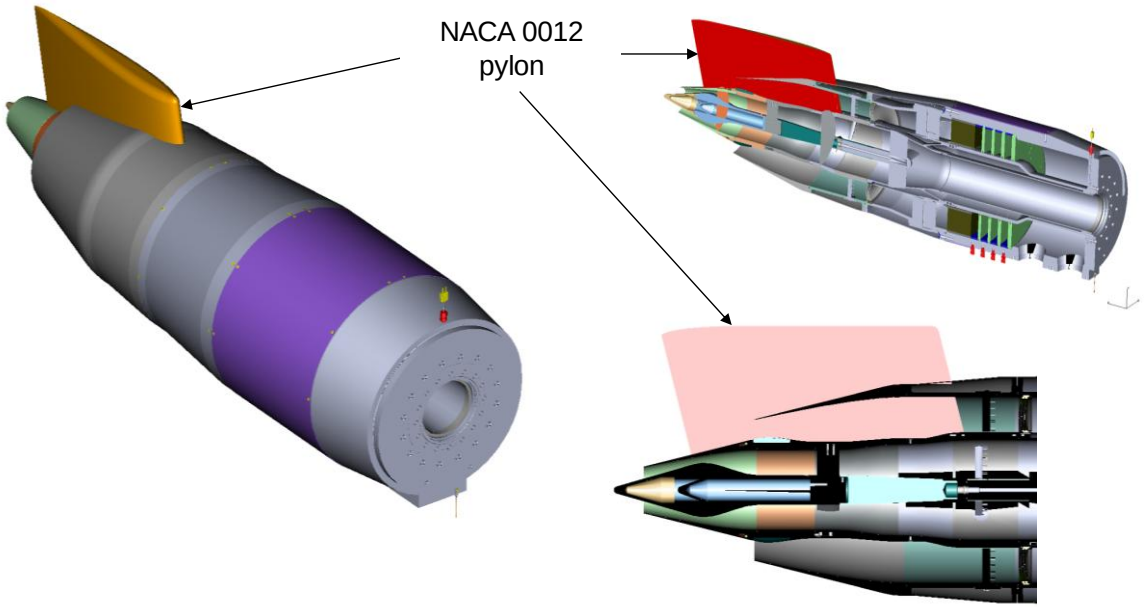

Figure 3–6: The NACA 0012 pylon shown assembled in the NASA AAPL 5-BB nozzle test bed, provided by ATA.

Chapter 4

Detailed Three-Dimensional Analysis of Swirling Flow

A full three-dimensional investigation was needed to fully capture the pressure drag from swirling flow. To assess the feasibility of the EAB in the presence of the pylon, CFD computations were used to model steady flow through the dual stream 4-BB HBPR nozzle without any turbomachinery.

4.1 Control Volume Analysis

A control volume (CV) analysis was carried out to quantify the benefit of the swirling outflow in terms of equivalent drag. Figure 4–1 shows a fixed control volume around the integrated EAB device proposed by ATA. The black dashed lines represent control surfaces over which mass and momentum fluxes are computed to determine the propulsor's thrust. The gray region notionally shows the CFD domain, which shares three boundaries with the control volume, 1: fan stream inlet, 2: core stream inlet, and 3: the freestream inlet. The no-slip core, fan, and plug (also known as the centerbody) walls are enclosed within the definition of the control volume. The other control surfaces are 4: the edge of the cylindrical domain and 5: the upstream boundary.

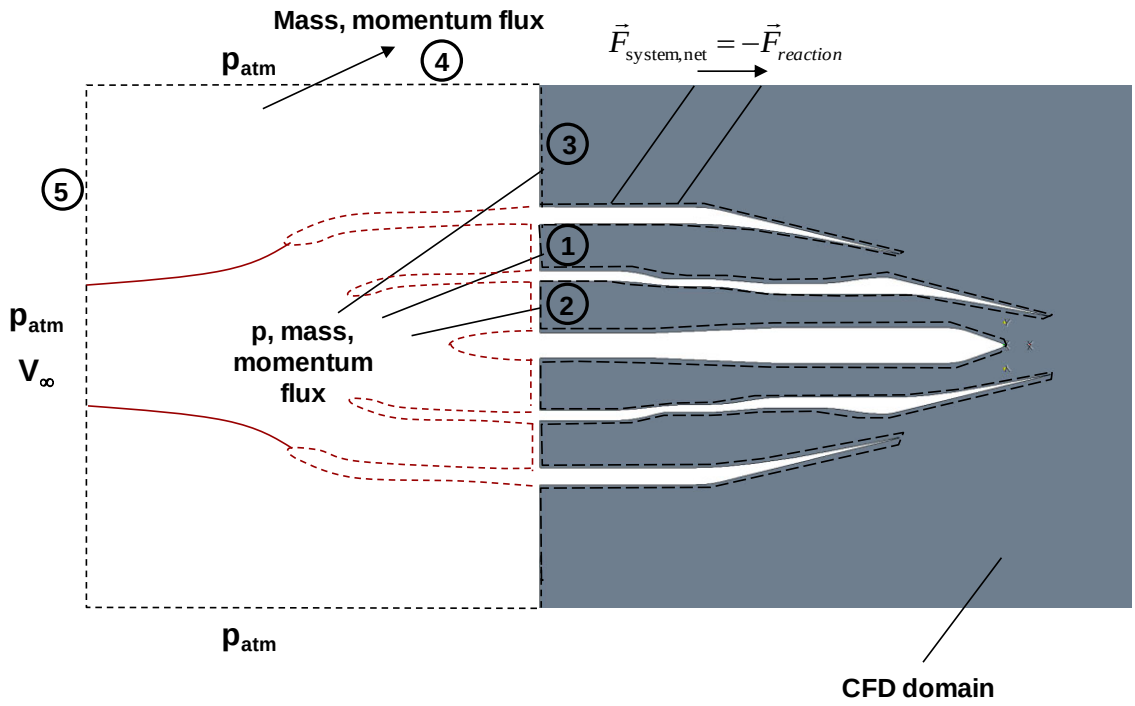

Figure 4–1: Control volume of the integrated EAB (without vanes) used to calculate equivalent drag for swirling outflow, provided by ATA. Flux crossing boundaries are shown by circled numbers.

The following assumptions are applied in this analysis:

1. There is uniform axial flow at stations 1, 2, and 5.
2. The nacelle upstream of the CFD domain shown here by red dashed lines is a notional inlet.
3. The upper and lower boundaries of the CV are sufficiently far away from the device that streamlines there are parallel with the freestream flow.

Conservation of mass across the five boundaries requires,

$$\dot{m}_{fan} + \dot{m}_{core} + \dot{m}_{freestream} + \dot{m}_{u,spill} = \rho_\infty V_\infty A_{upstream} \quad (4.1)$$

Thus the mass flow crossing the side boundaries is given by,

$$\dot{m}_{u,spill} = \rho_\infty V_\infty A_{upstream} - \left(\dot{m}_{fan} + \dot{m}_{core} + \dot{m}_{freestream} \right), \quad (4.2)$$

with the convention that a positive sign implies mass is leaving (thus spillage) and a negative sign signifying mass is entering (thus entrainment).

Conservation of linear momentum in the axial direction for the control volume is given in Equation 4.3. It consists of momentum fluxes across the boundaries, a reaction force, and pressure force terms. The latter includes the force on the fan nozzle, core nozzle, and centerbody walls. The pressure forces relative to ambient pressure on the side (A_4) and upstream (A_5) boundaries are not included because they are zero by definition. Furthermore, although the shear forces on the nozzle walls are much smaller than the pressure forces, they are computed and book kept in the reaction force. The reaction force can be isolated to compute the net thrust of the nozzle.

$$\begin{aligned} &-\rho_\infty V_\infty^2 A_5 + \iint_{A_1} \rho V_x \left(\vec{V}\cdot\mathbf{n}\right) dA + \iint_{A_2} \rho V_x \left(\vec{V}\cdot\mathbf{n}\right) dA + \iint_{A_3} \rho V_x \left(\vec{V}\cdot\mathbf{n}\right) dA + \dot{m}_{u,spill} V_\infty \\ &= -\iint_{A_1} (p - p_\infty) dA_x - \iint_{A_2} (p - p_\infty) dA_x - \iint_{A_3} (p - p_\infty) dA_x - \iint_{\text{fan nozzle}} (p - p_\infty) dA_x \\ &\quad - \iint_{\text{core nozzle}} (p - p_\infty) dA_x - \iint_{\text{centerbody}} (p - p_\infty) dA_x + F_{\text{system,net}} \end{aligned} \tag{4.3}$$

Upon substituting the mass flow carried out the sides in Equation 4.2, the thrust expression is given by,

$$\begin{aligned} F_{\text{system,net}} &= \iint_{A_1} \rho V_x \left(\vec{V}\cdot\mathbf{n}\right) dA + \iint_{A_2} \rho V_x \left(\vec{V}\cdot\mathbf{n}\right) dA + \iint_{A_3} \rho V_x \left(\vec{V}\cdot\mathbf{n}\right) dA \\ &\quad - \left(\dot{m}_{fan} + \dot{m}_{core} + \dot{m}_{freestream}\right) V_\infty + \iint_{A_1} (p - p_\infty) dA_x + \iint_{A_2} (p - p_\infty) dA_x \\ &\quad + \iint_{A_3} (p - p_\infty) dA_x + \iint_{\text{fan nozzle}} (p - p_\infty) dA_x + \iint_{\text{core nozzle}} (p - p_\infty) dA_x + \iint_{\text{centerbody}} (p - p_\infty) dA_x . \end{aligned} \tag{4.4}$$

The system net thrust can be estimated by integrating streamtubes on relevant boundaries in the CFD domain in Fluent to obtain mass flow rates, axial momentum fluxes, pressure forces, shear forces, and then substituting into Equation 4.4.

A second CV was proposed by "un-wrapping" surfaces around the nozzle and using a planar downstream outlet surface instead. The computation of net thrust is independent of the choice of CV and so both CV definitions should give the same result for system net thrust. This property of

the CV analysis is exploited to check for numerical convergence of all steady state simulations in the pylon study. The second CV is illustrated in Figure 4–2.

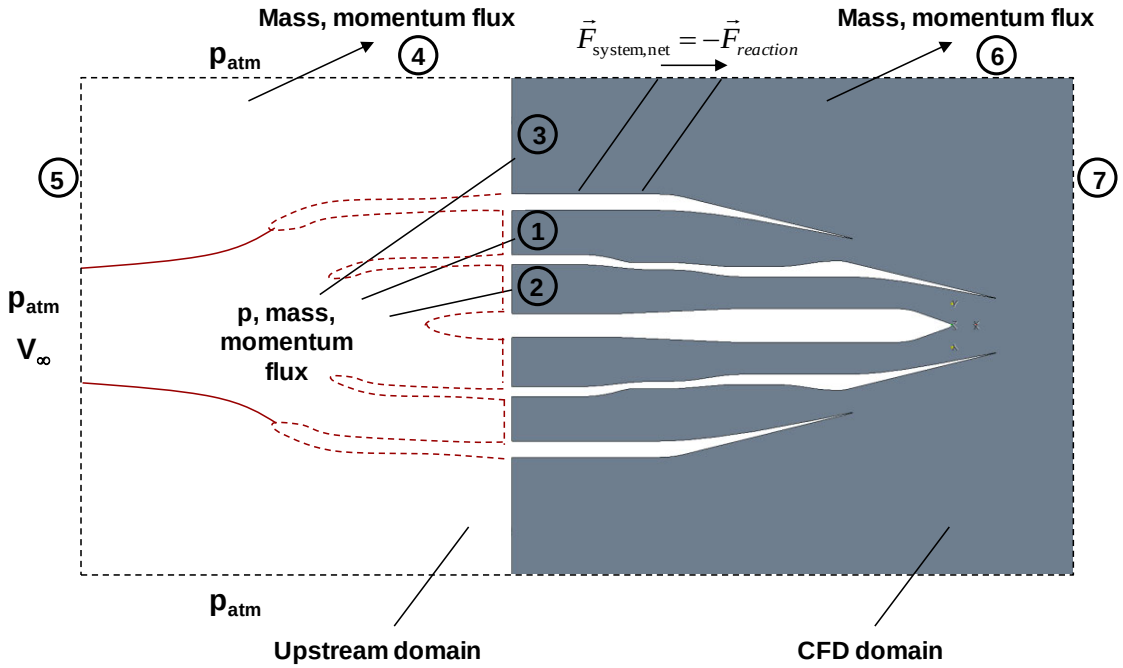

Figure 4–2: Second control volume definition, obtained by un-wrapping surfaces around the nozzle and using a planar downstream outlet surface instead. Flux crossing boundaries are shown by circled numbers.

The new flux boundaries are 6: edge of the cylinder in the CFD domain and 7: the downstream outlet. Mass and momentum flux are spilled across the cylindrical edge of the CFD domain. Mass conservation is the same as before. Conservation of axial momentum is given in Equation 4.5. It includes axial momentum flux terms across the upstream, two sides, and the outlet boundary balanced by the pressure terms on the upstream (A_5) and downstream boundaries (A_7) and the resultant force needed to hold the device in equilibrium. The flow is swirling near the domain outlet so the static pressure there is non-uniform because of radial equilibrium.

$$\begin{aligned} &-\rho_\infty V_\infty^2 A_5 + \dot{m}_{u,spill} V_\infty + \dot{m}_{CFD,spill} V_\infty + \iint_{A_7} \rho V_x \left(\vec{V} \cdot \mathbf{n} \right) dA_x \\ &= p_\infty A_5 - \iint_{A_7} p dA_x + F_{\text{system,net}}. \end{aligned} \tag{4.5}$$

Upon substituting the mass flow carried out the sides from Equation 4.2, the system net thrust is given by,

$$F_{\text{system,net}} = \iint_{A_7} \rho V_x \left(\vec{V} \cdot \mathbf{n} \right) dA - \dot{m}_{outlet} V_\infty + \iint_{A_7} \left(p - p_\infty \right) dA_x . \tag{4.6}$$

As an example, calculation of the equivalent drag coefficient (C_D) for Alternative Pylon Configuration 1 (see Section 4.8) using both CV definitions yields the same result: $C_D = 0.25$.

4.2 Evaluation Metrics

Key parameters for quantifying the potential of an integrated EAB include the equivalent drag coefficient C_D defined in Equation 1.3, side load coefficient C_S, the nozzle discharge coefficient C_d, blockage B, and the swirl parameter S. The reasons which underpin these choices are described below.

$$C_S = \frac{F_S}{qA_{ref}} \tag{4.7}$$

$$C_d = \frac{\dot{m}_{fan}}{\dot{m}_{fan,ideal}} \text{ and } B(\%) = \frac{\left(C_{d0} - C_d \right)}{C_{d0}} \tag{4.8}$$

$$S = \frac{\Gamma_c}{r_c V_x} \tag{4.9}$$

4.2.1 Side Load Coefficient

The side load coefficient C_S in Equation 4.7 is the non-dimensional total horizontal force acting on the EAB. A positive value indicates the resultant side force is acting from the pressure side towards the suction side as shown in Figure 4–3. It is an important metric because swirling flow in the EAB can generate side loads that are of comparable magnitude to the equivalent drag, and the goal is to maximize equivalent drag and minimize the side loads.

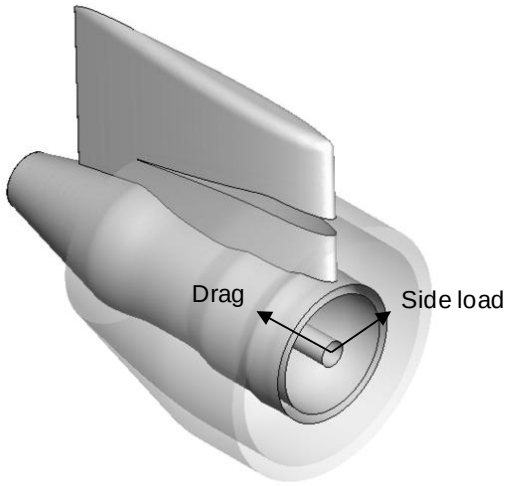

Figure 4–3: The 4-BB nozzle with baseline pylon installed shows a positive side load acts from the pressure side towards the suction side.

4.2.2 Nozzle Discharge Coefficient and Blockage

The nozzle discharge coefficient C_d in Equation 4.8 is a measure of the reduction in mass flow through the fan nozzle due to losses. It is defined as the actual mass flow over the mass flow assuming an ideal expansion to the same static pressure at the nozzle exit. For the EAB application, this is a suitable measure of nozzle performance because changes in mass flow rate indicate changes in the fan operating point [1]. The flow blockage term *B* is a measure of the reduction in the discharge coefficient from the empty nozzle (without pylon and vanes) due to a reduction in flow through area.

4.2.3 Swirl Parameter

The swirl parameter *S* is used to quantify the strength of the asymmetric swirling motion with a high velocity core flow component downstream of the nozzle exhaust in the EAB. In Equation 4.9, V_x is a characteristic axial velocity of the flow [27], and the circulation Γ_c measures the strength of all vortex tubes that thread through a circular contour *C* of radius r_c and cross sectional area *A* [28],

$$\Gamma_c = \iint_A \boldsymbol{\omega} \cdot \mathbf{n} dA = \oint_C \mathbf{V} \cdot dl \quad . \tag{4.10}$$

4.3 Technical Approach for Pylon Study

The technical approach involved conducting analyses of swirling bypass flows in the presence of a pylon duct bifurcation in the 4-BB HBPR nozzle. To investigate the flowfield and the effect of swirling flow on equivalent drag and mass flow changes, ATA conducted analyses of axisymmetric swirling bypass flows in the dual stream, 4-BB nozzle at approach conditions. Guided by these results, the penalty in nozzle performance in the presence of un-deflected swirl vanes at an upstream location and at fan nozzle exit at high power, take-off operating conditions was quantified. The upstream location corresponds to the location of the integrally vaned-disk (visk) hardware that has been manufactured for testing in the NASA AAPL facility. Both locations are shown in Figure 4–4.

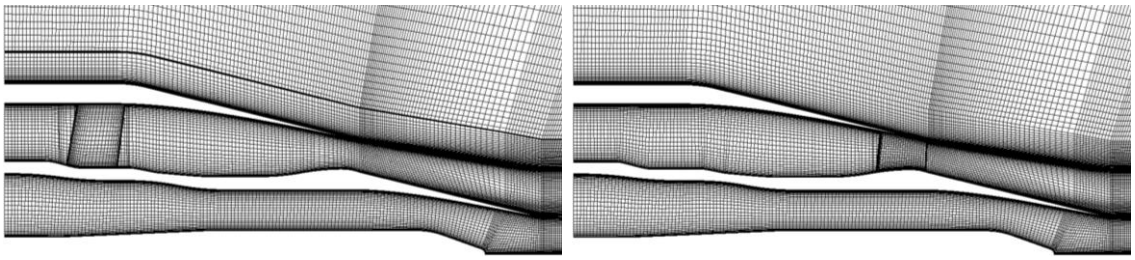

Figure 4–4: Close-up view of the 4-BB nozzle flow path grid showing un-deflected vanes at the upstream and fan nozzle exit locations.

The latter is expected to be the worst case scenario for EAB operation in terms of system net thrust and blockage. After understanding the flowfield response to swirling flows, a detailed investigation of pylon effects on the integrated EAB at approach conditions was carried out with:

1. Baseline Pylon Configuration 1: straight pylon, to allow for consistent performance analysis.
2. Baseline Pylon Configuration 2: straight pylon with un-deflected swirl vanes at the fan nozzle exit, to allow for consistent performance analysis in terms of equivalent drag.
3. Alternative Pylon Configuration 1: pylon TE flap deflected full-span by 35 degrees, to set structural load limits on the baseline pylon design because of the potentially large side loads on the EAB. Results can also guide how much and where the pylon TE flap should be deflected, and the placement and distribution of swirl vanes for maintaining swirling outflow.

4. Alternative Pylon Configuration 2: pylon TE flap deflected partial-span by 20 degrees with swirl vanes at the upstream location, to mitigate any separation and maintain coherent swirling outflow downstream of the fan nozzle exit.

4.4 Analyses of Swirling Bypass Flows in Dual Stream 4-BB Nozzle

The purpose of ATA's swirling bypass flow study was to provide a first-look at the swirling bypass flowfields, and the effect of swirl on mass flow and equivalent drag. A 15 degree wedge of the 4-BB nozzle geometry was used as the CFD solution domain. The wedge allowed for quick parametric studies of the swirl-drag-mass flow relationship and the flexibility to add between twenty to thirty swirl vanes for future analysis. The cross section of the domain is shown in Figure 4–5 and a close-up view of the nozzle flow path is shown in Figure 4–6.

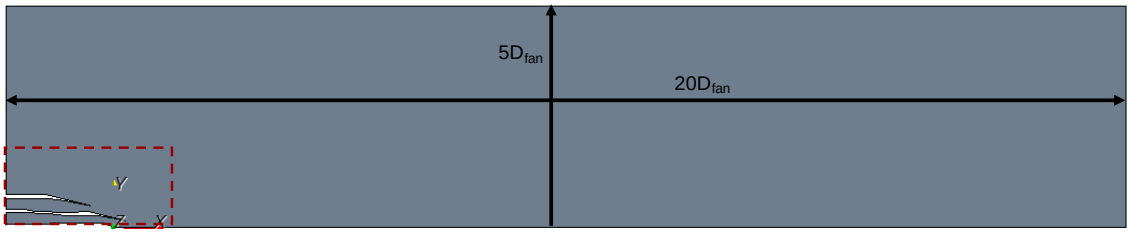

Figure 4–5: CFD solution domain for analysis of swirling bypass flows in the 4-BB nozzle, provided by ATA.

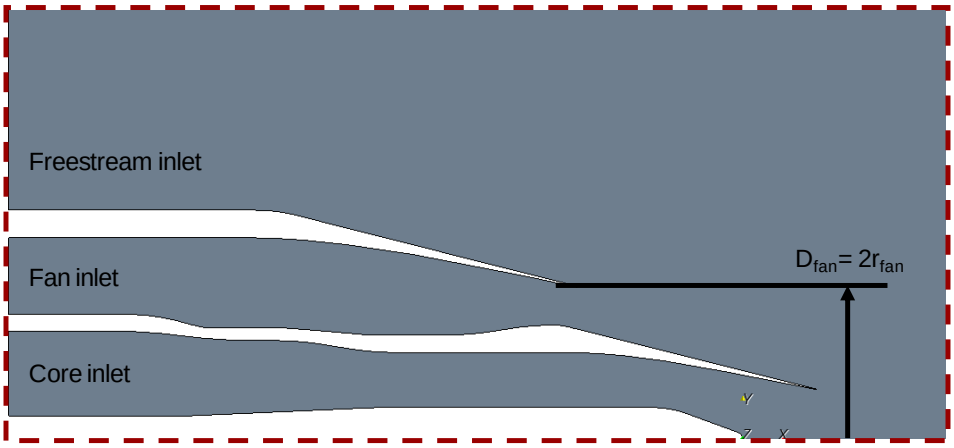

Figure 4–6: Close-up view of the 4-BB nozzle flow path, provided courtesy of ATA.

The radial extent of the domain is $5D_{fan}$ and the axial extent is $20D_{fan}$, where D_{fan} is the SDT fan nozzle diameter (approximately 0.25 m). It consists of three inlet streams: core, fan, and freestream, each with prescribed total temperature and pressure. Constant swirl angles are specified at the fan inlet boundary to simulate axisymmetric swirling flows. The radial and domain outlet boundaries discharge to the ambient atmosphere. It is important to note that since the domain outlet is far downstream of the swirling motion, the pressure defect there from simple radial equilibrium is negligible. This is shown in Figure 4–7 for a constant fan inlet swirl angle of 40 degrees. The assumption of a uniform atmospheric pressure distribution at the domain outlet is therefore reasonable. The sides of the wedge are specified as periodic fluid surfaces to simulate flow through the full annulus.

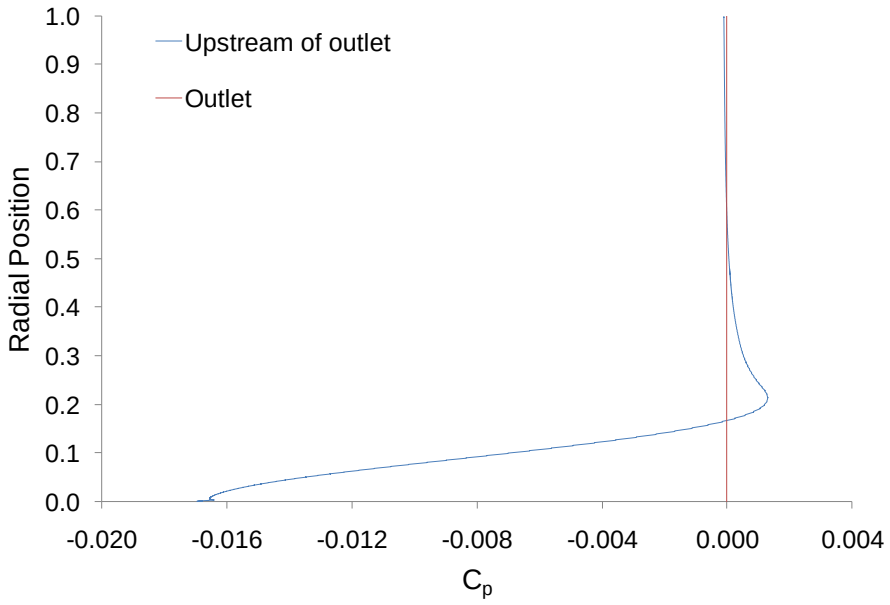

Figure 4–7: The variation of static pressure with radial position for a constant fan inlet swirl angle of 40 degrees at a plane upstream of the domain outlet shows the pressure defect from swirling flow is negligible.

The all-y+ wall treatment was chosen with the standard *k*-ω turbulence model to provide a compromise between full boundary layer resolution near finely meshed regions and the use of wall functions in coarser regions. The solution domain consists of approximately 500,000 cells with wall y+ values over the nozzle surfaces in the range 4-50, which is reasonable for this turbulence model [29]. All simulations solved the steady state RANS equations to convergence in Star-CCM+.

The flight Mach number was selected to be 0.21 to correspond to the approach speed of 140 knots for the Boeing 787-8 class aircraft [30]. The ambient temperature and pressure was 300 K and 1 atm respectively. The approach fan pressure ratio was 1.15 of the SDT fan stage [18], thus the fan nozzle pressure ratio (FNPR) was calculated by multiplying this number by the ram pressure ratio corresponding to the flight Mach number. This analysis assumes the engine inlet is ideal (i.e. $\pi_{inlet} = 1$). The same process was used to pick the fan nozzle temperature ratio (FNTR). The core nozzle pressure ratio (CNPR) was selected by assuming a bypass-to-core jet velocity ratio of 0.7 from cruise conditions. A "hot" core nozzle temperature ratio (CNTR) was selected by preserving the ratio of core-to-fan total temperature from a design point cycle analysis on the 787-8 aircraft as outlined in Equation 4.11,

$$\tau_{core} = \left(\frac{T_t}{T}\right)_{\infty} \times \tau_{fan} \times \left(\frac{598.4}{317.5}\right). \tag{4.11}$$

In addition to a "hot" core, a "cold" core temperature was found by reducing the ratio of core-to-fan total temperature from 1.88 to 1 in the CNTR while keeping the CNPR fixed. A list of the operating conditions for all permutations tested is given in Table 4.1.

Table 4.1: Operating conditions for study of swirling bypass flows in 4-BB nozzle at approach, provided by ATA.

Cases	Freestream PR (Gauge Pressure)	FNPR (Exit Gauge Pressure)	FNTR (Exit Temperature)	CNPR (Exit Gauge Pressure)	CNTR (Exit Temperature)
Hot Core Fan Inlet Swirl Angles: 0 deg 20 deg 40 deg 60 deg	1.03	1.19	1.06	1.21	2.00 (598.4 K)
Cold Core Fan Inlet Swirl Angles: 0 deg 20 deg 40 deg 60 deg	1.03	1.19	1.06	1.21	1.06 (317.5 K)

Constant swirl angles of 0, 20, 40, and 60 degrees for hot and cold cores were specified at the fan inlet boundary to explore the effects of swirling flow on the flowfield. These swirl angles do not correspond to swirl vane TE angles or mass averaged swirl angles at the fan nozzle exit, but cover a broad range for analysis of the flowfield. In all, a total of 16 permutations have been tested for hot and cold core conditions on 4-BB and 5-BB nozzles. Results for mass flows and equivalent drag for the 4-BB geometry are presented in Table 4.2.

Table 4.2: Fan and core mass flows, bypass ratio, and equivalent drag coefficient results for swirling bypass flows in the 4-BB geometry.

	Upstream Swirl Angle	Fan Mass Flow (kg/s) (% change rel to baseline)	Core Mass Flow (kg/s) (% change rel to baseline)	BPR (% change rel to baseline)	Effective C_D based on fan nozzle diameter
Cold Core	0 deg (Baseline)	0.18	0.04	4.83	0.00
	20 deg	0.18 (-1.20%)	0.04 (4.90%)	4.55 (-5.81%)	0.19
	40 deg	0.17 (-6.07%)	0.05 (21.12%)	3.75 (-22.45%)	0.91
	60 deg	0.14 (-20.77%)	0.05 (44.92%)	2.64 (-45.32%)	2.83
Hot Core	0 deg (Baseline)	0.18 (0.00%)	0.03 (0.00%)	6.65 (0.00%)	0.00
	20 deg	0.18 (-1.22%)	0.03 (4.92%)	6.26 (-5.85%)	0.18
	40 deg	0.17 (-6.09%)	0.03 (21.17%)	5.15 (-22.50%)	0.88
	60 deg	0.14 (-20.78%)	0.04 (45.09%)	3.63 (-45.40%)	2.77

Four observations can be made from the results in Table 4.2. First, for a prescribed inlet swirl angle, the fan mass flow is independent of the temperature of the core flow. This is because the ratio of nozzle exhaust pressure to upstream (inlet) stagnation pressure is constant in the fan stream for both cases and unaffected by the core nozzle temperature.

Second, for a given level of inlet swirl, the percent change in core mass flow from the baseline case is independent of the core nozzle temperature. This occurs because the fan inlet swirl sets the core nozzle exit pressure boundary condition from swirling outflow and since the fan is cold for all cases, the core nozzle pressure ratio is always the same, irrespective of the core temperature.

Third, the bypass ratio decreases significantly with increasing levels of inlet swirl. This is because swirling bypass flow generates suction in the core which increases the core exit Mach number and causes the bypass flow to decrease and the core flow to increase, resulting in a significant reduction of the bypass ratio.

Finally, the core mass flow scales with stagnation temperature as,

$$\frac{\dot{m}_{cold}}{\dot{m}_{hot}} = \sqrt{\frac{T_{\mathrm{t,hot}}}{T_{\mathrm{t,cold}}}} = 1.37. \tag{4.12}$$

Comparing absolute Mach number contours for the cold and hot core cases in Figure 4–8 and Figure 4–9 respectively show the two cases produce identical flowfields. This is in agreement with the substitution principle of Munk and Prim from Greitzer et al. [28]. It states that two steady, inviscid flowfields with the same stagnation pressure distributions but different stagnation temperature distributions will produce identical streamline patterns, static pressure fields, and Mach number distributions. The mass flows for the two streams will be different however and scale with the expression in Equation 4.12.

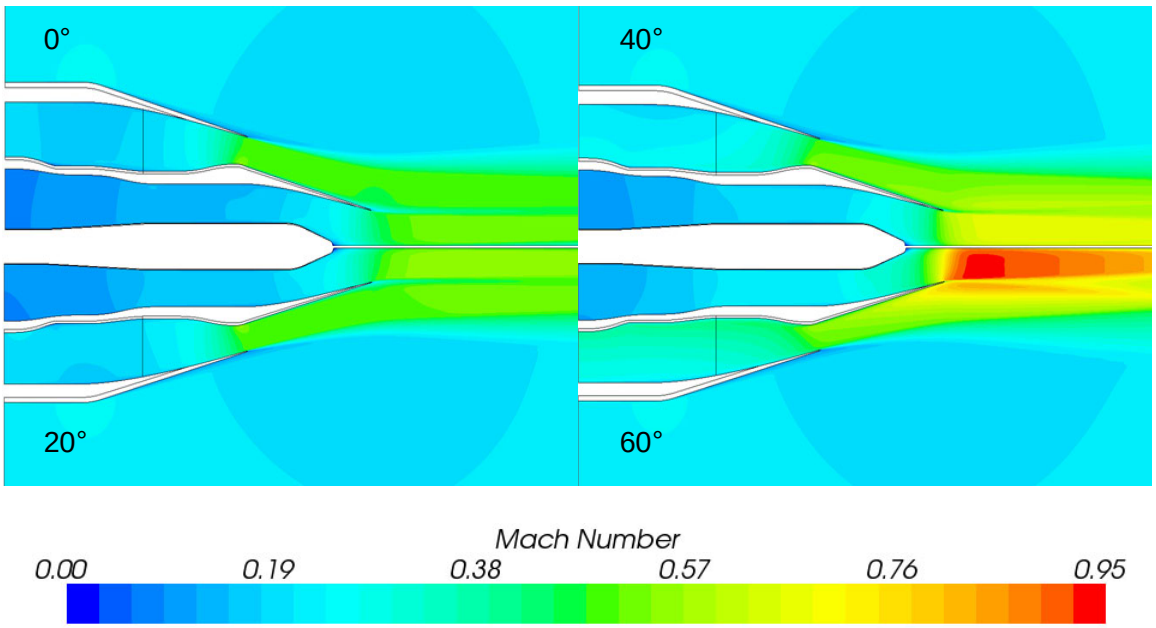

Figure 4–8: Absolute Mach number contours for all fan inlet swirl angles at cold approach conditions in the 4-BB nozzle show no difference to the hot core cases (courtesy of ATA).

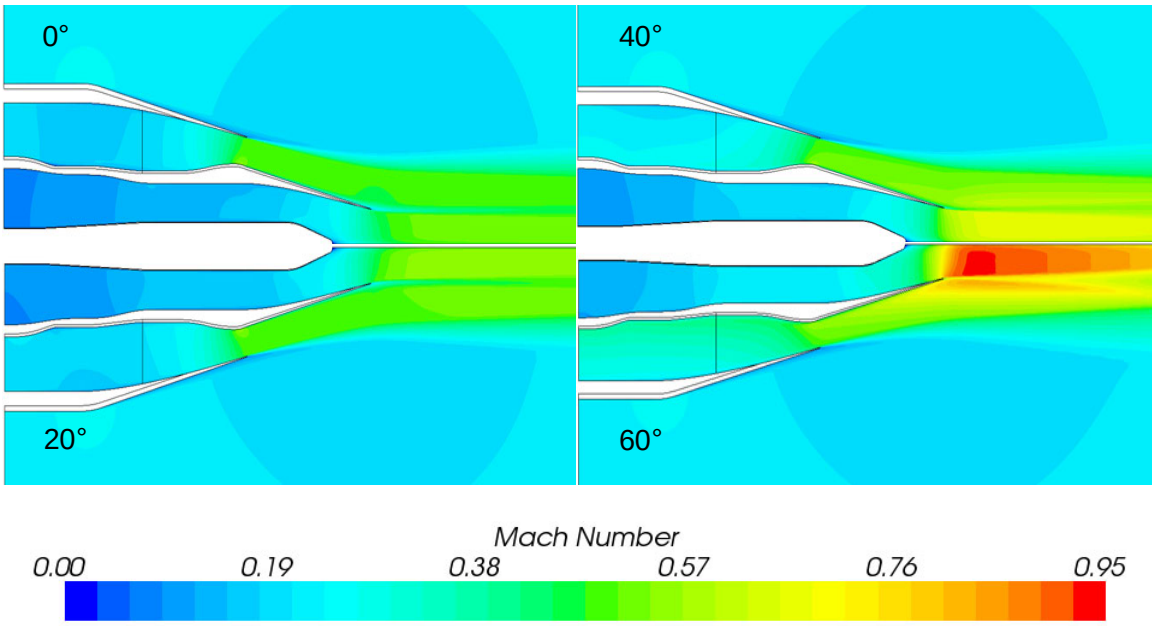

Figure 4–9: Absolute Mach number contours for all fan inlet swirl angles at hot approach conditions in the 4-BB nozzle show no difference to the cold core cases (courtesy of ATA).

4.5 4-BB Nozzle Performance at Take-off

Flow at take-off conditions was used to quantify the penalty in nozzle performance in the presence of un-deflected swirl vanes at an upstream location and the fan nozzle exit. The latter represents the worst case scenario for EAB operation in terms of system net thrust and blockage. Fan stage take-off conditions of temperature and pressure ratios were taken from the NASA SDT study by Hughes [20]. The fan pressure ratio at take-off is 1.49. From the adiabatic efficiency η of 0.88, the fan temperature ratio is calculated to be 1.14 using Equation 4.13,

$$\tau = 1 + \frac{\pi^{\left(\frac{\gamma-1}{\gamma}\right)} - 1}{\eta} \quad . \tag{4.13}$$

Based on a take-off Mach number of 0.25 and ambient conditions of 300 K and 1 atm, the ram pressure and temperature ratios are 1.04 and 1.01 from their respective isentropic relationships. Thus the FNPR is 1.55 and the FNTR is 1.15.

Core stage conditions were assumed using design point analysis and linear scaling of the fan-to-core jet velocity ratio from cruise conditions. A hot CNTR of 2.17 was obtained as before, but the specific procedure for the CNPR is as follows. From the FNPR, the fan nozzle is not choked, but assumed to be fully expanded, in that the pressure at the nozzle exit is atmospheric. With this information and the FNPR, the exit Mach number could be obtained using Equation 4.14. It is found to be 0.82.

$$M_e = \sqrt{\left(\left(\frac{p_t}{p}\right)^{\left(\frac{\gamma-1}{\gamma}\right)} - 1\right)\left(\frac{2}{\gamma-1}\right)} \tag{4.14}$$

Next the fan nozzle exhaust static temperature of 304 K and exit velocity of 286 m/s were calculated using Equation 4.15 and Equation 4.16,

$$T_{fan} = \frac{T_{t,fan}}{1 + \left(\frac{\gamma-1}{2}\right)M_e^2} \tag{4.15}$$

$$V_{e,fan} = M_e \cdot \sqrt{\gamma R T_{fan}} \quad . \tag{4.16}$$

The core exit velocity $V_{e,core}$ of 409 m/s was obtained by assuming the fan-to-core jet velocity ratio scales as 0.7 from design point (cruise) conditions to be consistent with the approach conditions. Since the total temperature of the core was known to be 650.5 K from the CNTR, Equation 4.17 could be used to calculate the static temperature of the core at 567 K,

$$T_{core} = T_{t,core} - \left(\frac{\gamma - 1}{2}\right)\frac{V_{e,core}^2}{\gamma R} \quad . \tag{4.17}$$

The core exit Mach number is then found from Equation 4.18 and finally the CNPR is obtained by re-arranging Equation 4.14 and substituting the core exit Mach number result. The CNPR is calculated to be 1.61.

$$M_{e,core} = \frac{V_{e,core}}{\sqrt{\gamma R T_{core}}} \tag{4.18}$$

The operating conditions at take-off are summarized in Table 4.3.

Table 4.3: Operating conditions for 4-BB nozzle performance study at take-off.

Cases	Freestream PR (Gauge Pressure)	FNPR (Exit Gauge Pressure)	FNTR (Exit Temperature)	CNPR (Exit Gauge Pressure)	CNTR (Exit Temperature)
Hot Core Fan Inlet Swirl Angle: 0 deg	1.04	1.55	1.15	1.61	2.17 (650.5 K)

Figure 4–4 shows the flow path grid with un-deflected vanes at the upstream and fan nozzle exit locations. The chord, solidity, and maximum thickness-to-chord ratio for both vanes at mid-span is 83 mm, 1.51, and 7% respectively. These values were chosen to match the SDT low-count fan OGVs used in the preliminary two-dimensional study.

Computational results suggest the presence of un-deflected vanes at the fan nozzle exit at take-off conditions:

- Reduces system net thrust by 7.45%, and
- Reduces C_d by 5.45% compared to the empty nozzle with no vanes.

For C_d, the ideal mass flow rate in Equation 4.8 is calculated by considering the ideal process of isentropic expansion to ambient conditions at the fan nozzle exit using corrected flow. Since the exit Mach number is known from the exit velocity, it is possible to calculate the corrected flow per unit area,

$$D(M_e) = \frac{\dot{m}\sqrt{R\overline{T}_t}}{A_{flow}\overline{p}_t\sqrt{\gamma}} = \frac{M_e}{\left(1+\frac{\gamma-1}{2}M_e^2\right)^{\frac{1}{2}\left(\frac{\gamma+1}{\gamma-1}\right)}}. \tag{4.19}$$

In addition to the nozzle geometric area, the total temperature and pressures are known at the fan nozzle exit from the operating conditions so accordingly, Equation 4.19 can be re-arranged to extract the desired mass flow quantity $\dot{m}_{ideal}$. The ideal mass flow rate is 0.31 kg/s. The actual mass flow rate can be obtained through integration of streamtubes in Fluent. For the empty nozzle, the actual mass flow rate $\dot{m}_{Fluent}$ is 0.29 kg/s and thus C_d is 0.96.

To check that Fluent correctly integrates streamtubes to estimate the nozzle discharge coefficient through the fan nozzle, a sanity check was performed. The process involved calculating the actual mass flow through the nozzle from corrected flow in Equation 4.19 and comparing this to the result obtained from Fluent. The exit Mach number was calculated from the isentropic relationship in Equation 4.14 since the ratio of mass averaged stagnation pressure to static pressure is known at the nozzle exhaust from Fluent. For the empty nozzle, the pressure ratio is 1.54 giving an exit Mach number of 0.81 and a corrected flow per unit area of 0.56.

The flow through area A_{flow} is computed by subtracting the area occupied by the boundary layer displacement thickness from the nozzle geometric area at the exhaust. For compressible flow, the displacement thickness is given by,

$$\delta^* = \int_0^\infty \left[1 - \frac{\rho(x,y)V(x,y)}{\rho_\infty V_\infty}\right] dy. \tag{4.20}$$

Cell centered values for density and velocity can be obtained from Fluent, so Equation 4.20 may be integrated numerically using the Trapezoidal method to obtain the required displacement thickness. The values for the top and bottom fan nozzle surfaces are 0.14 mm and 0.31 mm respectively. The flow through area for the empty nozzle compared to the geometric area gives a mass flow blockage of 1.26%. The desired mass flow quantity $\dot{m}_{check}$ can be obtained upon re-arranging Equation 4.19 and substituting relevant quantities for estimated flow through area, and total temperature and pressure. For the empty nozzle, it is 0.30 kg/s, compared to Fluent's value of 0.29 kg/s with corresponding C_d values of 0.97 and 0.96, giving an error of 1.49%. A similar analysis was carried out for the other two cases. The summary of nozzle discharge coefficients and sanity checks for all three cases presented in Table 4.4 suggest the mass flow results predicted by Fluent are accurate.

Table 4.4: Summary of nozzle discharge coefficient results for the 4-BB nozzle at take-off conditions.

	No vanes	Vanes at upstream location	Vanes at fan nozzle exit
Term	Value	Value	Value
$\dot{m}_{ideal}$ (kg/s)	0.31	0.31	0.31
$\dot{m}_{Fluent}$ (kg/s)	0.29	0.29	0.28
$\dot{m}_{check}$ (kg/s)	0.30	0.30	0.28
C_D (Fluent)	0.96	0.95	0.90
C_D (Check)	0.97	0.97	0.91
Difference (%)	1.49	1.47	0.67

4.6 Baseline Pylon Configuration 1

The NACA 0012 baseline pylon was used in this study to investigate its effect on the flowfield without swirl. A major challenge was to generate an efficient grid for the full annulus. The objective was to integrate the pylon in a flexible and modular fashion to allow a parametric investigation with swirl vanes and a deflected TE flap in alternate configurations.

The strategy involved creating a 24 degree wedge containing half of the symmetric pylon (e.g. suction surface) integrated in the 4-BB nozzle and flowfield. The entire wedge was then mirrored to create a 48 degree wedge with the full pylon, while checking for and fixing issues involving skewness, interpolation, and alignment of adjacent cells. Periodic surfaces of the wedge were

finally revolved to create the full 360 degree annulus. Care was taken to ensure the grid density of the shear layers forming a conical plume coming off the fan and core nozzle walls was preserved from the original 15 degree wedge 4-BB nozzle flowfield grid provided by ATA. The radial and axial extent of the grid is $5D_{fan}$ and $20D_{fan}$ respectively, consistent with the grid used in the swirling bypass flow study. The total cell count is approximately 10 million. Figure 4–10 shows a close-up view of the pylon in the 48 degree wedge. The most important feature of this grid is its modularity; individual grid units called blocks containing vanes, or an entire deflected pylon TE flap can be added as required for further studies.

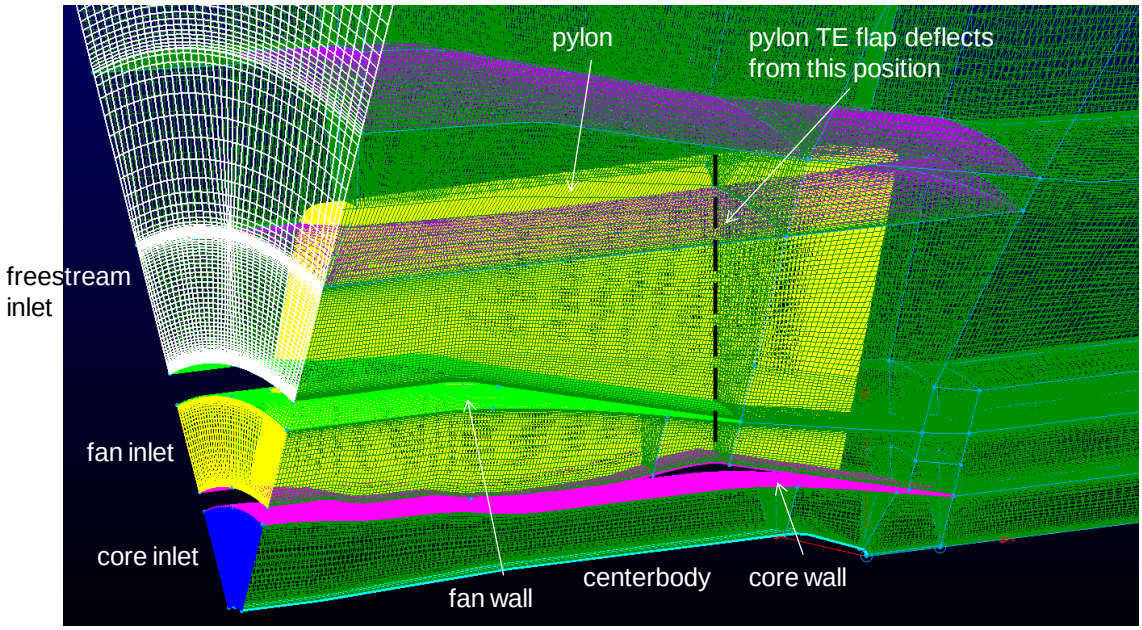

Figure 4–10: Close-up view of the 48 degree wedge grid that contains the baseline pylon geometry; the pylon TE flap deflects from the hinge location shown to form an alternative pylon configuration.

The boundary conditions selected for the swirling bypass flow study were applied to the baseline pylon calculation. Results suggest the non-dimensional thrust coefficient defined by Equation 4.21,

$$C_0 = \frac{F_0}{qA_{ref}}, \tag{4.21}$$

is 3.33 using both CV definitions and the flow blockage due to the pylon in the fan gas path is 4.37% compared to the empty nozzle with no pylon.

Contours of axial Mach number in $r-\theta$ cross section planes in Figure 4–11 show the jet flow downstream of the pylon deflects upwards to form a pear shape due to the interaction with the pylon. Velocity vectors in Figure 4–12 at the $r-\theta$ cross section plane x/L = 0.53 show there is more inward entrainment of air from the freestream in the 4-BB nozzle with the baseline pylon installed compared to the empty 4-BB nozzle. This causes the jet flow to elongate in the direction of the pylon downstream of the EAB.

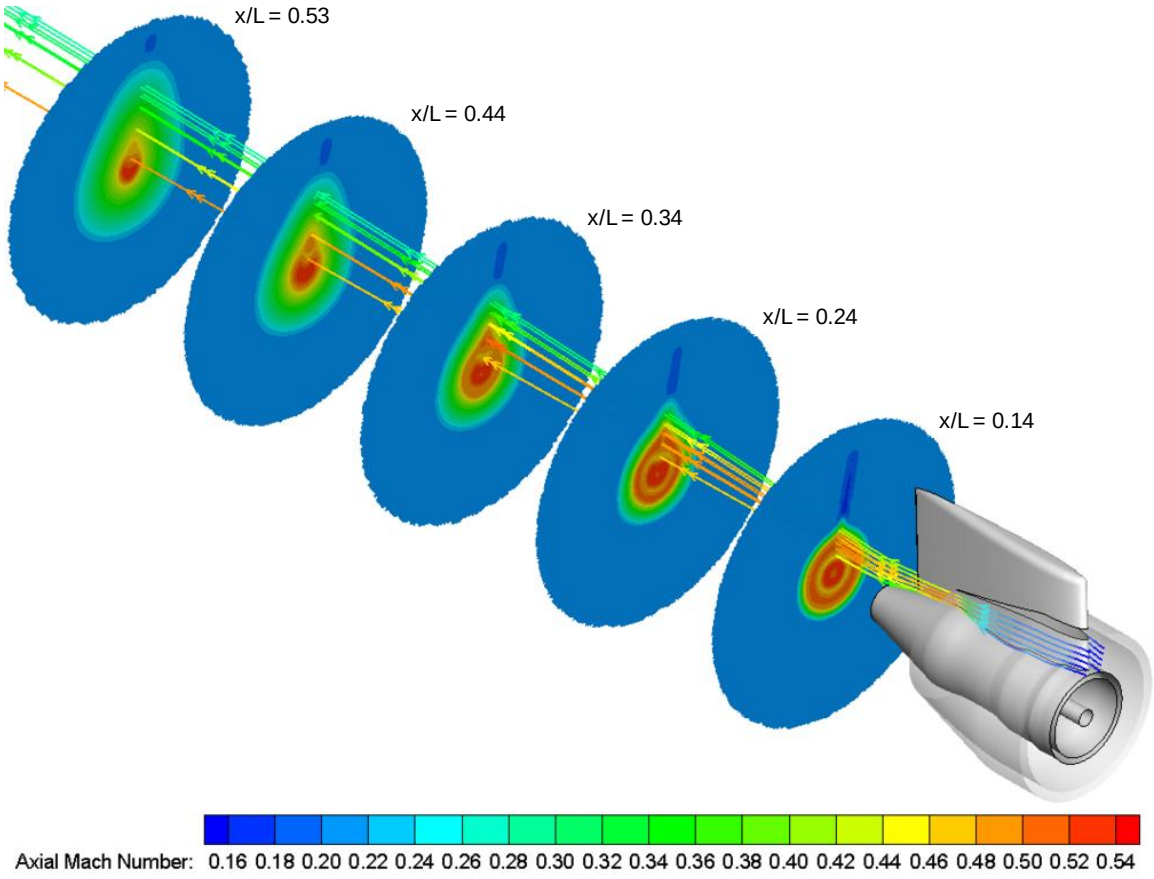

Figure 4–11: Axial Mach number contours in $r-\theta$ cross section planes show the upward motion of the jet flow in the wake of the pylon is due to the interaction with the pylon.

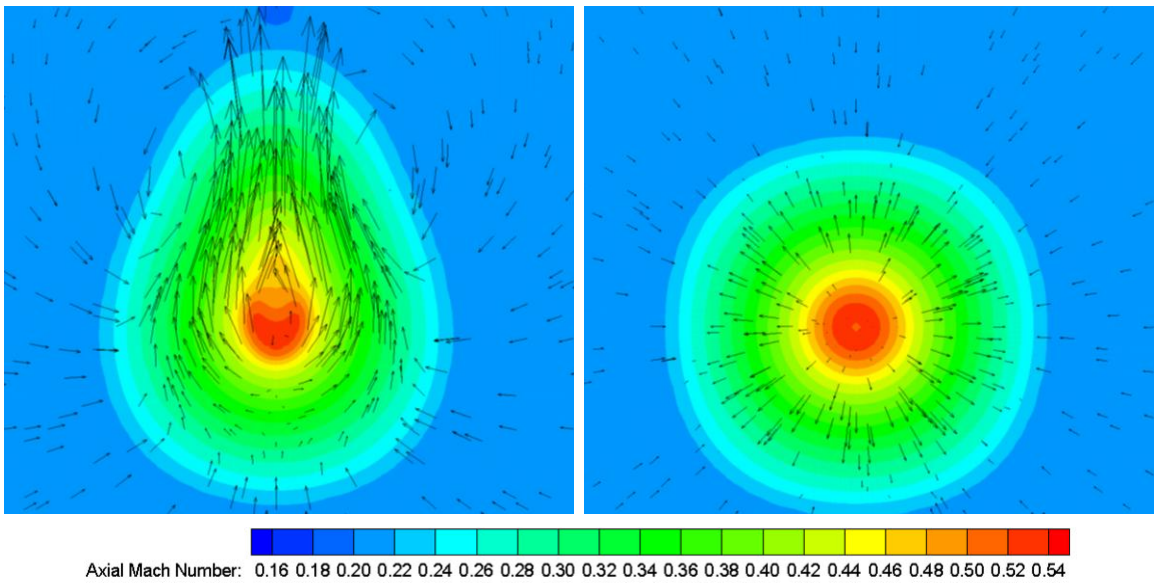

Figure 4–12: Velocity vectors at x/L = 0.53 in the 4-BB nozzle with the baseline pylon installed (left) show there is more entrainment of air from the freestream compared to the empty 4-BB nozzle (right) because of the pylon.

4.7 Baseline Pylon Configuration 2

For consistent performance analysis in the effective drag calculation, Equation 1.3, un-deflected swirl vanes were added at the fan nozzle exit to quantitatively assess the performance penalty in terms of system net thrust and fan mass flow at approach conditions. The chord and solidity of each vane at mid-span is consistent with the study of nozzle performance at take-off, allowing 19 vanes to be modeled in the full annulus. Results suggest the reduction in thrust due to drag from the vanes is 2.42% using both CV definitions and blockage due to the pylon and vanes is 5.46%.

4.8 Alternative Pylon Configuration 1

In the first alternative pylon configuration (AP1), the pylon TE flap is deflected full-span by 35 degrees. The motivation for the aggressive full-span deflection was three-fold. First, it represents the worst case scenario for structural design because of the potentially large side loads on the EAB. Second, it allows for an investigation of the extent of the expected separation around the pylon. Finally, the flowfield results can guide how much and where the pylon TE flap should be deflected, and the placement and distribution of asymmetric swirl vanes.

The specific choice of 35 degrees corresponds to the average swirl angle at the fan nozzle exhaust plane that produces a C_D value near 1.0 in the axisymmetric swirling bypass flow study performed by ATA. The AP1 configuration is shown assembled on the 4-BB nozzle test bed in Figure 4–13, courtesy of ATA.

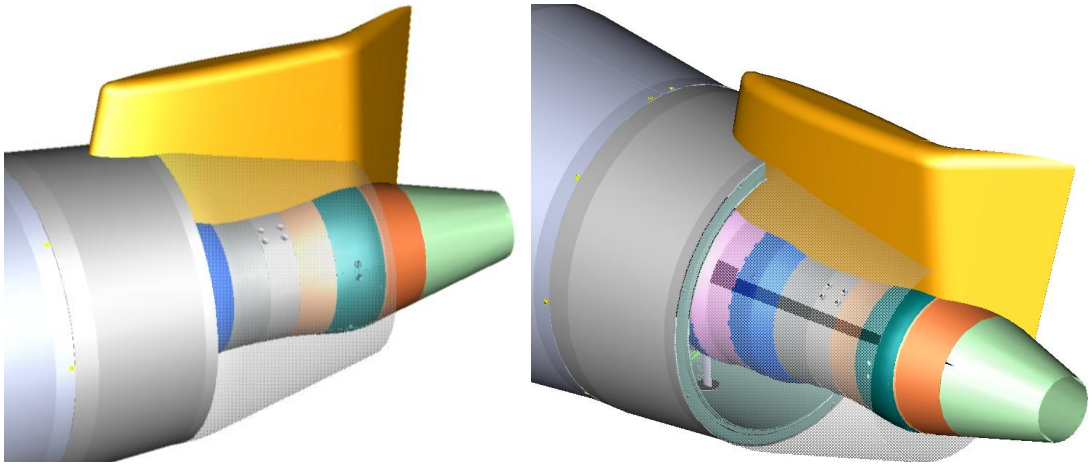

Figure 4–13: The full-span 35 degree TE deflected pylon is shown assembled on the 4-BB nozzle test bed, provided by ATA.

Table 4.5: Equivalent drag coefficient, side load coefficient, and blockage results for AP1.

Metric	Value
C_D	0.25
C_S	0.87
B (%)	5.50

Results for equivalent drag coefficient, side load coefficient, and blockage are presented in Table 4.5. Streamlines colored by absolute Mach number in Figure 4–14 show a tip vortex at the outer span is a result of the aggressive full-span deflection of the pylon TE flap. In addition, flow is redirected off the TE flap on the pressure side without creating the desired coherent swirling outflow downstream of the EAB. As a result, the total side load is more than three times the equivalent drag, indicating the deflection is excessive and should be taken as the load limit case. For all other alternative pylon configurations, the TE flap deflection is reduced to limit the total side load on the EAB. Furthermore, the structural loads used in detailed design of the baseline pylon are taken from the AP1 configuration, after being scaled up from the approach FNPR of 1.2 to a maximum operational FNPR of 1.5 using the ratio of dynamic pressures.

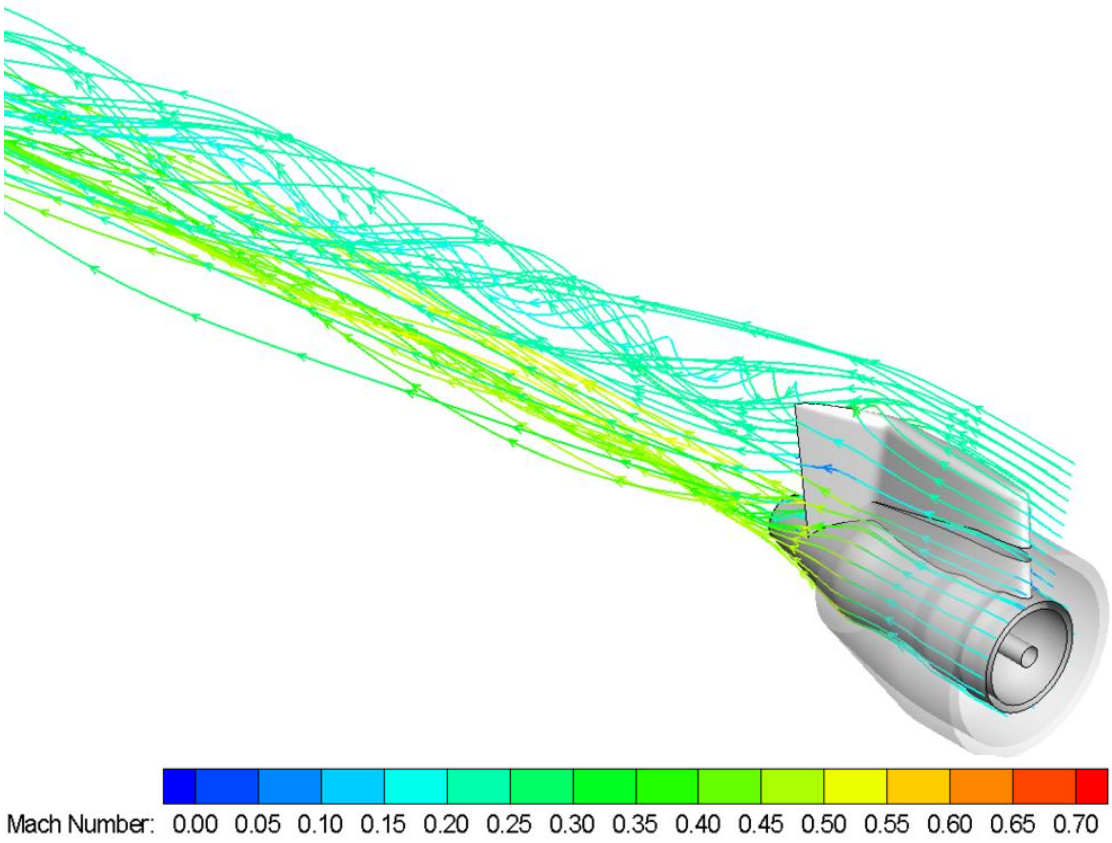

Figure 4–14: Absolute Mach number streamlines for AP1 show flow is re-directed off the pressure side on the pylon and interaction of flow with the outer edge of the deflected flap produces a tip vortex.

Axial Mach number contours in Figure 4–15 show the full-span deflection produces separation on the suction side of the pylon TE flap near the core wall at x/L = 0.10. Circumferential Mach number contours at the same axial location show most of the swirling flow induced by the full-span deflection is concentrated near the pylon TE flap. This confirms the full-span deflection does not produce the desired coherent swirling motion out of the fan nozzle. Furthermore, the swirling flow appears to hug the core nozzle surface near the TE flap, although the extent of this Coanda effect is limited and cannot prevent the flow from separating there. All these observations point to the need for guide vanes to keep the flow attached and generate a coherent swirling outflow. The ideal location to add vanes is at the fan nozzle exit to generate a stronger swirling outflow by avoiding the majority of the duct bifurcation.

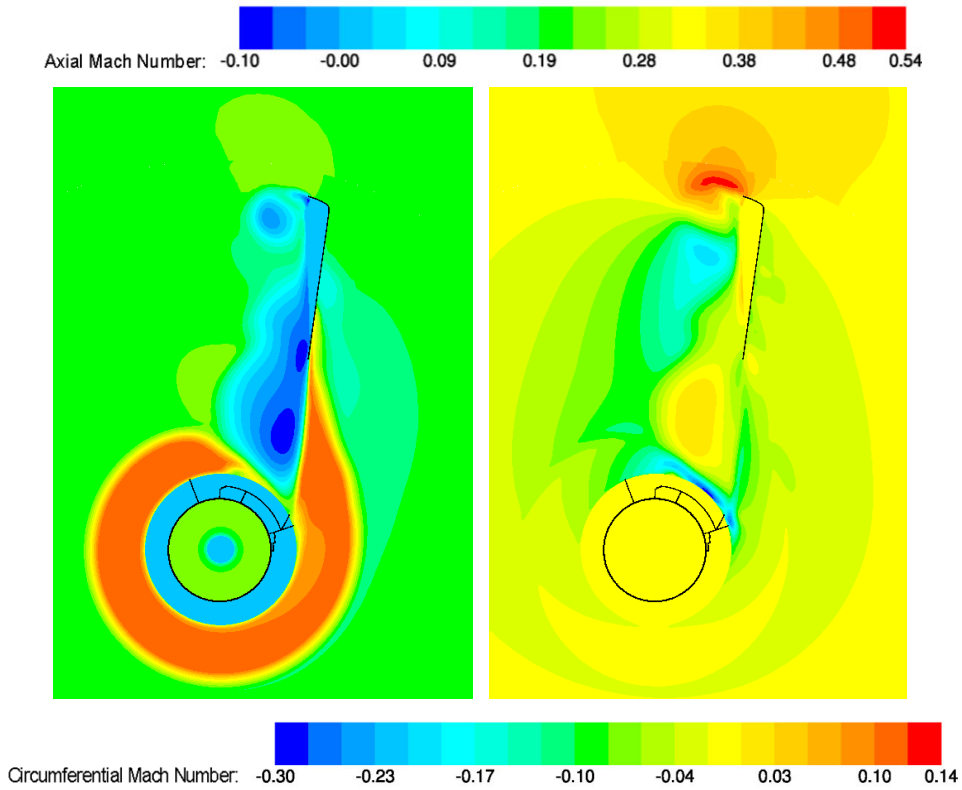

Figure 4–15: Axial (left) and circumferential (right) Mach number contours in the $r-\theta$ cross-section plane at x/L = 0.10 show the flow separates on the suction side of the pylon TE flap near the core wall and the extent of the Coanda effect on the core nozzle surface is minimal.

4.9 Alternative Pylon Configuration 2

For the second alternative pylon configuration (AP2), the pylon TE flap is deflected partial-span by 20 degrees to reduce separation and associated side loads, and vanes are added in order to maintain overall swirling outflow. The deflected portion extends past the fan nozzle lip for flow entrainment into the fan stream and asymmetric turning vanes are placed at the upstream location, as shown in Figure 4–16. The chord and solidity of the vanes at mid-span is the same as the SDT OGVs.

Results for equivalent drag coefficient, side load coefficient, and blockage are presented in Table 4.6. Flow visualization of streamlines in Figure 4–16 shows swirling outflow is maintained from the fan nozzle exhaust, as desired, mitigating side loads. However, a portion of the drag is potentially due to leakage flows in the gap between the deflected flap and the un-deflected pylon TE. This is undesirable because it could adversely affect the far-field noise signature of the EAB.

Table 4.6: Equivalent drag coefficient, side load coefficient, and blockage results for AP2.

Metric	Value
C_D	0.11
C_S	0.23
B (%)	6.58

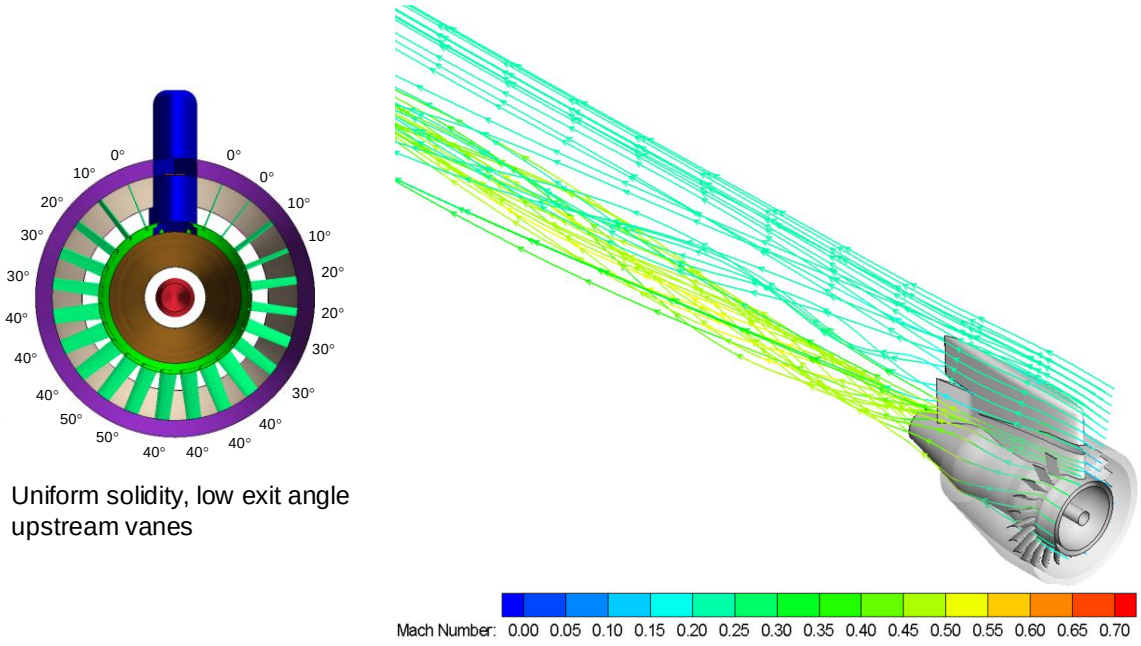

Figure 4–16: Absolute Mach number streamlines for AP2 show swirling flow emanates from fan nozzle exhaust, reducing the side loads on the device. The EAB with vane angle descriptions (left) is provided by ATA.

Chapter 5

Analysis of ATA's Simulations

5.1 Background and Motivation for Analysis

Guided by results of AP1, ATA carried out 10 independent investigations of alternative pylon and vane configurations in addition to those conducted at MIT. A summary of the various configurations with equivalent drag coefficient, side load coefficient, and mass flow results is presented in Table 5.1. The equivalent drag results are obtained using both CV definitions.

Table 5.1: Summary of results for equivalent drag coefficient, side load coefficient, fan mass flow, and blockage for all 10 cases tested by ATA.

Case	Pylon	C_D	C_S	m_{fan} (kg/s)	B (%)	Comments
Test3	Partially deflected 20°, high flap, no fence	0.10	0.14	4.07	7.02	
Test4	Partially deflected 20°, low flap, fence parallel to freestream	0.09	0.07	4.07	6.97	
Test7	Partially deflected 20°, low flap, fence parallel to freestream	0.61	-0.19	3.72	15.08	Potential vortex breakdown?
Test9	Partially deflected 20°, low flap, fence parallel to freestream	0.36	-0.09	3.86	11.71	Potential vortex breakdown?
Test10	Partially deflected 20°, low flap, fence parallel to fan nozzle	0.14	0.10	4.02	8.13	
Test11	Partially deflected 25°, low flap, fence parallel to fan nozzle	0.18	0.18	4.01	8.24	
Test12	Partially deflected 20°, low flap, fence parallel to fan nozzle, through passage	0.17	0.07	4.00	8.52	
Test13	Partially deflected 20°, low flap, fence parallel to fan nozzle	0.35	-0.07	3.88	11.33	Potential vortex breakdown?
Test14	Partially deflected 20°, low flap, no fence	0.35	-0.10	3.88	11.32	Potential vortex breakdown?
Test15	Partially deflected 20°, low flap, no fence	0.14	0.07	4.02	8.20	

Nine cases made use of the 20 degree partial-span pylon TE flap deflection, with varying swirl vane turning angles, solidities, and placement, in order to maximize equivalent drag and minimize side loads on the EAB. Due to the large number of simulations and time constraints, a quick computational turnaround time was desired, and therefore all grid counts were between 3-5 million cells. The EAB configurations with swirl vane angle definitions for all 10 cases in the next several figures have been provided by ATA.

The Test3 configuration was run with vanes of constant solidity in the upstream location as in AP2 but with different exit angles as shown in Figure 5–1. The deflected flap is in the original ("high") location, shown in Figure 5–2, extended beyond the fan nozzle lip to entrain flow into the fan stream. Results suggest a comparable equivalent drag coefficient of 0.10 and blockage of 7.02% is achieved, although the total side loads have been reduced due to stronger swirling outflow. Streamlines in Figure 5–1 reveal interaction of the flow with the TE flap generates a side edge vortex, similar to a flap side edge vortex on an aircraft wing, which could have an adverse impact on noise.

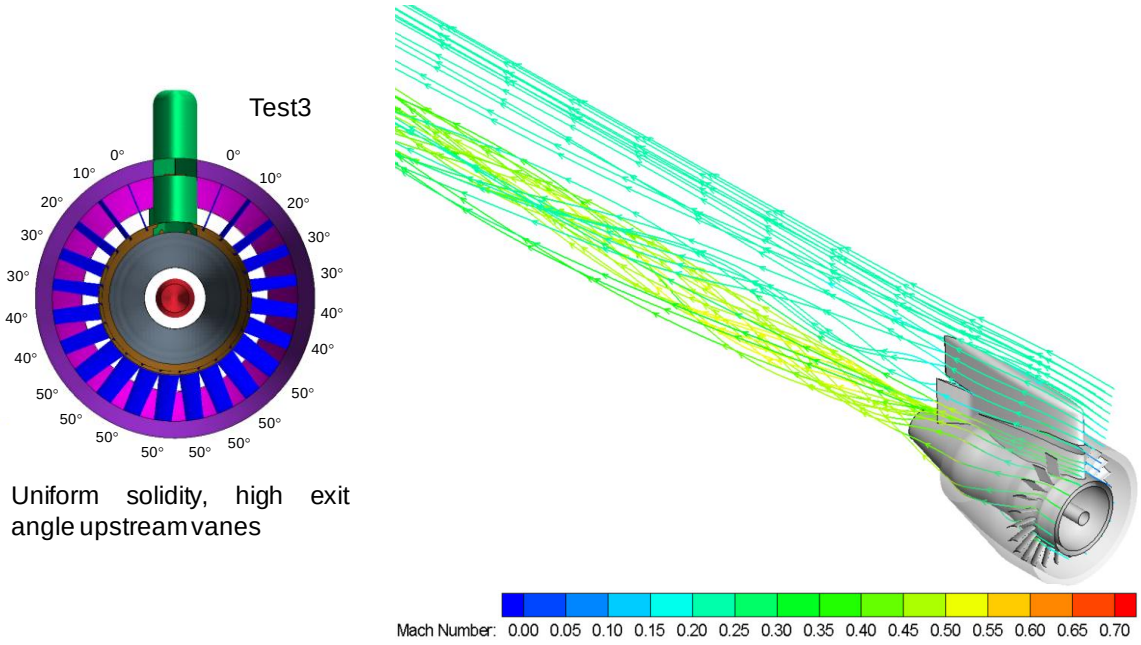

Figure 5–1: Streamlines for Test3 show the flow interaction with the TE flap generates a side edge vortex which could adversely affect noise.

For subsequent cases, the flap was deflected at a lower (“low”) position to reduce side loads and a fence added at the flap edge between the pylon deflection flap and the undeflected TE to reduce non-drag loads from leakage flows and the associated noise. The fence is positioned parallel to the freestream flow direction for test cases 4-9 while cases 10-13 employ a fence parallel to the fan nozzle. The low TE flap deflection position and fence orientations are shown for Test4 and Test10 in Figure 5–2.

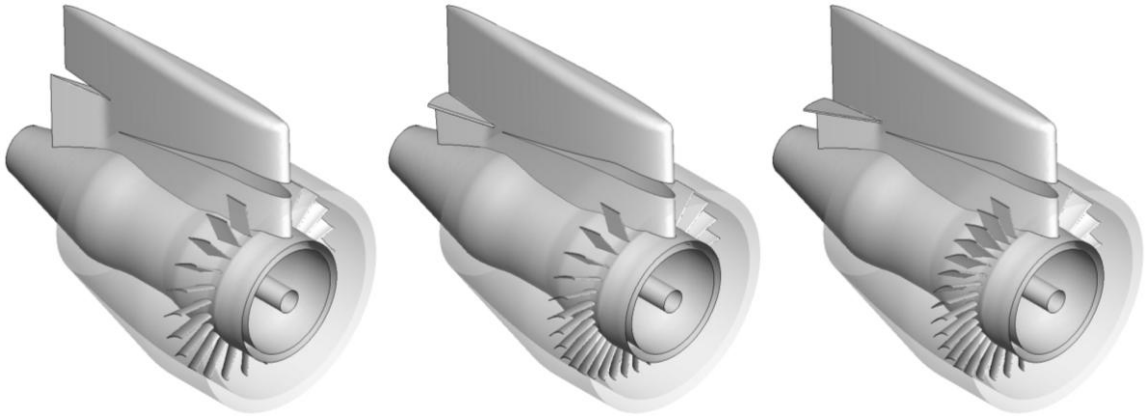

Figure 5–2: Test3 shows the pylon TE flap deflected in the high location, Test4 shows the low flap deflection with the fence parallel to the freestream flow direction, and Test10 shows the low flap with fence parallel to the fan nozzle surface.

Test4 incorporates asymmetric turning vanes with higher solidity in the circumferential region opposite the pylon as shown in Figure 5–3 to generate stronger swirling outflow with reduced side loads on the pylon. Table 5.1 suggests the drag is slightly reduced from Test3 and the side load is significantly reduced as flow interaction with the pylon decreases.

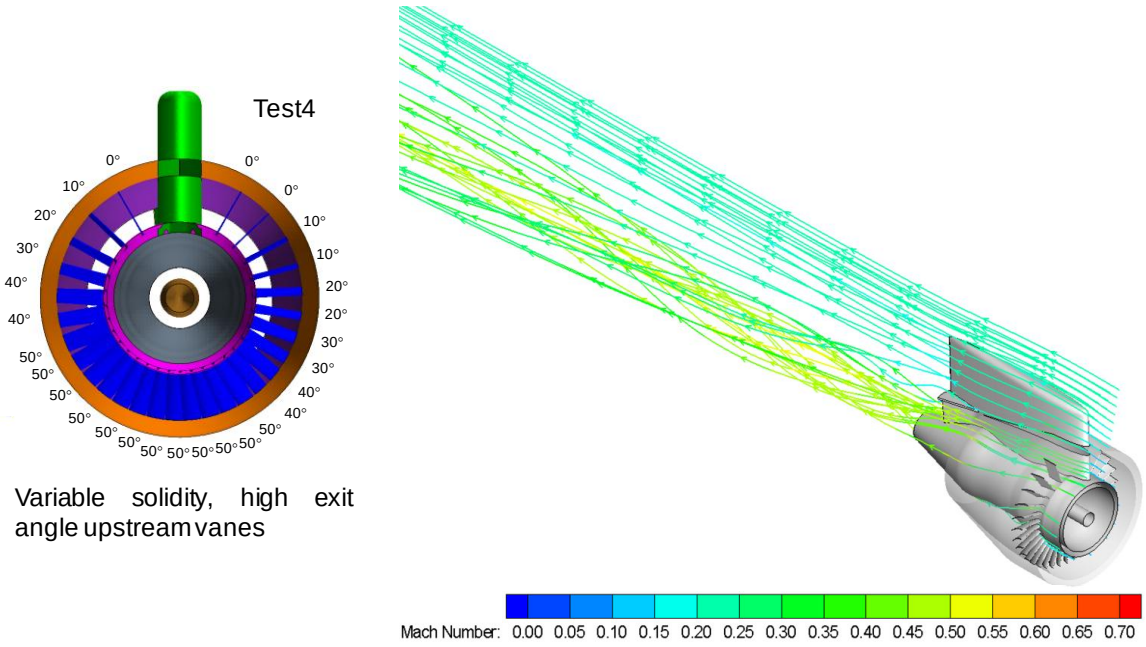

Figure 5–3: Streamlines for Test4 show a stronger swirling flow emanates from the nozzle exhaust compared to Test3.

Test7 and Test9 were run with vanes of constant solidity but different exit angles in the rear ("aft") location. The objective of these computations was to generate a stronger swirling outflow by placing vanes near the nozzle exhaust to minimize interaction of the flow with the duct bifurcation. Test7 used predominantly 30 degree exit vane angles while Test9 employed mainly 20 degree vane exit angles. The lower vane exit angles are derived from quantitative analysis of the axisymmetric swirling bypass flows presented earlier that demonstrate the swirl angle reduces as flow passes through the nozzle exit from conservation of angular momentum. Table 5.1 shows Test7 and Test9 achieve appreciably high equivalent drag coefficients. However streamlines in Figure 5–4 for Test7 and Figure 5–5 for Test9 show the strong swirling motion causes flow to rapidly expand downstream of the fan nozzle exhaust. The question is whether this rapid expansion constitutes vortex breakdown and how the non-axisymmetric flow, from the presence of a pylon and asymmetric swirl vanes, affects it. If vortex breakdown is found to occur, these two configurations may be less desirable because of the increased scattering noise from unsteady flow structures in the breakdown structure close to the solid nozzle surfaces [14]. This flow feature is explored further in Section 5.2. The fan mass flow is significantly reduced due to increased blockage at the nozzle exhaust.

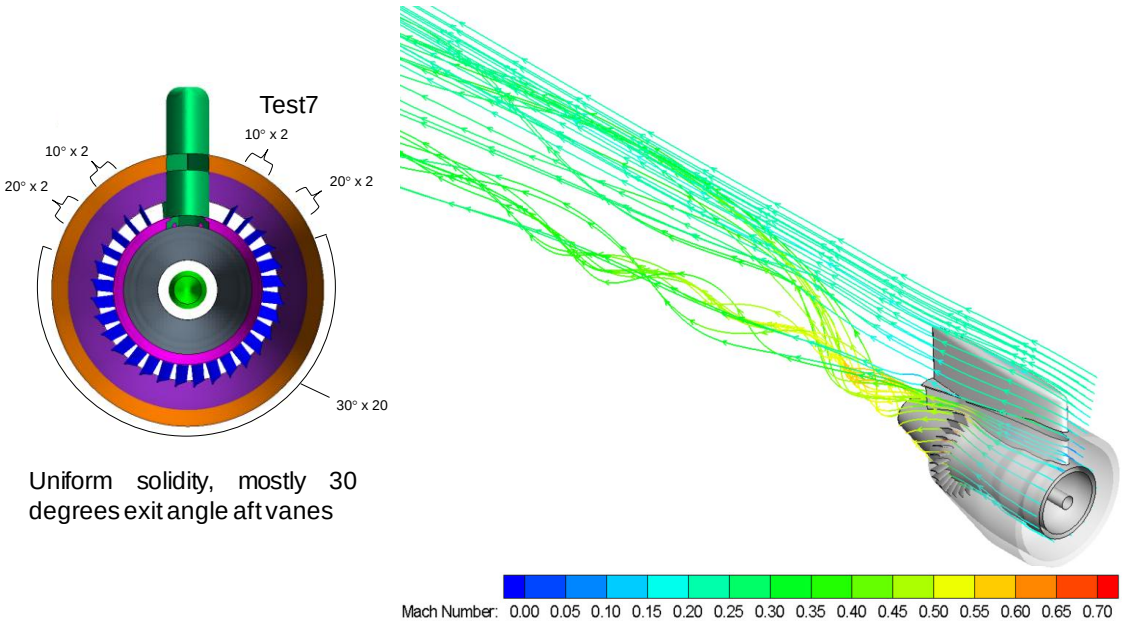

Figure 5–4: Streamlines for Test7 show the flow rapidly expands downstream of the EAB due to the high exit angle turning vanes near the fan nozzle exhaust.

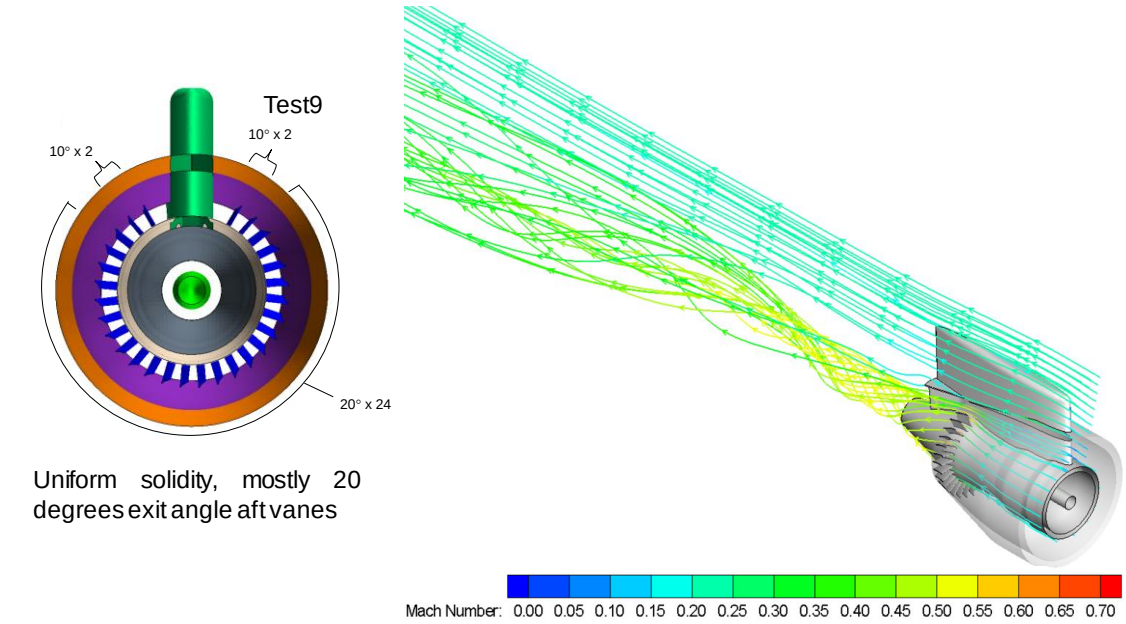

Figure 5–5: Streamlines for Test9 show flow expansion downstream of the EAB is reduced because the vane turning angles are reduced.

The vane configuration of Test10 in Figure 5–6 was similar to Test4 but with higher vane exit angles at the suction side of the pylon and higher solidity around the pressure side of the pylon.

The aim was to further enhance swirling outflow and minimize interaction with the duct bifurcation by providing means for greater turning on the pressure side, away from the pylon. Table 5.1 shows this concept produces more drag and slightly higher side loads than Test4 although the effect on fan mass flow is small. As a result, Test10 is considered the most reasonable forward vane case.

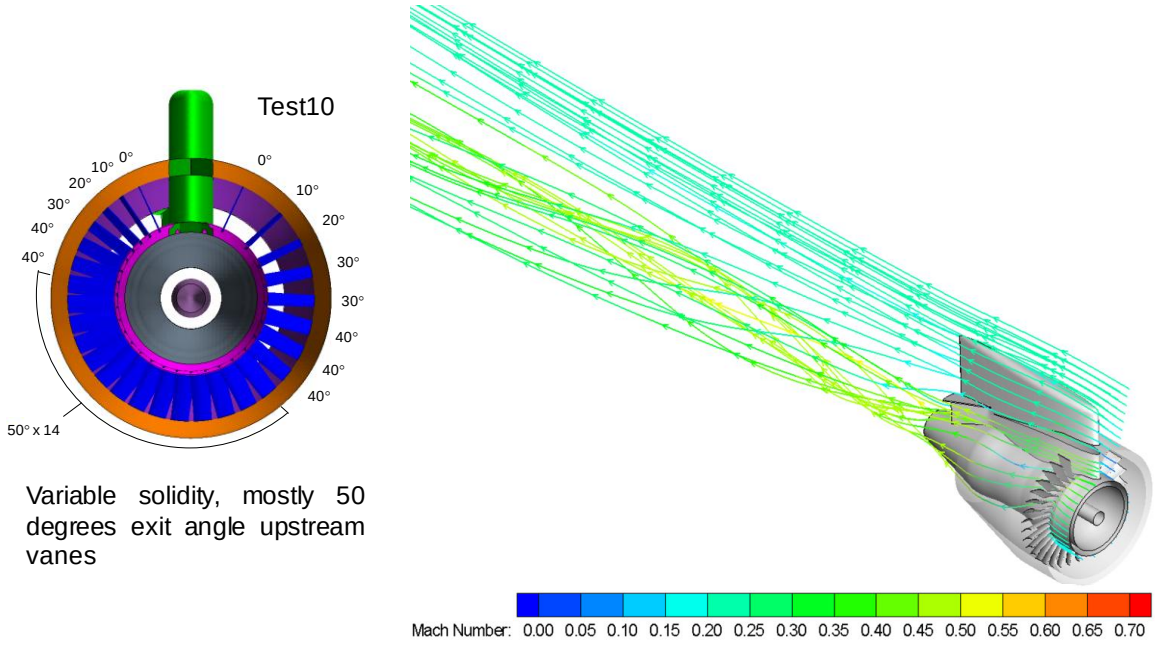

Figure 5–6: Streamlines for Test10 show swirling flow emanates from the nozzle exhaust.

Test cases 11 and 12 employed the same vane configuration as Test10 but with the pylon TE flap deflected by 25 degrees to further enhance flow turning, and a through passage in the pylon to reduce its side load, respectively. Streamlines in Figure 5–7 and Figure 5–8 indicate no major changes to the flowfield. Results suggest the equivalent drag for Test11 is higher than Test10, with comparable side loads. Test12 yields a similar equivalent drag result but with reduced side loads, as expected.

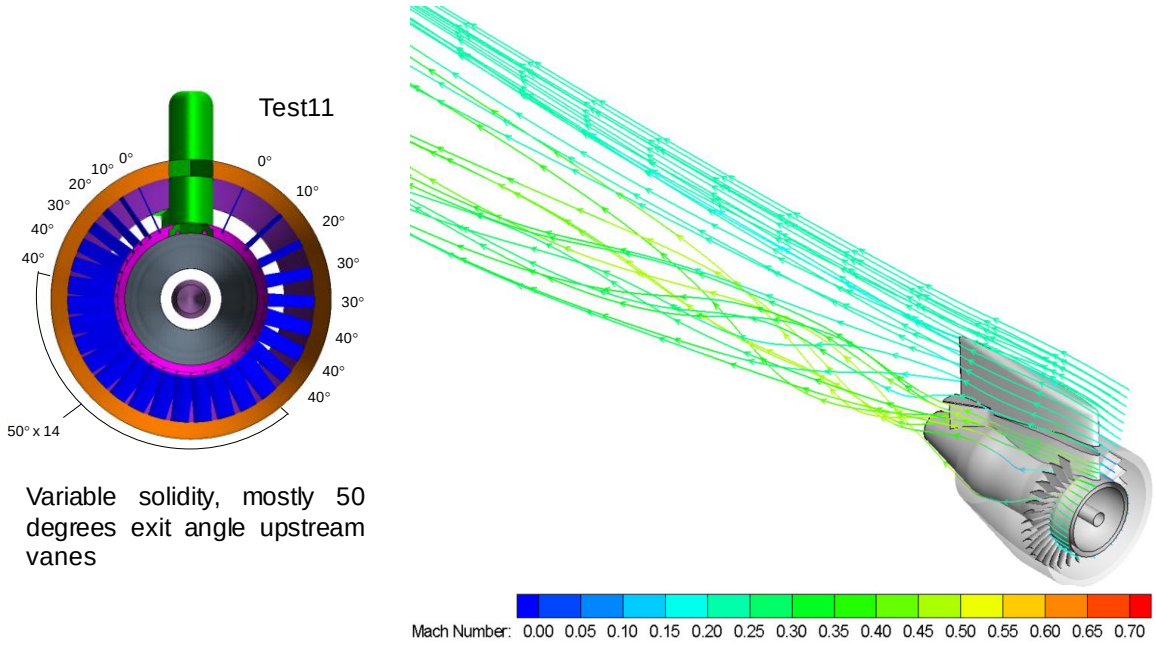

Figure 5–7: Streamlines for Test11 show stronger swirling outflow but the higher level of flow turning from the pylon produces comparable side loads.

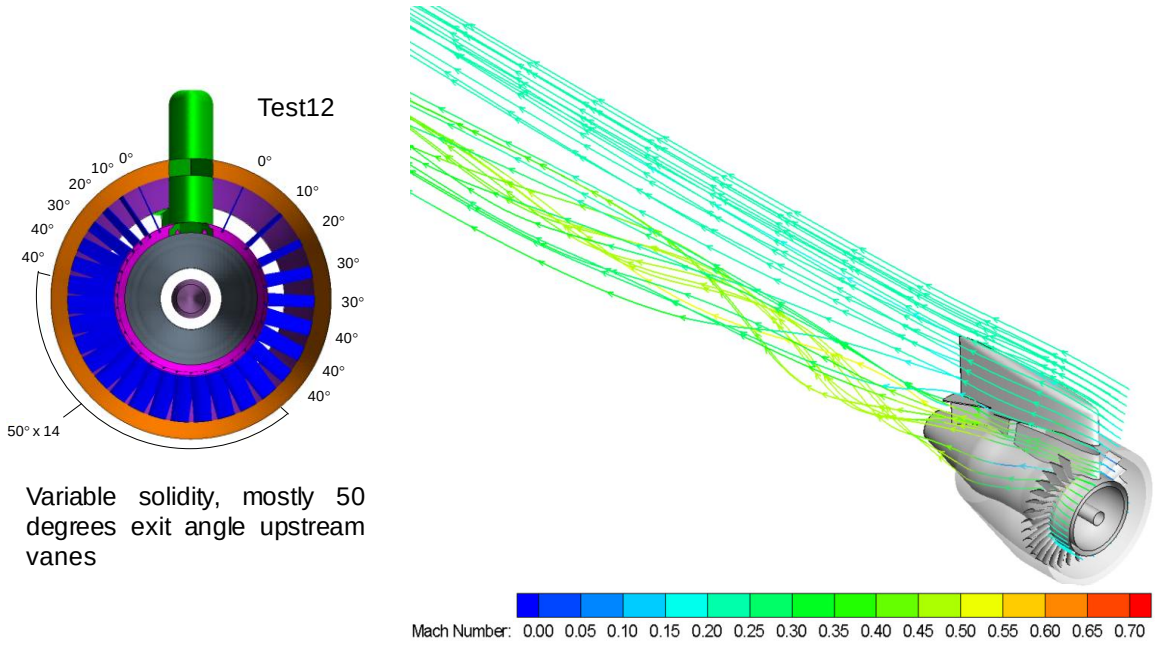

Figure 5–8: Streamlines for Test12 show there is no overall effect on the flowfield due to the through passage.

Test13 used the same vane configuration as Test9 but with the fence parallel to the fan nozzle instead of the freestream as shown in Figure 5–9 to understand of the effect of the fence orientation on the flowfield. Comparing streamlines for these two cases shows the swirling outflow is unaffected by the presence of the different fence. However, results suggest equivalent drag and side loads are slightly reduced from Test9 because of the fence effect. Fan and core mass flows are unchanged as expected. As a result, Test13 is considered the most reasonable aft vane case.

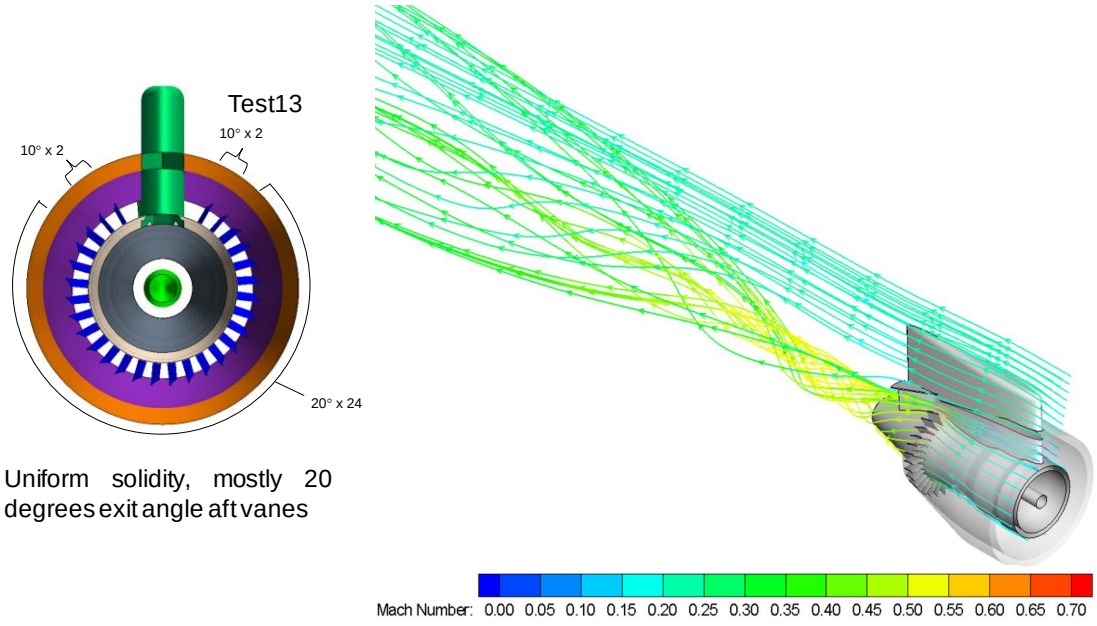

Figure 5–9: Streamlines for Test13 show the fence parallel to the fan nozzle helps to maintain the swirling flow.

To completely isolate the effect of the fence on the flowfield, Test14 and Test15 employed the same vane configuration as the rear visk in Test9 and forward visk in Test10 respectively but without the fence. Flow visualization through streamlines in Figure 5–10 and Figure 5–11 show no evidence for any differences in the flowfield without the fence installation. Results show the drag, side loads, are comparable and mass flows are the same between the respective cases so the fence is thought to have only a localized effect on the flowfield.

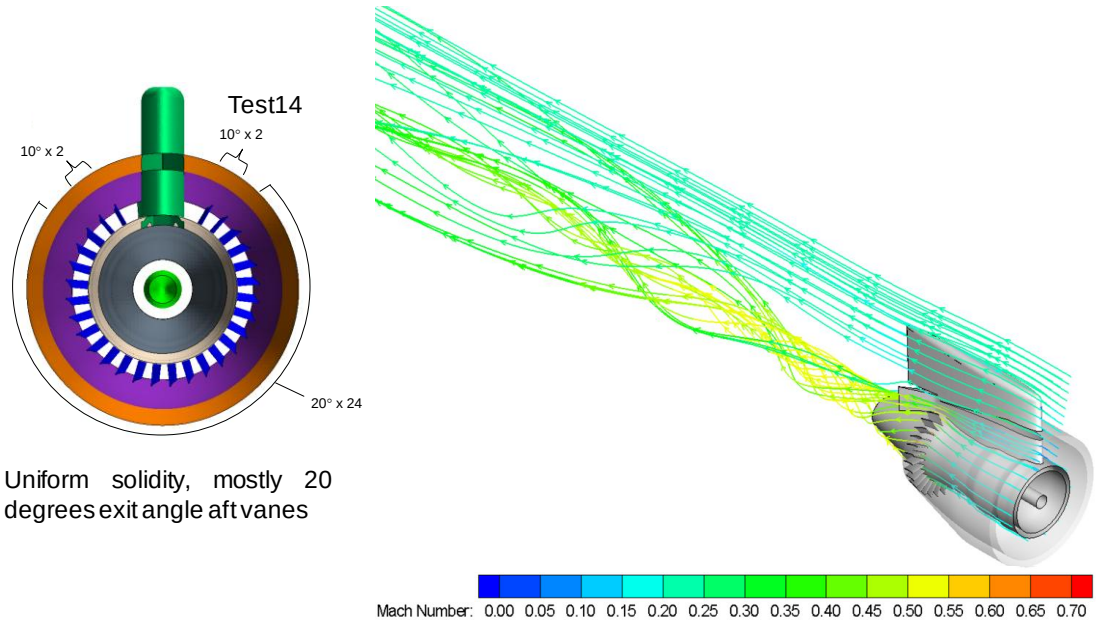

Figure 5–10: Streamlines for Test14 show the rapid expansion of flow is pushed further downstream without the fence compared to Test9.

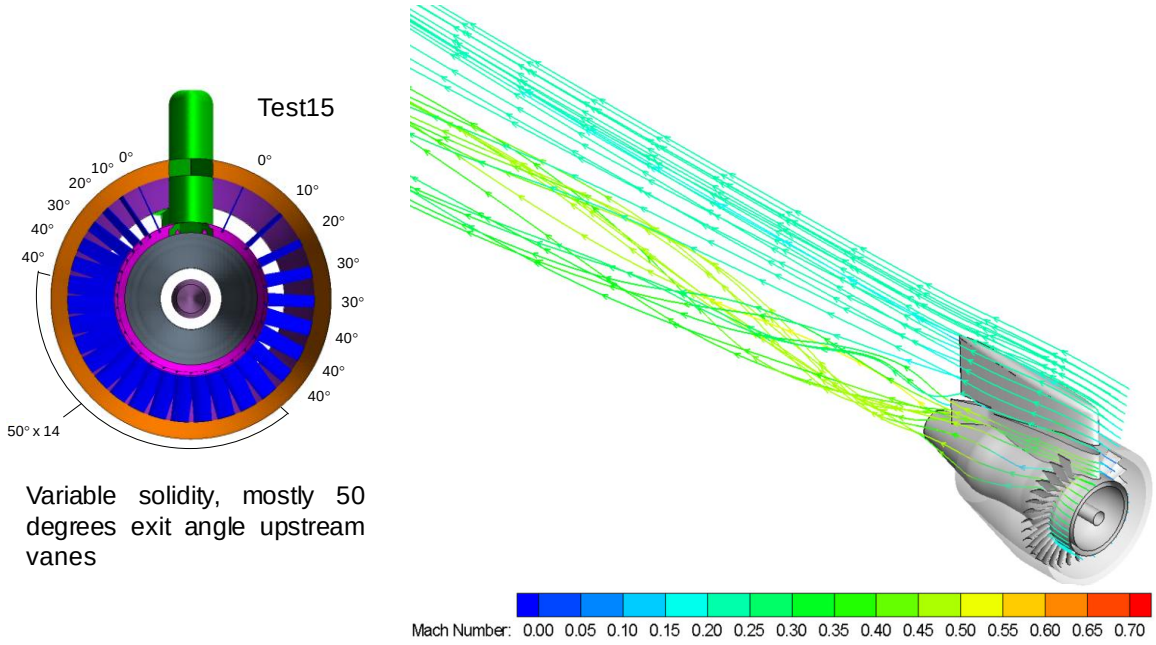

Figure 5–11: Streamlines for Test15 show no overall effect on the swirling outflow without the fence, compared to Test10.

From examining streamlines, each concept maintains coherent swirling flow out of the fan nozzle exhaust as desired. However, there is a clear distinction in equivalent drag values. The aft vane cases generate a stronger swirling outflow with C_D in the range of 0.35-0.61 compared to the upstream vane installation cases which produce C_D between 0.09-0.18. The motivation for this post-processing analysis is thus to learn about the key differences between the different pylon/vane configurations by interrogating the flowfield. Specific research questions to be addressed are:

- What is the effect of the vane configuration on the topology of the flowfield?
- What is the effect of the fence on the flowfield in terms of swirling jet deflection?
- What is the root cause of the side loads acting on the EAB?

5.2 Investigation of the Flowfield Topology

Two representative cases from each of the aft and upstream vane cases were chosen to study the effect of the vane configuration on the topology of the flowfield. The cases selected were Test13, representing the aft vane cases, and Test10, representing the upstream vane cases. The flowfields are also compared to an axisymmetric swirling flow case with 60 degree constant swirl angle specified at the fan inlet boundary. Figure 5–12 shows contours of streamwise vorticity for Test13 in $r-\theta$ cross section planes spaced apart by $2D_{fan}$ downstream of the EAB. Most of the streamwise vorticity is from trailing vorticity off the vanes and vorticity generated in the boundary layers near the nozzle end walls. A positive value indicates the sense of rotation is clockwise and a negative value indicates the sense of rotation is counter-clockwise.

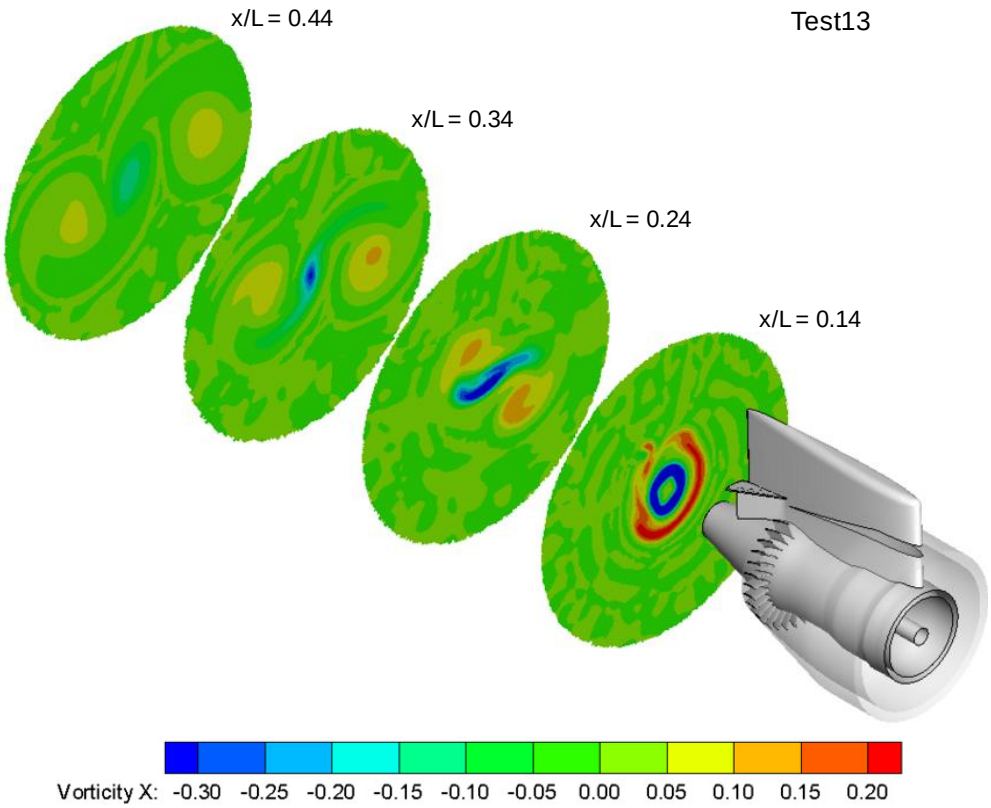

Figure 5–12: Streamwise vorticity contours in $r-\theta$ cross section planes for Test13 show the roll-up and separation of the vortex sheet into three distinct vortices due to the induced velocity field.

The vortex sheet that forms when vortex lines thread through the cross section planes appears to be rolling up downstream of the plane at x/L = 0.14. Further downstream, beyond x/L = 0.24, the vorticity diffuses due to viscous effects and the induced velocity field from swirling motion separates the structure into three distinct vortices at x/L = 0.34. Each structure has its own vortex core and direction of fluid rotation.

Figure 5–13 shows contours of streamwise vorticity for Test10. Similar to Test13, the vortex sheet at x/L = 0.14 rolls up and separates into three structures at x/L = 0.44, but the effect is less pronounced because the trailing vorticity is generated further upstream of the EAB.

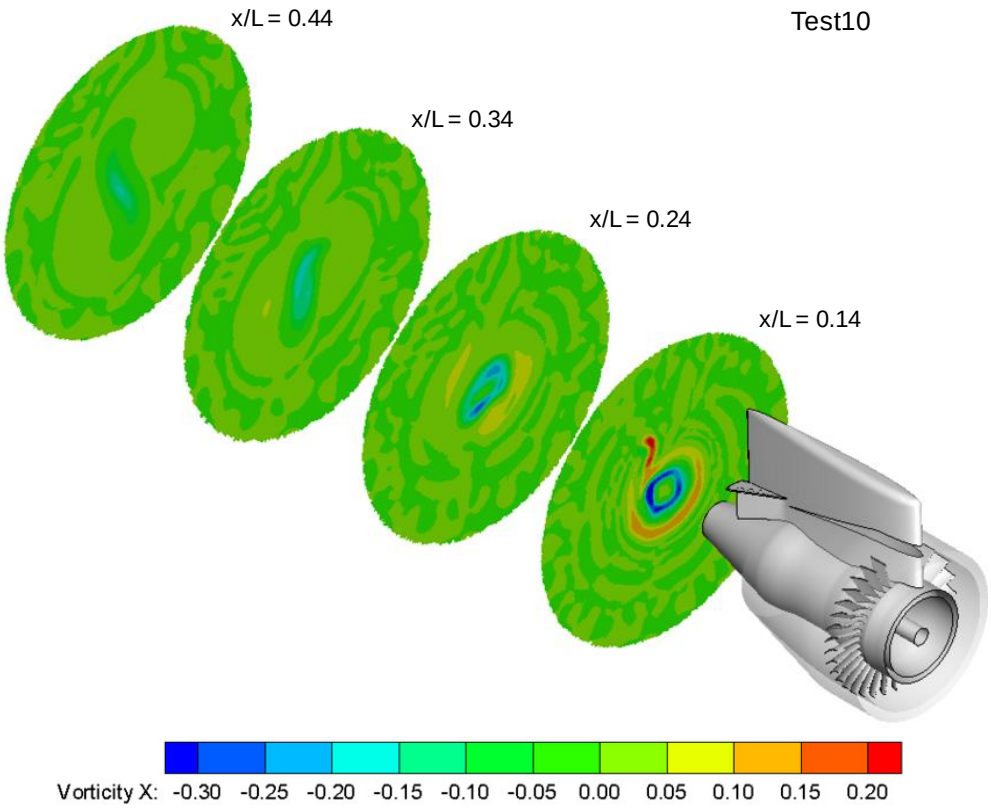

Figure 5–13: Streamwise vorticity contours in $r-\theta$ cross section planes for Test10 show the roll-up and separation of the vortex sheet is less pronounced than in Test13 because the trailing vorticity is from further upstream.

Figure 5–14 shows contours of streamwise vorticity for an axisymmetric swirling flow case with a constant 60 degree swirl angle specified at the fan inlet boundary. All of the vorticity is generated in the boundary layers of the fan and core nozzle end walls. The vortex lines get aligned in the streamwise direction by the bulk fluid motion downstream of the nozzle and their strength decreases due to viscous diffusion effects. The major distinction in the flowfield from Test13 and Test10 is the vortex sheet separates axisymmetrically because the induced velocity field is axisymmetric in the absence of the pylon duct bifurcation.

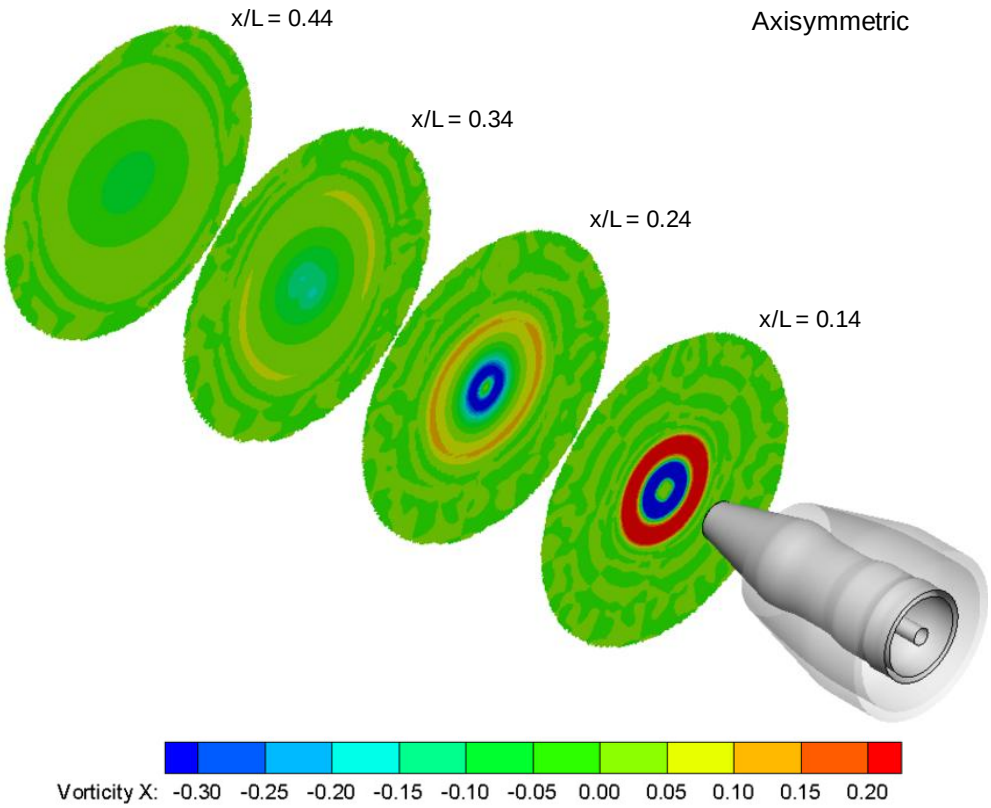

Figure 5–14: Streamwise vorticity contours in $r-\theta$ cross section planes for the axisymmetric case with 60 degree swirl angle specified at the fan inlet show the roll-up and separation of the vortex sheet is axisymmetric.

Figure 5–15 shows contours of axial Mach number in horizontal cross section planes through the EAB for all three cases. The central region of low axial velocity resembling a bubble-type structure in Test13 is a result of the swirling flow rapidly expanding downstream of the nozzle exhaust. The deflection of fan and core flows visible immediately downstream of the nozzle can be attributed to the interaction of the swirling outflow with the high velocity core jet. This creates an asymmetric pressure distribution on the fan and core nozzles that contribute to the side loads on the EAB. More details on the analysis of side loads for all cases are presented in Section 5.4.

In general, vortex breakdown in an axisymmetric swirling flow occurs as a result of excessive swirl and manifests as an abrupt change in flow properties, such as the rapid diffusion of vorticity [2], [27]. Based on these observations then, there is inconclusive evidence to suggest that the roll-up and consequent separation of the vortex sheet in the non-axisymmetric case Test13, and by extension the aft set of vanes, constitutes the vortex breakdown instability. This issue will be clarified by far-field noise measurements of both cases in the NASA AAPL facility.

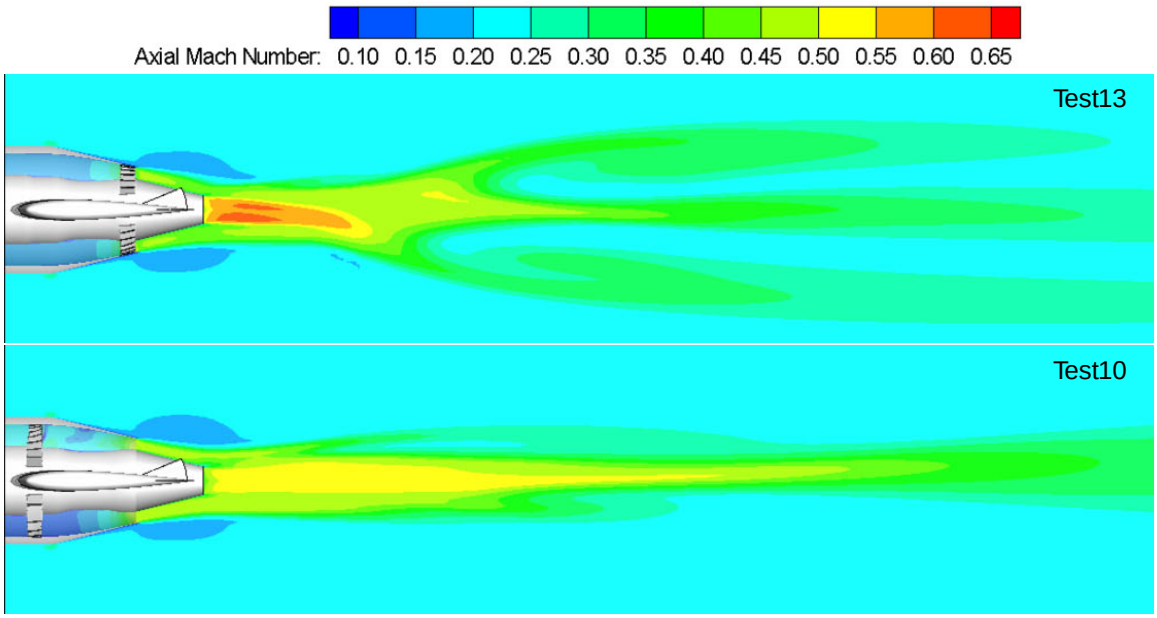

Figure 5–15: Axial Mach number contours in the horizontal plane show the central region of low velocity in the jet flow of Test13 arises due to the strong swirling outflow from the nozzle exit.

The circulation-based swirl parameter *S* can be used to quantify the strength of the asymmetric swirling motion with a high velocity core flow component downstream of the nozzle exit in terms of vorticity. The approach is to compute *S* for Test13, Test10, and the axisymmetric case, compare the values, and relate differences to the geometry. The key challenges are to establish a circular region of radius r_c for calculating Γ_c and to define a representative value for the characteristic convection velocity of the swirling motion V_x. The strategy employed is as follows:

a. Identify the axial location in the flowfield where the vortex sheet completely separates into three distinct structures – the swirl parameter will be calculated at this location.
b. Isolate the area *A* of high positive (clockwise sense) streamwise vorticity in the jet at this location – this is the region of swirling motion that is strongly affected by viscosity, the so-called "viscous core" [27].
c. Calculate the circulation Γ_c through *A* using Equation 4.10.
d. Calculate the effective radius of the viscous core r_c by equating its area to an effective circular area, i.e. $A = \pi r_c^2$.
e. Calculate the mass-averaged axial velocity in the viscous core to determine V_x.

f. Obtain *S* from Equation 4.9 for Test13, Test10, and the axisymmetric case, compare values and relate to the geometry.

The viscous core region in step b) is isolated by plotting the variation of circulation Γ with effective circle radius r to establish the point r_c where the circulation begins to approach a constant value Γ_c, as shown in Figure 5–16. The swirl parameter for Test13 and Test10 is calculated at axial locations associated with vortex sheet separation. Contours of streamwise vorticity for Test13 in Figure 5–12, Test10 in Figure 5–13, and the axisymmetric case in Figure 5–14 suggests the vortex sheet separates at x/L = 0.34, x/L = 0.44, and x/L = 0.34 respectively. The axial location at x/L = 0.44 was chosen for analysis on all three cases to maintain consistency. Results are presented below.

Table 5.2: Swirl parameter results at x/L = 0.44 for Test13, Test10, and the axisymmetric case.

Case	Γ/Γ_{Test13}	r/r_{Test13}	M_x	S
Test13	1.00	1.00	0.24	1.25
Test10	0.53	1.12	0.23	0.62
Axisymmetric	0.98	1.12	0.22	1.22

Results in Table 5.2 show the effect of the aft vane cases is to generate more positive circulation in the separated vortex sheet from stronger swirling outflow compared to the upstream vanes. The circulation for Test13 is of similar strength to the axisymmetric case suggesting the effect of asymmetry from the pylon is less prominent when vanes are placed near the nozzle exhaust.

The procedure from b) to f) is repeated at several downstream axial stations to obtain a trend. The variation of swirl parameter with axial location in Figure 5–17 shows it is at a higher level in the flowfield for Test13 and the aft vane concepts than Test10 and the upstream vane concepts. This is because the trailing vorticity off the vanes is generated near the nozzle exhaust in the aft vane configurations and is therefore stronger. The larger swirl parameter values upstream of x/L = 0.42 for the axisymmetric case compared with Test13 is a result of stronger swirling outflow. The average swirl angle at the fan nozzle exhaust is 37 degrees for a constant fan inlet swirl angle of 60 degrees. This is greater than the predominantly 20 degree swirl angle vanes placed at the fan nozzle exit in Test13. The reduction in swirl parameter between the nozzle exhaust (x/L = 0.11) and the domain outlet is: $\Delta S = 1.49$ for Test13, $\Delta S = 0.95$ for Test10, and $\Delta S = 4.43$ for the axisymmetric case. The difference is likely because the streamwise vorticity diffuses more

rapidly in the axisymmetric case compared to the asymmetric cases, possibly indicating Test13 and the other aft vane cases may not produce vortex breakdown.

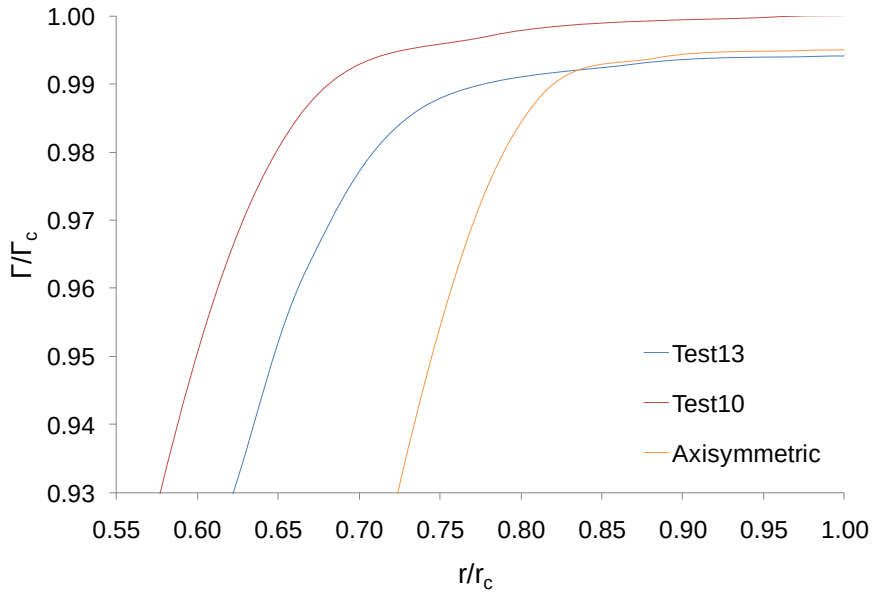

Figure 5–16: Variation of circulation with radius at x/L = 0.44 for Test13, Test10, and the axisymmetric case shows it approaches a constant value at the viscous core radius.

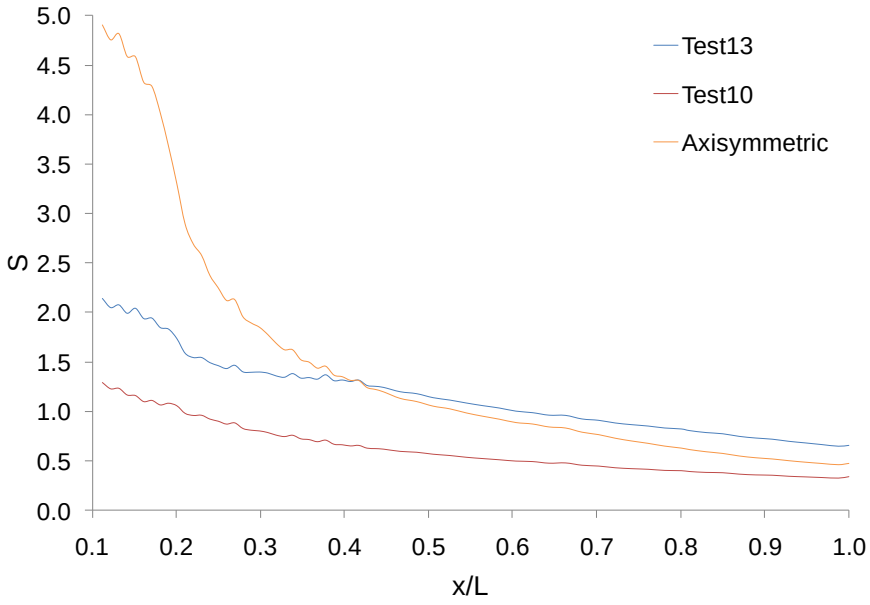

Figure 5–17: Variation of the swirl parameter with axial location shows Test13 is consistently higher than Test10 in the entire flowfield and the axisymmetric case after x/L = 0.42.

5.3 Fence Effect on the Flowfield

To determine the effect of the fence on the flowfield in terms of swirling flow deflection, the three aft and three upstream vane cases presented in Figure 5–18 were analyzed. Both sets of cases include configurations with the fence parallel to the freestream direction (Test9 and Test4), parallel to the fan nozzle surface (Test13 and Test10), and no fence (Test14 and Test15).

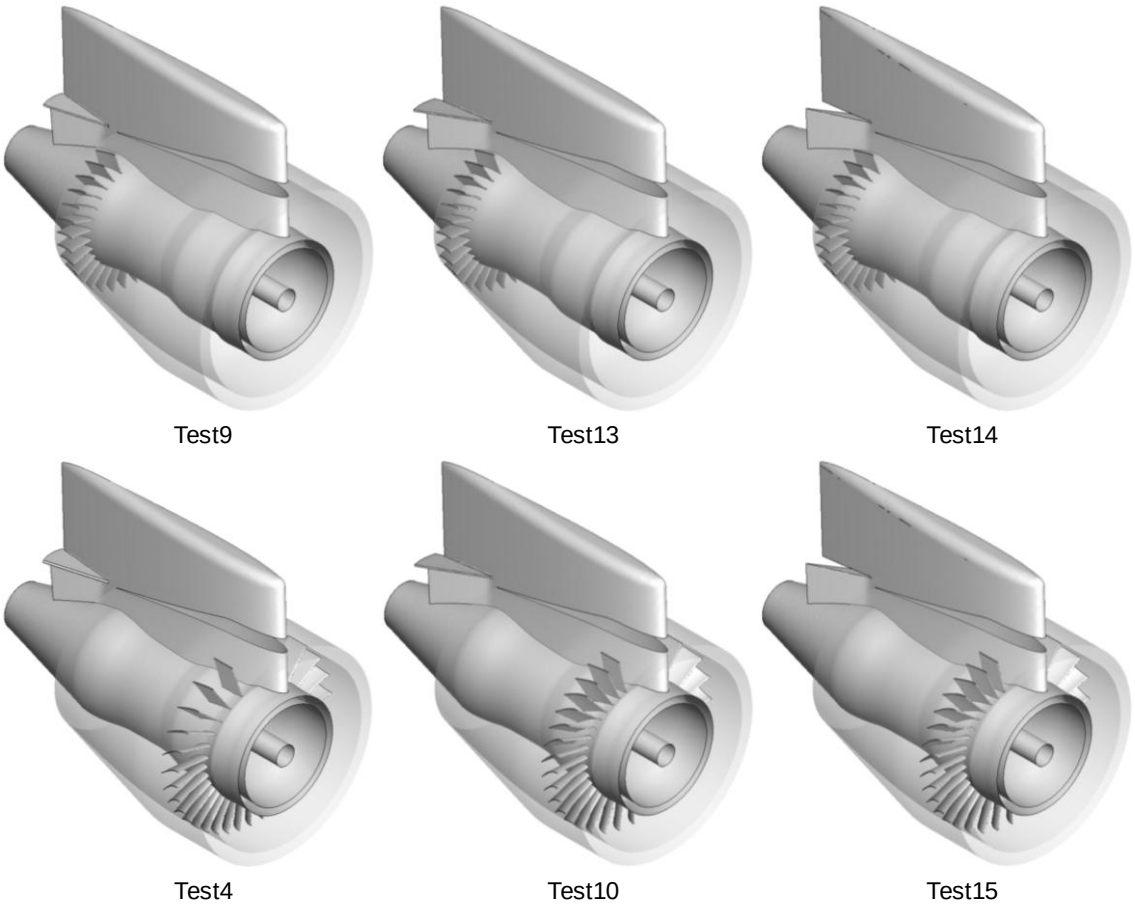

Figure 5–18: The three aft and three upstream cases are analyzed to determine the effect of the fence on the flowfield.

Axial Mach number contours in $r-\theta$ cross section planes show the evolution of the flowfield for the aft set of vanes. Comparing the jet evolution for the aft vane configurations in the next three figures, it is apparent that the fence has no overall effect on the flowfield.

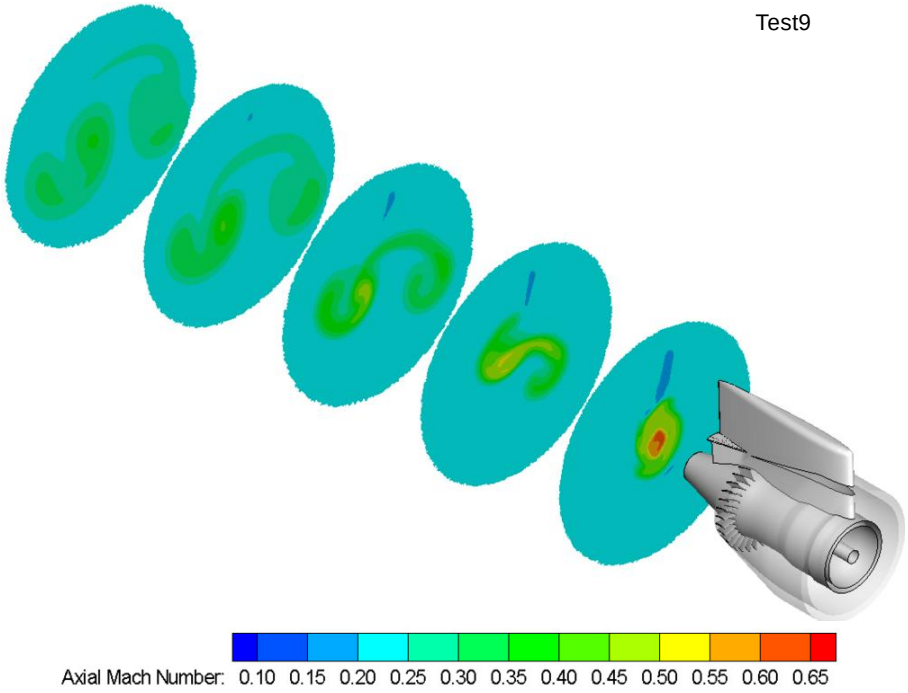

Figure 5–19: Axial Mach number contours in $r-\theta$ cross section planes for Test9 show the flowfield with the fence parallel to the freestream downstream of the EAB.

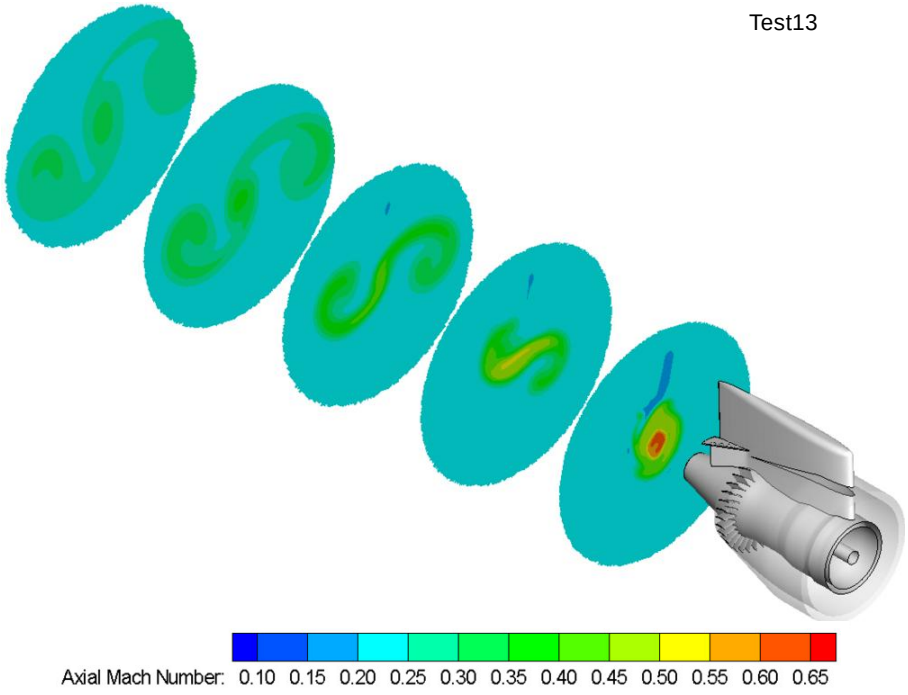

Figure 5–20: Axial Mach number contours in $r-\theta$ cross section planes for Test13 show the flowfield is unaffected by the fence parallel to the fan nozzle.

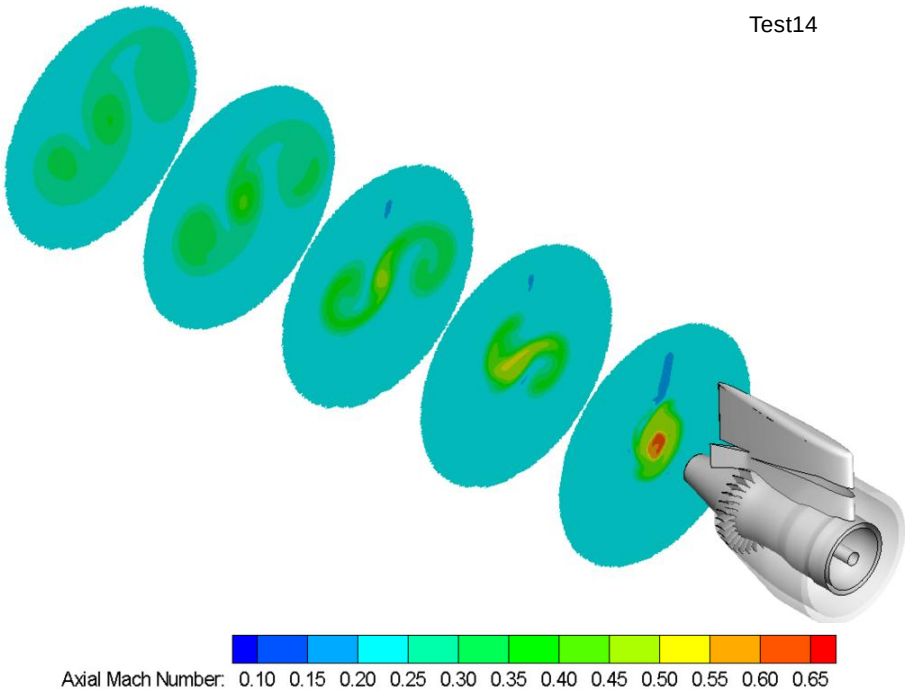

Figure 5–21: Axial Mach number contours in $r-\theta$ cross section planes for Test14 show the flowfield is unaffected by the absence of the fence.

Comparing the jet evolution for the forward vane cases in the next three figures, the fence has no effect on the jet deflection in the flowfield. The greater jet expansion in Test10 and Test15 compared to Test4 in Figure 5–22 downstream of the nozzle from the second axial station is a result of higher vane turning angles on the pylon suction side and higher solidity on the pylon pressure side (in view). This vane arrangement creates a stronger swirling outflow that gradually expands downstream of the fan nozzle as the jet slows down due to the conservation of angular momentum.

Absolute Mach number streamlines, shown in Figure 5–25, are used to assess the effect of the fence on jet deflection locally near the fence. Comparing the two sets of vane concepts, it appears the interaction of flow with the fence is influenced by turning from the vanes. Examination of the aft vane cases suggests the fence parallel to the fan nozzle in Test13 helps to maintain the swirling outflow. Examination of the upstream concepts shows the fence parallel to the freestream in Test4 and the absence of the fence in Test15 produces a side edge vortex that is similar to a delta wing at an angle of attack. This could lead to an undesirable noise source. For this reason, it was decided to employ the fence parallel with the fan nozzle for all alternative pylon model scale tests in the NASA AAPL facility.

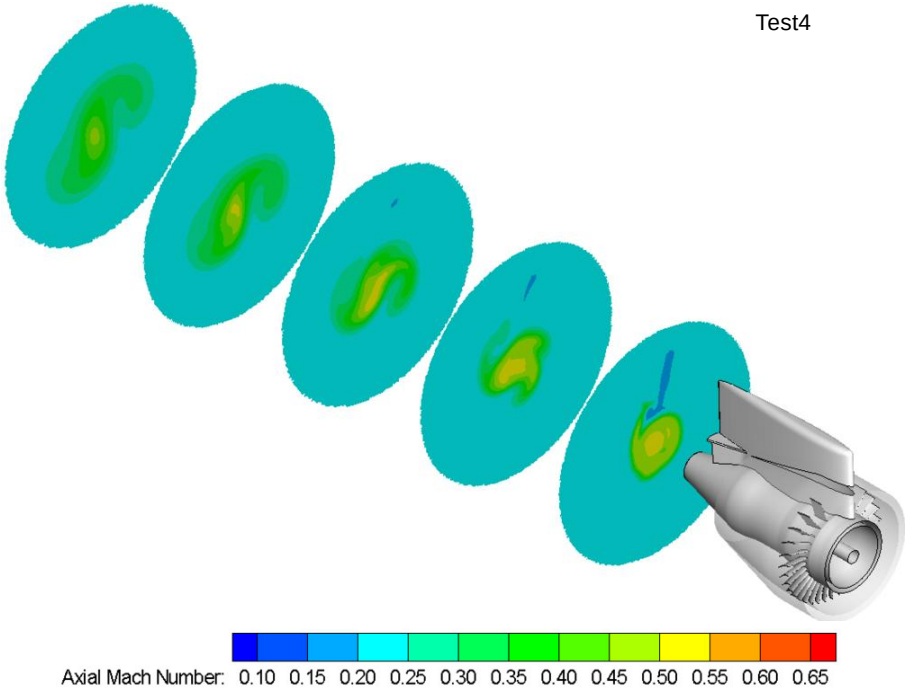

Figure 5–22: Axial Mach number contours in $r-\theta$ cross section planes for Test4 show the flowfield with the fence parallel to the freestream downstream of the EAB.

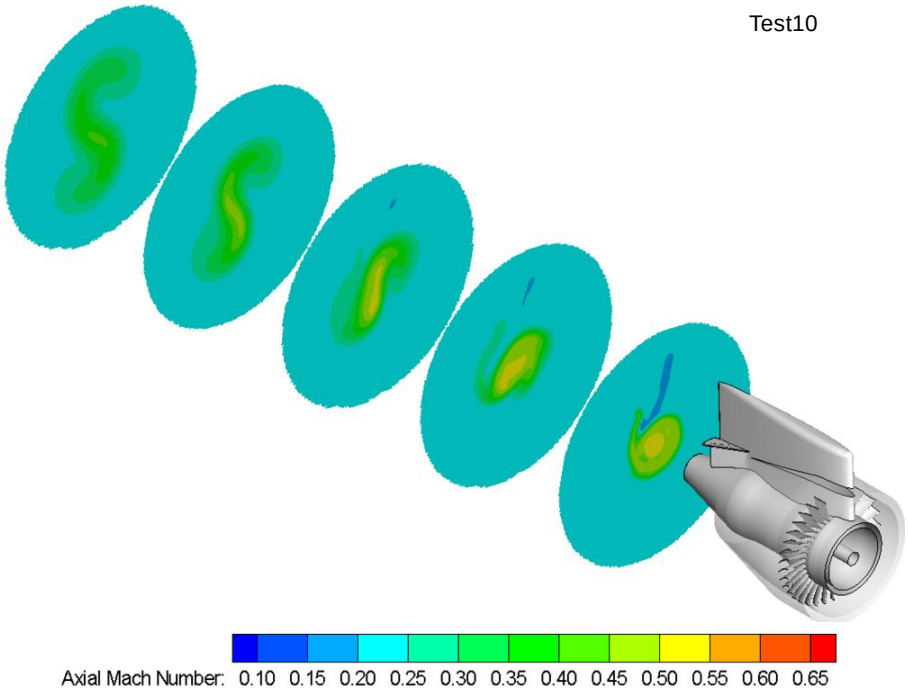

Figure 5–23: Axial Mach number contours in $r-\theta$ cross section planes for Test10 show the jet expands more rapidly than Test4 due to higher flow turning upstream.

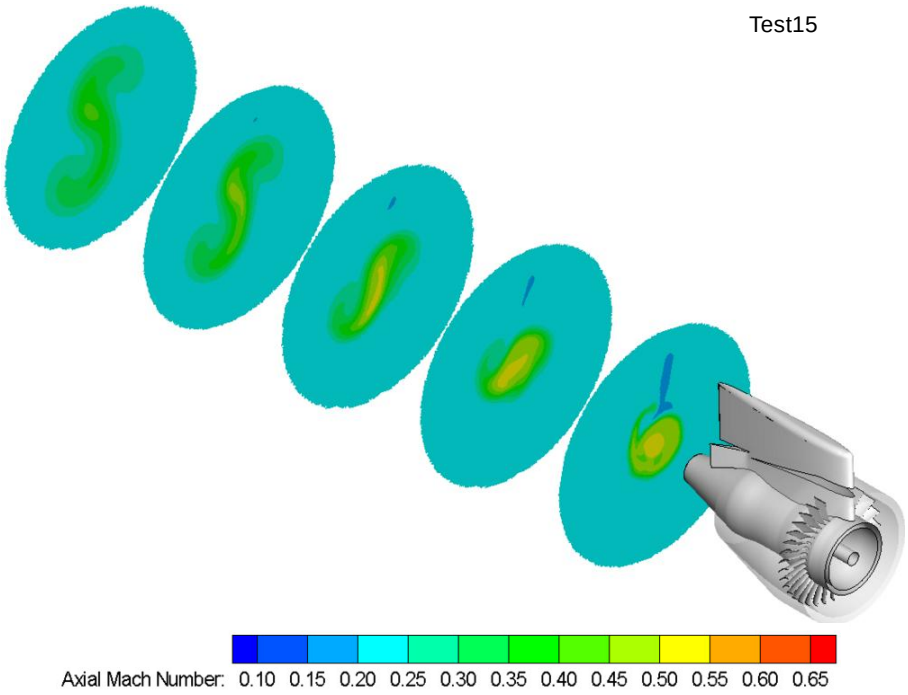

Figure 5–24: Axial Mach number contours in $r-\theta$ cross section planes for Test15 show the jet is unaffected without the fence installed.

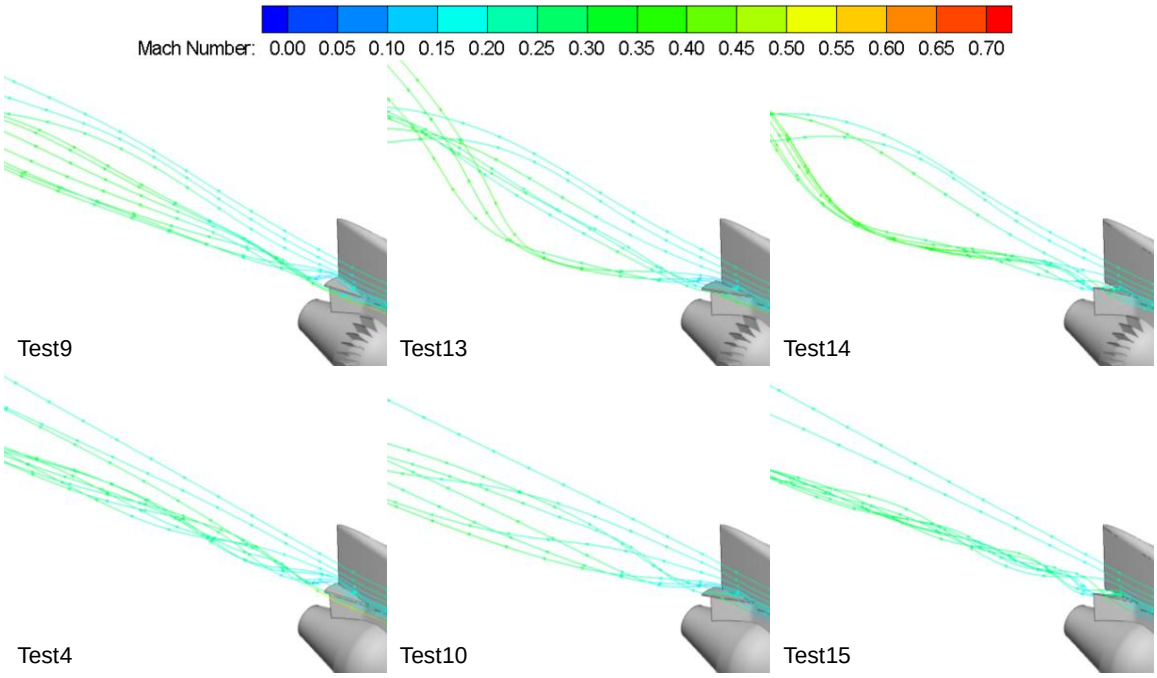

Figure 5–25: Streamlines near the fence show the effect of the side edge vortex on the flowfield in less pronounced when the fence is parallel to the fan nozzle.

5.4 Analysis of Side Loads

The horizontal force acting on each component of the EAB was calculated using Equation 4.7 to understand the effects of the swirling jet flow on the side loads. A breakdown of side loads for all test cases in shown in Table 5.3. A positive value indicates the force acts from the pressure side towards the suction side of the EAB.

Table 5.3: Summary of side loads acting on each component of the EAB for all 10 test cases.

Component	Test3	Test4	Test7	Test9	Test10	Test11	Test12	Test13	Test14	Test15
Pylon	-0.30	-0.34	-0.08	-0.05	-0.57	-0.50	-0.47	-0.03	-0.04	-0.48
Vanes	-0.26	-0.28	-0.25	-0.10	-0.12	-0.12	-0.13	-0.13	-0.13	-0.07
Core Nozzle	-0.99	-1.09	-0.18	-0.11	-1.27	-1.24	-1.15	-0.12	-0.13	-1.52
Fan Nozzle	1.69	1.78	0.32	0.17	2.06	2.05	1.82	0.20	0.20	2.14
Centerbody	0.00	0.00	0.00	0.00	0.00	0.00	0.00	0.00	0.00	0.00
Total	0.14	0.07	-0.19	-0.09	0.10	0.18	0.07	-0.07	-0.10	0.07

Four observations can be made from the results presented in Table 5.3. First, the forward vanes cases show a total positive side load whereas the aft vane cases show the resultant side load acts in the negative direction. For the forward vanes, this is due to an asymmetric pressure distribution on the fan nozzle inner diameter (ID) surface that causes a large positive side load on the fan nozzle which counteracts the negative loads on the core nozzle, pylon, and vane surfaces. From Figure 5–26 for Test4, the higher pressure on the suction side of the fan nozzle ID can be attributed to interaction of the surface with swirling flow from high exit angle, low solidity vanes placed upstream between the 4 o'clock and 9 o'clock positions (Figure 5–3). The swirling flow wraps around from the pressure side to the suction side within the length of the nozzle in the fan stream, pushing on the ID surface to generate the side loads. For the same reason, the core nozzle outer diameter (OD) surface inside the fan stream, shown in Figure 5–27 for Test4, experiences a large negative side force.

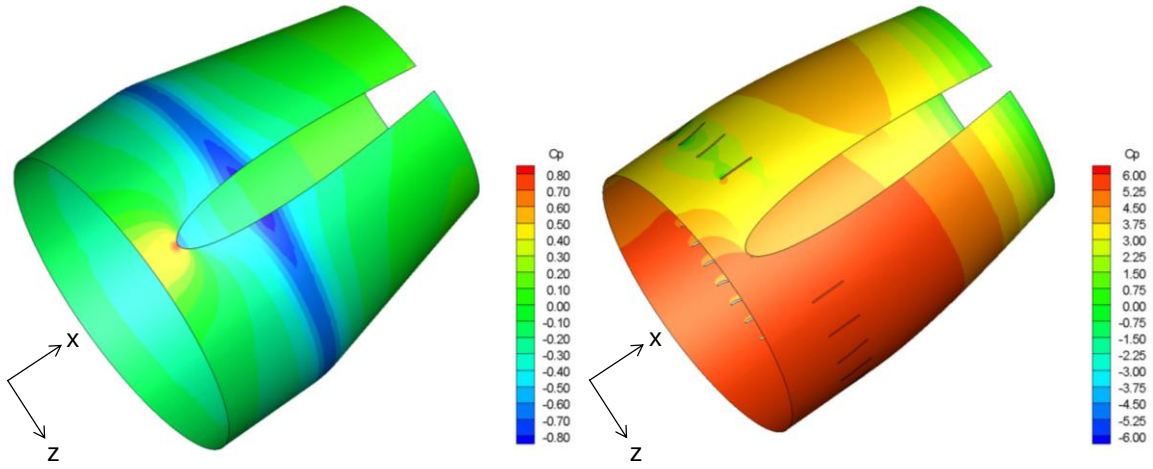

Figure 5–26: Cp contours on fan nozzle outer (left) and inner (right) diameter surfaces for Test4 show the asymmetric pressure distribution on the ID causes a large positive side load on the fan nozzle.

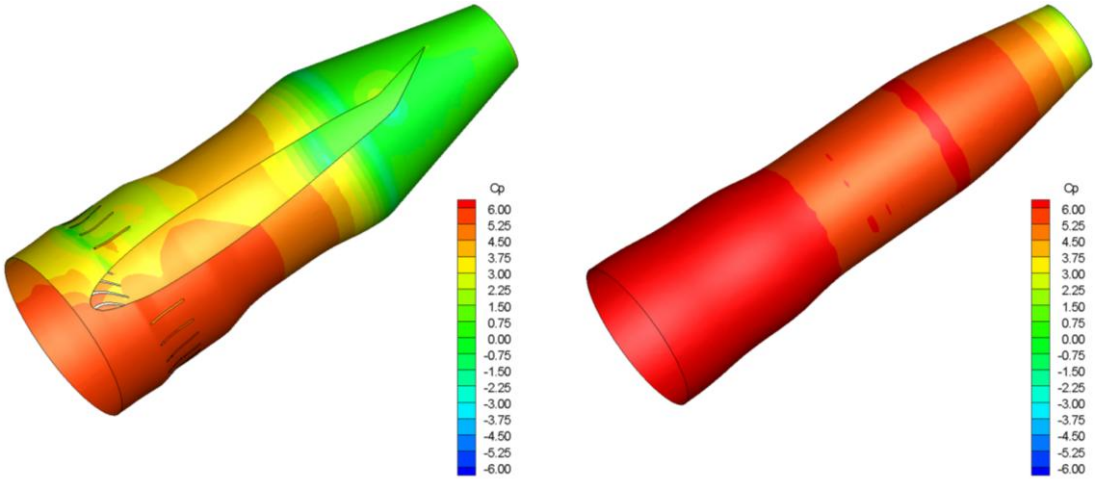

Figure 5–27: C_p contours on core nozzle outer (left) and inner (right) diameter surfaces for Test4 show the asymmetric pressure distribution on the OD causes a large negative side load on the core nozzle.

In contrast, the aft vanes cases show the loads on the fan and core nozzle surfaces are reduced considerably when flow is turned further downstream near the fan nozzle exit. This does not counteract the negative side loads on the other surfaces so the total side load on the EAB with aft vanes is negative. From Figure 5–28 for Test9, the asymmetric pressure distribution on the fan nozzle ID is a result of greater upstream influence on the pressure side. As the vane configuration

is symmetric about the vertical plane, (Figure 5–5), the upstream influence is from the pylon TE flap deflected towards the pressure direction.

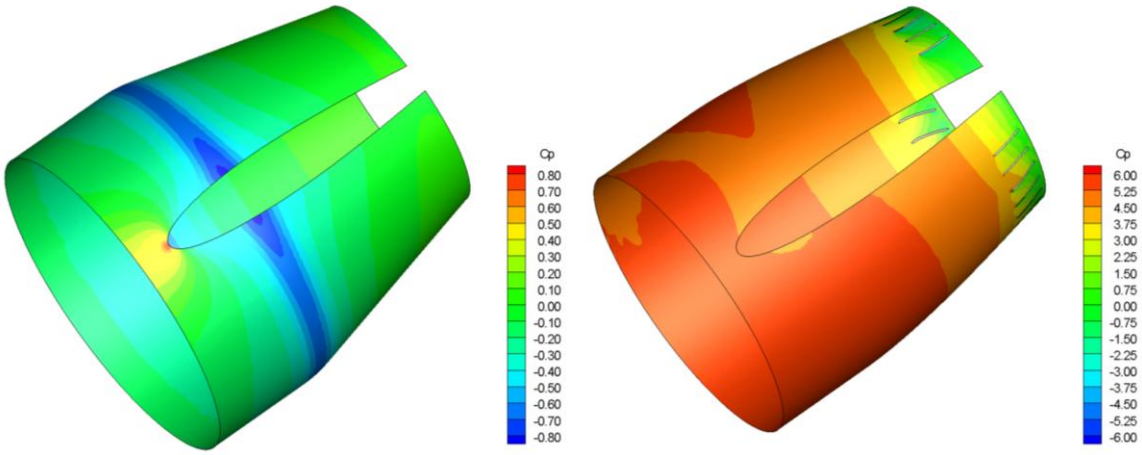

Figure 5–28: C_p contours on fan nozzle outer (left) and inner (right) diameter surfaces for Test9 show the asymmetric pressure distribution on the ID is due to greater upstream influence.

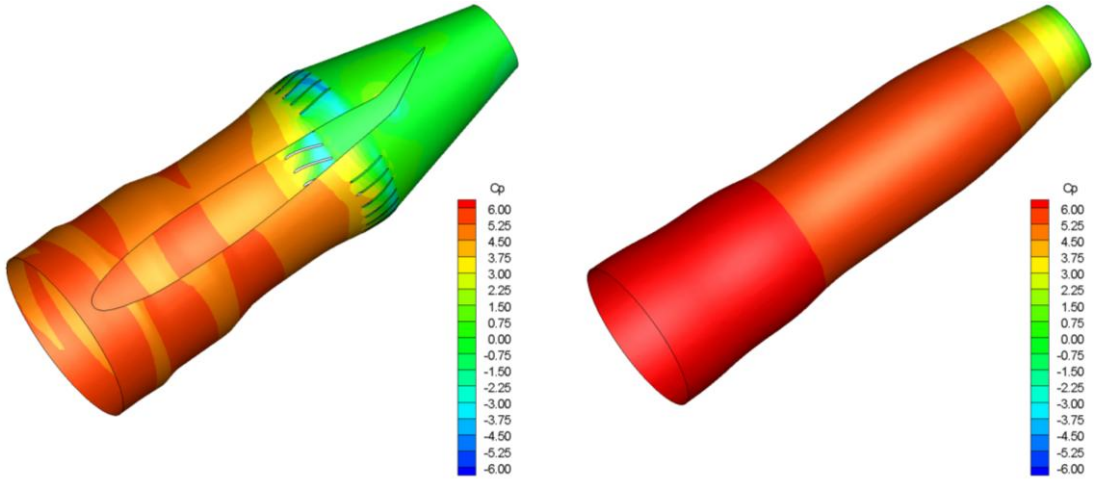

Figure 5–29: C_p contours on core nozzle outer (left) and inner (right) diameter surfaces for Test9 suggest flow is separating off the first few vanes on the pressure side of the OD surface.

On the core nozzle surfaces, Figure 5–29 shows flow is separating off the first three vanes on the pressure surface of the OD although results presented in Table 5.3 suggest this does not impact the loading of the vanes.

The second observation is the side loads on the pylon are reduced for the aft vanes cases, as expected, because the flow avoids the majority of the duct bifurcation. The negative side loads arise because flow is being turned away from the pressure side of the pylon towards the suction side. For the upstream vane concepts, the side loads on the pylon are between three to four times greater than the equivalent drag results. This is undesirable because it indicates the duct bifurcation obstructs the swirling flow that is generated upstream.

The third observation is the vanes all show a negative side load but in two distinct groups; the highly loaded cases (Test3, 4, 7) and the lightly loaded cases (Test9, 10, 11, 12, 13, 14, and 15). Both set of vane configurations are affected by vane exit angles, but the forward cases are also influenced by vane placement. The force on each vane in the horizontal direction is greater when vanes are placed in the region circumferentially opposite the pylon in the 6 o'clock position, as in Test4. For Test10, where vanes are packed between the 5 o'clock and 10 o'clock locations (Figure 5–6), the horizontal component of force acting on the vanes is reduced. By extension, since Test11, 12, and 15 have the same vane configuration as Test10, the side loads acting on the vanes for these cases are also smaller. Vanes in Test3 (Figure 5–1) experience larger side loads than in Test10 because of higher exit angles. For the aft vanes cases, the significant reduction in side loads of Test9 compared to Test7 is due to reduced vane exit angles and since Test13 and Test14 employ the same vane configuration as Test9, they are also lightly loaded.

The final observation is the centerbody does not experience a resultant side load because the pressure distribution on its surface is uniform.

Chapter 6

Conclusions

6.1 Summary and Conclusions

The feasibility of operating the EAB integrated with a pylon duct bifurcation in a realistic engine environment has been analyzed. A preliminary two-dimensional CFD investigation was first conducted on a pylon-cascade geometry to investigate the pylon's upstream influence, impact of the pylon on the downstream flow field, and to quantify the deterioration in flow turning angle. Analysis of the flowfield shows the separated flow region behind the pylon is due to the large flow incidence angle onto the pylon. Despite flow separation however, the average flow turning angle at the domain outlet, approximately 5*c* downstream of the pylon, is 26 degrees. This suggests it is possible to maintain swirling flow with guide vanes in the presence of a pylon.

To capture the effects of swirling flow, a detailed three-dimensional study was conducted on the 4-BB dual-stream HBPR nozzle with the pylon installed but without any turbomachinery. The baseline pylon is a prismatic NACA 0012 airfoil geometry with swept leading and trailing edges and an extended internal fairing to facilitate compatibility with the 4-BB and 5-BB nozzles in the NASA AAPL facility. Four pylon configurations were tested. Results demonstrate the baseline pylon configuration produces a thrust coefficient of 3.33 and blockage of 4.37% in the fan stream. The upward motion of the jet flow in the wake of the pylon is a result of entrainment of air from the freestream due to the pylon. The baseline pylon configuration with un-deflected swirl vanes at the fan nozzle exit produces a reduction in thrust of 2.42% and blockage of 5.46% due to the vanes. The AP1 configuration with an aggressive full-span pylon TE deflection of 35 degrees yields a large separation region on the suction side of the pylon near the core wall. In addition, flow is redirected off the pressure side without producing a coherent swirling outflow and flow interaction with the outer span forms a tip vortex that can adversely affect the noise signature of the EAB. Computational results suggest C_D is 0.25, C_S is 0.87, and blockage due to pylon is

5.50%. The AP2 configuration with the pylon TE flap deflected partial-span by 20 degrees and asymmetric swirl vanes at the upstream location generates swirling outflow from the fan nozzle exhaust, mitigating the side loads. Computational results suggest C_D is 0.11, C_S is 0.23, and blockage due to the pylon and vanes is 6.58%.

ATA's 10 additional alternative pylon/vane configurations were analyzed to understand the key differences between the different concepts. Investigation of the flowfield demonstrates the effect of the swirl vanes is to produce an asymmetric vortex sheet which rolls up and separates downstream of the EAB due to the induced velocity field from swirling outflow. This effect is more pronounced for the aft vane cases because the trailing vorticity is generated near the nozzle exhaust. Swirl parameter results at the location of vortex sheet separation for Test13, Test10, and an axisymmetric case with 60 degree swirl angle specified at the fan inlet are: 1.25, 0.62, and 1.22 respectively. For the two asymmetric concepts, the difference is because the aft set of vanes produces more positive circulation from stronger swirling motion compared to the upstream set of vanes. The circulation for the aft vane concepts is of similar strength to the axisymmetric case, suggesting the effect of the pylon duct bifurcation is less prominent when vanes are placed near the nozzle exhaust. Furthermore, the variation of swirl parameter with location suggests streamwise vorticity diffuses more rapidly in the axisymmetric case than the asymmetric cases. This is an indication that Test13 and other aft vane cases may not produce vortex breakdown.

The effect of a fence installed between the deflected TE flap and the un-deflected pylon was analyzed to determine its influence of the swirling jet deflection. From examining the jet evolution, there is no overall effect of the fence on the swirling flow deflection in the flowfield. However, locally the fence parallel to the fan nozzle prevents the formation of a side edge vortex seen without the fence installed and when the fence is parallel to the freestream. Thus from a noise perspective, a fence installed parallel to the fan nozzle is desirable for all alternative pylon/vane cases.

Finally, the component-wise analysis of side loads demonstrates pressure asymmetry creates resultant horizontal loads on the EAB. The upstream vane cases produce positive side loads because swirling flow in the fan duct wraps around from the pressure side to the suction side within the length of the nozzle, pushing on the ID surface to generate the side loads. This counteracts the negative side loads acting on the other components. The side loads on the pylon are between three to four times greater than the equivalent drag results, indicating the duct bifurcation obstructs the swirling motion that is generated upstream. The aft vane cases produce

negative side loads because the asymmetric pressure distribution on the fan nozzle ID is reduced as flow is turned further downstream, near the nozzle exhaust.

6.2 Implications of Present Work

The results of this study demonstrate coherent swirling outflow can be generated from an integrated EAB with asymmetric swirl vanes in the fan stream. The aft vane cases generate a stronger swirling outflow with C_D in the range of 0.35-0.61 compared to the upstream vanes cases which produce C_D between 0.09-0.18. The difference in drag is because the flow avoids the majority of the duct bifurcation in the aft vane cases to produce stronger swirling outflow. As a result, the flow blockage in the fan stream is between 11.3-15.1% for the aft vane cases compared to between 7.0-8.5% for the upstream vane cases. The drag results are below the target range of 0.7-1.0 required for a 3-4 degree glidescope change on several conventional tube-and-wing aircraft to achieve an overall noise benefit of 2.5 dB during approach. This suggests the current aft vane designs show potential in reaching the target C_D range of values while the upstream concepts require further investigation.

6.3 Recommendations for Future Work

The following list summarizes a few directions in which the present study could be extended:

- Investigation of the flowfield, equivalent drag, side load, and mass flow results for all EAB designs at a higher set of approach CNPRs and FNPRs to establish the swirl-drag-mass flow relationship for a wide range of operating conditions. This analysis can help answer the question: are current EAB designs better suited to engines with higher approach FNPRs?
- Quantification of the swirl-drag-mass flow relationship for Test13 and Test10 at the fan nozzle exhaust and comparison with experimental results obtained from model-scale tests at the NASA AAPL facility.
- Examination of the far-field noise signature for the aft vane case Test13 to determine if it produces vortex breakdown. Based on these findings, similar conclusions may be reached for the other aft vane cases, Test7, Test9, and Test14.
- Exploration of alternate means to maintain coherent swirling outflow in the presence of a pylon for the upstream vane concepts. One possible idea is to impart swirling motion onto the high velocity core flow.

Bibliography

[1] Cumpsty, N. A., 2003, *A Simple Guide to the Aerodynamic and Thermodynamic Design and Performance of Jet Engines* , Cambridge University Press, Cambridge, United Kingdom.

[2] Shah, P. N., 2006, Novel Turbomachinery Concepts for Highly Integrated Airframe/Propulsion Systems, Ph.D. Thesis, Massachusetts Institute of Technology, Cambridge, MA.

[3] Shah, P. N., Mobed, D. D., and Spakovszky, Z. S., 2007, Engine Air-Brakes for Quiet Air Transport, *45th AIAA Aerospace Sciences Meeting and Exhibit*, American Institute of Aeronautics and Astronautics, AIAA 2007-1033, Reno, NV.

[4] Hileman, J. I., Spakovszky, Z. S., and Drela, M., 2006, Aerodynamic and Aeroacoustic Three-Dimensional Design for a "Silent" Aircraft, *44th AIAA Aerospace Sciences Meeting and Exhibit*, American Institute of Aeronautics and Astronautics, AIAA 2006-241, Reno, NV.

[5] Mody, P. C., Sato, S., Hall, D. K. et al., 2010, Conceptual Design of an N+3 Hybrid Wing Body Subsonic Transport, *28th AIAA Applied Aerodynamics Conference*, American Institute of Aeronautics and Astronautics, AIAA 2010-4812, Chicago, IL.

[6] Collier, F., 2010, Overview of NASA's Environmentally Responsible Aviation (ERA) Project (PowerPoint Presentation), *48th AIAA Aerospace Sciences Meeting*, American Institute of Aeronautics and Astronautics, Orlando, FL.

[7] Shah, P. N., Mobed, D. D., and Spakovszky, Z. S., 2007, A Novel Turbomachinery Air-Brake Concept for Quiet Aircraft, *2007 ASME Turbo Expo: Gas Turbine Technical Conference* , American Society of Mechanical Engineers, GT2007-27635, Montreal, Canada.

[8] General Electric Aviation, 1995, "The GE90 Engine," Retrieved online on August 1, 2010 from http://www.geae.com/aboutgeae/presscenter/ge90/ge90_19951109a.html/.

[9] Thomas, R. H., Burley, C. L., and Olson, E. D., 2010, Hybrid Wing Body Aircraft System Noise Assessment With Propulsion Airframe Aeroacoustic Experiments, *16th AIAA/CEAS Aeroacoustics Conference*, American Institute of Aeronautics and Astronautics, AIAA 2010-3913, Stockholm, Sweden.

[10] Dunbar, D. K., 1993, Method of Operating an Aircraft Bypass Turbofan Engine having Variable Fan Outlet Guide Vanes, US Patent No. 5,259,197.

[11] DeBonis, J. R., 2009, RANS Analyses of Turbofan Nozzles with Internal Wedge Deflectors for Noise Reduction, *Journal of Fluids Engineering*, **131**.

[12] National Aeronautics and Space Administration, 2008, "Facilities: Aero-Acoustic Propulsion Laboratory," Retrieved online on September 12, 2010 from http://facilities.grc.nasa.gov/aapl/.

[13] Smith, M. J. T., 1989, *Aircraft Noise*, Cambridge University Press, Cambridge, United Kingdom.

[14] Shah, P. N., Mobed, D. D., and Spakovszky, Z. S., 2007, Aero-Acoustics of Drag Generating Swirling Exhaust Flows, *13th AIAA/CEAS Aeroacoustics Conference (28th AIAA Aeroacoustics Conference)*, American Institute of Aeronautics and Astronautics, AIAA 2007-3714, Rome, Italy.

[15] Linke-Diesinger, A., 2008, *Systems of Commercial Turbofan Engines: An Introduction to Systems Functions*, Springer-Verlag, Leipzig, Germany.

[16] Wanhill, R. J. H., and Oldersma, A., 1996, Fatigue and Fracture in an Aircraft Engine Pylon, National Aerospace Laboratory NLR, Report # 96719, Amsterdam, the Netherlands.

[17] Goodrich Aerostructures, 2004, "Aerostructures Suppliers," Retrieved online on June 4, 2009 from http://www.goodrich.com/.

[18] Hughes, C. E., Jeracki, R. J., and Woodward, R. P., 2005, Fan Noise Source Diagnostic Test - Rotor Alone Aerodynamic Performance Results, National Aeronautics and Space Administration, NASA/TM-2005-211681, Cleveland, OH.

[19] Woodward, R. P., and Hughes, C. E., 2004, Noise Benefits of Increased Fan Bypass Nozzle Area, National Aeronautics and Space Administration, NASA/TM-2004-213396, Cleveland, OH.

[20] Hughes, C. E., 2001, Aerodynamic Performance of Scale-Model Turbofan Outlet Guide Vanes Designed for Low Noise, National Aeronautics and Space Administration, NASA/TM-2001-211352, Cleveland, OH.

[21] Fluent User Services Center, 2005, "Modeling Turbulent Flows," Retrieved online on July 14, 2009 from http://www.fluentusers.com/.

[22] Lowey, H., 1990, GE's CF34 Engine for Business and Regional Jets, *AIAA/SAE/ASME/ASEE 26th Joint Propulsion Conference*, American Institute of Aeronautics and Astronautics, AIAA 90-2041, Orlando, FL.

[23] Naik, D. A., Ingraldi, A. M., and Pendergraft Jr., O. C., 1993, Experimental Study of Pylon Cross Sections for a Subsonic Transport Airplane, *Journal of Aircraft*, **30**(5).

[24] General Electric Aviation, 2008, "The CF34 Family," Retrieved online on August 12, 2009 from http://www.geae.com/engines/commercial/cf34/index.html/.

[25] Airliners.net, 2007, "The Wings of the Web," Retrieved online on June 3, 2009 from http://www.airliners.net/.

[26] Borg, D., 2001, Flight Testing of the CF34-8C Engine on the GE B747 Flying Test Bed, *1st Aircraft, Technology Integration, and Operations Forum*, American Institute of Aeronautics and Astronautics, AIAA 2001-5271, Los Angeles, CA.

[27] Delery, J. M., 1994, Aspects of Vortex Breakdown, *Progress in Aerospace Sciences*, **30,** pp. 1-59.

[28] Greitzer, E. M., Tan, C. S., and Graf, M. B., 2004, *Internal Flow: Concepts and Applications*, Cambridge University Press, Cambridge, United Kingdom.

[29] CD-adapco, 2008, "Modeling Turbulence and Transition in Star-CCM+," Retrieved online on September 16, 2010 from http://www.cd-adapco.com/.

[30] Boeing Commercial Airplanes, 2007, "Airport Reference Code and Approach Speeds for Boeing Airplanes," Retrieved online on September 18, 2010 from http://www.boeing.com/.